

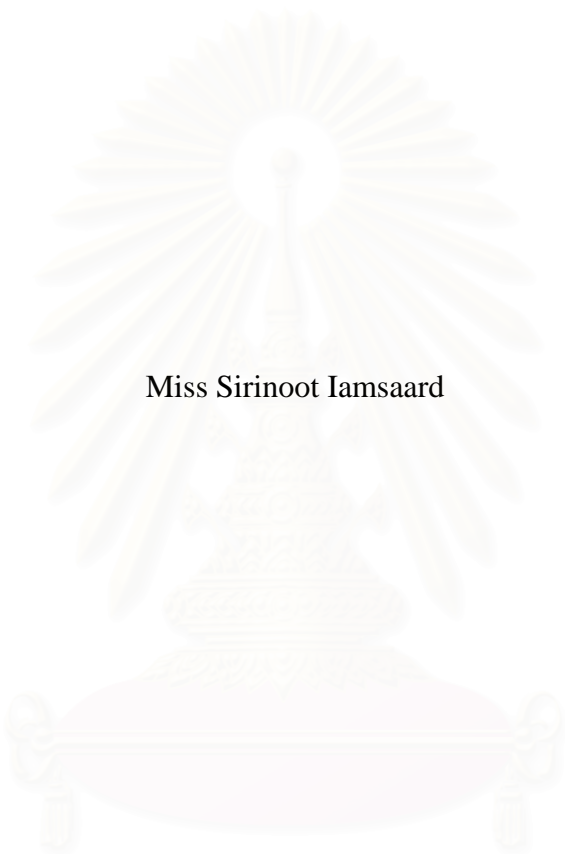
การเข้ากันได้เชิงเคมีและกายภาพของเลนทามันนิกิลเหล็กออกไซด์
และอิตเทรียสเทปิลไซด์เซอร์โคเนีย

นางสาวศิรินุช เอี่ยมสอาด

สถาบันวิทยบริการ
จุฬาลงกรณ์มหาวิทยาลัย

วิทยานิพนธ์นี้เป็นส่วนหนึ่งของการศึกษาตามหลักสูตรปริญญาวิทยาศาสตรมหาบัณฑิต
สาขาวิชาปิโตรเคมี และวิทยาศาสตร์พอลิเมอร์
คณะวิทยาศาสตร์ จุฬาลงกรณ์มหาวิทยาลัย
ปีการศึกษา 2550
ลิขสิทธิ์ของจุฬาลงกรณ์มหาวิทยาลัย

CHEMICAL AND PHYSICAL COMPATIBILITY OF LANTHANUM NICKEL
IRON OXIDES AND YTTRIA STABILIZED ZIRCONIA



Miss Sirinoot Iamsaard

สถาบันวิทยบริการ
จุฬาลงกรณ์มหาวิทยาลัย

A Thesis Submitted in Partial Fulfillment of the Requirements

for the Degree of Master of Science Program in Petrochemistry and Polymer Science

Faculty of Science

Chulalongkorn University

Academic Year 2007

Copyright of Chulalongkorn University

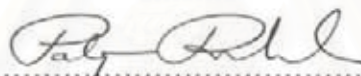
Thesis Title CHEMICAL AND PHYSICAL COMPATIBILITY OF
LANTHANUM NICKEL IRON OXIDES AND YTTRIA
STABILIZED ZIRCONIA
By Miss Sirinoot Iamsaard
Field of Study Petrochemistry and Polymer Science
Thesis Advisor Nipaka sukpirom, Ph.D.

Accepted by the Faculty of Science, Chulalongkorn University in Partial
Fulfillment of the Requirements for the Master's Degree



.....Dean of the Faculty of Science
(Professor Supot Hannongbua, Ph.D.)

THESIS COMMITTEE



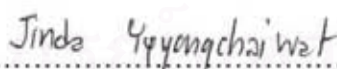
.....Chairman
(Professor Pattarapan Prasassarakich, Ph.D.)



.....Thesis Advisor
(Nipaka Sukpirom, Ph.D.)



.....Member
(Associate Professor Wimonrat Trakarnpruk, Ph.D.)



.....Member
(Assistant Professor Jinda Yeyongchaiwat, Ph.D.)

ศรินุช เอี่ยมสอาด : การเข้ากันได้เชิงเคมีและกายภาพของแลนทานัม นิกเกิล เหล็ก ออกไซด์ และอิตเทรียสเทบิลไลซ์เซอร์โคเนีย (CHEMICAL AND PHYSICAL COMPATIBILITY OF LANTHANUM NICKEL IRON OXIDES AND YTTRIA STABILIZED ZIRCONIA) อ. ที่ปรึกษา: ดร. นิปกา สุขภิรมย์, 128 หน้า.

ศึกษาการเข้ากันได้เชิงเคมีและกายภาพของวัสดุสำหรับใช้เป็นขั้วแคโทดในเซลล์เชื้อเพลิงชนิดออกไซด์ของแข็ง คือ $\text{La}(\text{Ni}_{1-x}\text{Fe}_x)_2\text{O}_3$ (LNF) ซึ่งมีโครงสร้างแบบเพอโรฟสไกต์ และ $\text{La}_2(\text{Ni}_{1-x}\text{Fe}_x)_4\text{O}_4$ (L_2NF) ซึ่งมีโครงสร้างแบบ K_2NiF_4 กับของแข็งอิเล็กโทรไลต์ที่ใช้ในทางการค้า คือ 8 โมลเปอร์เซ็นต์ของอิตเทรียสเทบิลไลซ์เซอร์โคเนีย (8-YSZ) ในชั้นแรก LNF และ L_2NF โดยที่ x เท่ากับ 0.0-1.0 ถูกเตรียมด้วยวิธีซิเตรทและวิธีซิเตรทประยุกต์ จากการตรวจสอบลักษณะเฉพาะด้วยเทคนิค XRD พบว่า LNF ที่สังเคราะห์ด้วยสองวิธีนั้นและเผาที่อุณหภูมิ 700-900 °ซ เป็นเวลา 5 ชั่วโมงจะได้เป็นเฟสเดี่ยวทั้งสิ้น โดยเมื่อ x เท่ากับ 0.0-0.5 โครงสร้างผลึกเป็นแบบคิวบิกและรวมโบฮีรอลที่ 700 และ 900 °ซ ตามลำดับ การศึกษาเพิ่มเติมพบว่า LNF ที่มีโครงสร้างผลึกเป็นแบบคิวบิกจะเปลี่ยนเป็นโครงสร้างผลึกแบบรวมโบฮีรอลที่อุณหภูมิ 900 °ซ และมีความเสถียรจนถึงอุณหภูมิ 1200 °ซ เมื่อ x เท่ากับ 0.6-1.0 โครงสร้างผลึกเป็นแบบออร์โธโรมบิกทั้งสองอุณหภูมิ โครงสร้างผลึกแบบออร์โธโรมบิกชนิดนี้สลายตัวที่ 1200 °ซ ส่วนในกรณีของ L_2NF พบว่าเฉพาะ L_2NF ที่ x เท่ากับ 0.0 และ 0.1 และเผาที่อุณหภูมิ 900 °ซ เท่านั้น ที่ได้เป็นเฟสเดี่ยว โดยมีโครงสร้างผลึกเป็นแบบเททราโกนอล นอกจากนี้ค่าแลตทิซและปริมาตรต่อหน่วยยูนิตโดยทั่วไปมีแนวโน้มเพิ่มขึ้นเมื่อปริมาณของเหล็กมีมากขึ้น จากนั้นศึกษาติดตามความเข้ากันได้ของ LNF และ L_2NF กับ 8-YSZ ด้วยเทคนิค XRD และ SEM-EDX พบว่าสารที่ได้สกัดส่วนตามสูตรเคมี $\text{La}(\text{Ni}_{0.6}\text{Fe}_{0.4})_2\text{O}_3$ และ $\text{La}_2(\text{Ni}_{0.9}\text{Fe}_{0.1})_4\text{O}_4$ กับ 8-YSZ เข้ากันได้เชิงเคมีจนถึงอุณหภูมิ 900 °ซ ในกรณีของสารที่ไม่ได้สกัดส่วนตามสูตรเคมี $\text{La}(\text{Ni}_{0.6}\text{Fe}_{0.4})_2\text{O}_3$ และ $\text{La}_2(\text{Ni}_{0.9}\text{Fe}_{0.1})_4\text{O}_4$ โดย y มีค่าเท่ากับ 0.95 และ 1.05 พบว่าสามารถมีการเข้ากันได้เชิงเคมีกับ 8-YSZ จนถึงอุณหภูมิ 800 °ซ นอกจากนี้พบว่าค่าสัมประสิทธิ์การขยายตัวเนื่องจากความร้อนที่อุณหภูมิ 800 °ซ ของ $\text{La}(\text{Ni}_{0.6}\text{Fe}_{0.4})_2\text{O}_3$ และ $\text{La}_2(\text{Ni}_{0.9}\text{Fe}_{0.1})_4\text{O}_4$ มีค่าเท่ากับ $13.2 \times 10^{-6} \text{ K}^{-1}$ และ $12.7 \times 10^{-6} \text{ K}^{-1}$ ตามลำดับ ซึ่งเป็นค่าที่ใกล้เคียงกับค่าสัมประสิทธิ์การขยายตัวของ 8-YSZ จึงแสดงว่าแลนทานัม นิกเกิล เหล็ก ออกไซด์ที่สังเคราะห์ได้มีความเข้ากันได้ทางกายภาพกับ 8-YSZ

สาขาวิชา วัสดุเคมีและวิทยาศาสตร์พอลิเมอร์ ลายมือชื่อนิสิต ศรินุช เอี่ยมสอาด
ปีการศึกษา 2550 ลายมือชื่ออาจารย์ที่ปรึกษา นิปกา สุขภิรมย์

4872484823 : MAJOR PETROCHEMISTRY AND POLYMER SCIENCE
 KEY WORD: PEROVSKITE / K_2NiF_4 -TYPED / LANTANUM NICKEL IRON
 OXIDES / YTTRIA STABILIZED ZIRCONIA / SOLID OXIDE FUEL CELLS

SIRINOOT IAMSAARD: CHEMICAL AND PHYSICAL
 COMPATIBILITY OF LANTHANUM NICKEL IRON OXIDES AND
 YTTRIA STABILIZED ZIRCONIA. THESIS ADVISOR: NIPAKA
 SUKPIROM, Ph.D., 128 pp.

The chemical and physical compatibilities of the candidates, $LaNi_{1-x}Fe_xO_3$ (LNF) perovskites and K_2NiF_4 -typed $La_2Ni_{1-x}F_xO_4$ (L_2NF), of a cathode material for solid oxide fuel cell with the commercial solid electrolyte, 8 mol % Ytria Stabilized Zirconia (8-YSZ), were studied. Firstly, LNF and L_2NF with $x = 0-1.0$ were prepared by Water Citrate (WC) and Modified Water Citrate (MWC) methods, and characterized by XRD. It was found that the single phased LNF perovskites were synthesized successfully by both methods at 700-900 °C for 5h. As x is 0-0.5, the crystal structure is cubic and rhombohedral at the calcination temperature of 700 °C and 900 °C, respectively. The further investigation indicated that the cubic structure changed to the rhombohedral structure at 900 °C, and was stable up to 1200 °C. As x is 0.6-1.0, the crystal structure is in the orthorhombic phase at both calcination temperatures. This orthorhombic phase decomposed at 1200 °C. The single-phased L_2NF systems were achieved only that of $x = 0$ and 0.1 after calcination at 900 °C. The crystal structure of L_2NF is tetragonal. In all cases, the lattice constants and the volume per formula unit in all series generally increased as the Fe content increased. Following the reaction by XRD and SEM-EDX, the stoichiometric $La(Ni_{0.6}Fe_{0.4})O_3$ and $La_2(Ni_{0.9}Fe_{0.1})O_4$ have a good chemical compatibility with 8-YSZ from room temperature up to 900 °C. In the case of the non-stoichiometric $La(Ni_{0.6}Fe_{0.4})_yO_3$ and $La_2(Ni_{0.9}Fe_{0.1})_yO_4$ ($y = 0.95$ and 1.05), the chemical compatibility with 8-YSZ is good up to 800 °C. In addition the thermal expansion coefficients of $La(Ni_{0.6}Fe_{0.4})O_3$ and $La_2(Ni_{0.9}Fe_{0.1})O_4$ are $13.2 \times 10^{-6} K^{-1}$ and $12.7 \times 10^{-6} K^{-1}$, respectively. These values are close to that of 8-YSZ; therefore, lanthanum nickel iron oxide of both structures have a good physical compatibility with 8-YSZ.

Field of Study Petrochemistry and Polymer Science Student's Signature Sirinoot Iamsaard
 Academic year2007..... Advisor's Signature Nipaka Sukpirom

ACKNOWLEDGEMENTS

The author is deeply appreciated to her family for their love, support and encouragement during her the period of her study.

The author wishes to express greatest gratitude to her advisor, Dr. Nipaka Sukpirom, for her valuable advice, kind assistance, and encouragement throughout the course of this research. Gratefully thanks to Dr. Sumittra Charojrochkul from National Metal and Materials Technology Center, and Assistant Professor Dr. Jinda Yeyongchaiwat, hers for good advice, kind assistance and equipment. In addition, the author would like to special thank to Associate professor Dr. Phattarapan Prasassarakich, Associate Professor Dr. Wimonrat Trakarnpruk, and Assistant Professor Dr. Jinda Yeyongchaiwat for serving as the chairman and members of her thesis committee, respectively, for their valuable suggestions and comments.

Appreciation is extended to Materials Chemistry and Catalysis Research Unit (MATCAT) for financial support during study and provision of experimental facilities. Acknowledgement is also extended to Program of Petrochemistry and Polymer Science, Department of Chemistry, faculty of Science and Graduate School, Chulalongkorn University for granting financial support to fulfill this study.

This thesis can not complete without generous help of the staff members of the Materials Chemistry and Catalysis Research Unit (MATCAT). Special thank is forwarded to my best friends for their love, assistance and encouragement. Without them, the author would have never been able to achieve this goal.

CONTENTS

	Page
ABSTRACT IN THAI	iv
ABSTRACT IN ENGLISH	v
ACKNOWLEDGEMENTS	vi
CONTENTS	vii
LIST OF FIGURES	xi
LIST OF SCHEMES	xvi
LIST OF TABLES	xvii
LIST OF ABBREVIATIONS	xx
CHAPTER I INTRODUCTION	1
1.1 Background	1
1.2 Literature reviews of cathode materials selection	2
1.2.1 Literature reviews of perovskite type structure	2
1.2.2 Literature reviews of K_2NiF_4 -typed structure	6
1.2.3 Literature reviews of chemical and physical compatibility of cathode with the 8-YSZ electrolyte.....	10
1.3 The objectives of this study.....	13
CHAPTER II THEORY	15
2.1 Materials Issues (SOFC)	17
2.1.1 Cathode (Air Electrode) and Anode (H_2/CO Electrode).....	17
2.1.2 Electrolyte (Air Electrode).....	17
2.1.3 Interconnect (between Cathode and Anode).....	17
2.2 Physical and physicochemical properties of cathode materials.....	18
2.2.1 Perovskite-type structure	18
2.2.2 K_2NiF_4 -typed structure	20
2.2.3 Fundamental	22
2.2.4 Thermal expansion	22
2.3 Reactivity of perovskite cathode with YSZ	23
2.3.1 Thermodynamic considerations	23

	Page
2.3.2 Reaction of perovskite with the zirconia component in YSZ	24
2.4 The synthesis of perovskite and K_2NiF_4 -typed structure synthesis	24
2.4.1 Solid-state reaction	24
2.4.2 Solution reaction	24
2.5 Powder sizing	25
2.5.1 Powder compacting by uniaxial pressing	25
2.5.2 Sintering	26
2.6 Screen-printing	27
2.7 Crystal structure	27
2.7.1 Lattice and Unit cell	27
2.7.2 Crystal systems and Bravais Lattices	28
2.7.3 Miller Indices	29
2.8 Characterization of materials	30
2.8.1 X-ray Diffraction (XRD)	30
CHAPTER III EXPERIMENTAL	33
3.1 Chemicals	33
3.2 Synthesis of perovskite and K_2NiF_4 -typed powders	33
3.2.1 Synthesis of perovskite and K_2NiF_4 powders by water citrate method (WC)	33
3.2.2 Synthesis of perovskite and K_2NiF_4 powders by modified water citrate (MWC).....	34
3.2.3 Synthesis of perovskite and K_2NiF_4 powders by nitric citrate (NC)	34
3.2.4 Synthesis of perovskite and K_2NiF_4 powders by modified nitric citrate (MNC).....	35
3.3 Chemical compatibility	40
3.3.1 The mixtures of LNF and L_2NF powders with 8-YSZ	40
3.3.2 The membrane of LNF and L_2NF powders with 8-YSZ by screen-printing technique	40
3.4 Physical compatibility	40

3.5 Characterization of materials	40
3.5.1 Powder X-ray diffraction (XRD)	40
3.5.2 Scanning electron microscopy (SEM)	41
3.5.3 Particle size analysis	41
CHAPTER IV RESULTS AND DISCUSSION.....	42
4.1 Perovskite powders	42
4.1.1 Crystal structure	42
A. Crystal structure of $\text{LaNi}_{1-x}\text{Fe}_x\text{O}_3$ by the WC method at 700 °C	42
B. Crystal structure of $\text{LaNi}_{1-x}\text{Fe}_x\text{O}_3$ by the MWC method at 700 °C	45
C. Crystal structure of $\text{LaNi}_{1-x}\text{Fe}_x\text{O}_3$ by the WC method at 900 °C	47
D. Crystal structure of $\text{LaNi}_{1-x}\text{Fe}_x\text{O}_3$ by the MWC method at 900 °C	49
E. The volume per formula unit of $\text{LaNi}_{1-x}\text{Fe}_x\text{O}_3$ perovskites.....	50
F. The phase diagram of LNF perovskite powders	54
4.1.2 The comparison of four combustion methods in the synthesis of LNF-64.....	56
4.1.3 Chemical compatibility with 8-YSZ electrolyte.....	59
4.1.3.1 The mixtures of LNF-64 perovskite powders with 8-YSZ	59
A. Stoichiometric perovskite of $\text{La}(\text{Ni}_{0.6}\text{Fe}_{0.4})_y\text{O}_3$ ($y = 1.00$) with 8-YSZ mixtures.....	59
B. Non-Stoichiometric perovskite of $\text{La}(\text{Ni}_{0.6}\text{Fe}_{0.4})_y\text{O}_3$ ($y = 0.95$) with 8-YSZ mixtures	62
C. Non-Stoichiometric perovskite of $\text{La}(\text{Ni}_{0.6}\text{Fe}_{0.4})_y\text{O}_3$ ($y = 1.05$) with 8-YSZ mixtures	65
4.1.3.2 The membrane of LNF-64 perovskite powder with 8-YSZ	68
4.1.4 Physical compatibility of LNF-64 with 8-YSZ electrolyte	72

	Page
4.2 K ₂ NiF ₄ powders	74
4.2.1 Crystal structure	74
A. Crystal structure of La ₂ Ni _{1-x} Fe _x O ₄ by the WC method at 700 °C	74
B. Crystal structure of La ₂ Ni _{1-x} Fe _x O ₄ by the MWC method at 700 °C	75
C. Crystal structure of La ₂ Ni _{1-x} Fe _x O ₄ by the WC method at 900 °C	76
D. Crystal structure of La ₂ Ni _{1-x} Fe _x O ₄ by the MWC method at 900 °C	77
E. The volume per formula unit of La ₂ Ni _{1-x} Fe _x O ₄	79
4.2.2 The comparison of four combustion methods on the synthesis of L ₂ NF-91.....	80
4.2.3 Chemical compatibility with 8-YSZ electrolyte.....	83
4.2.3.1 The mixtures of L ₂ NF-91 K ₂ NiF ₄ powders with 8-YSZ.....	83
A. Stoichiometric K ₂ NiF ₄ -typed of La ₂ (Ni _{0.9} Fe _{0.1}) _y O ₄ (y = 1.00) with 8-YSZ mixtures	83
B. Non-Stoichiometric K ₂ NiF ₄ -typed of La ₂ (Ni _{0.9} Fe _{0.1}) _y O ₄ (y = 0.95) with 8-YSZ mixtures	86
C. Non-Stoichiometric K ₂ NiF ₄ -typed of La ₂ (Ni _{0.9} Fe _{0.1}) _y O ₄ (y = 1.05) with 8-YSZ mixtures	89
4.2.3.2 The membrane of L ₂ NF-91 powder with 8-YSZ	92
4.2.4 Physical compatibility of L ₂ NF-91 structure with 8-YSZ electrolyte.	94
 CHAPTER V CONCLUSION AND SUGGESTION	95
5.1 Conclusion	95
A. Perovskite structure	95
B. K ₂ NiF ₄ -typed structure	95
C. Chemical compatibility of both structures with 8-YSZ.....	96
D. Physical compatibility between both structures with 8-YSZ.....	96
5.2 Suggestion.....	97
REFERENCES	98
APPENDICES	106
VITAE	128

LIST OF FIGURES

Figure	Page
2.1 Solid oxide fuel cells two configurations (a) Flat panel (b) Tubular.....	15
2.3 Ideal perovskite structure illustrated for ABO_3 . Note the corner shared octahedra, extending in three dimensions.....	19
2.4 Ideal K_2NiF_4 -typed structure illustrated for A_2BO_4 showing the NiF_6 octahedra and potassium ions (black spheres).....	21
2.5 The relationships for length in terms of the linear expansion.....	22
2.6 Mechanism of sintering.....	26
2.7 Unit cell and lattice.....	27
2.8 A unit cell with x, y and z coordinate axes, showing the lattice parameters: axial lengths (a, b and c) and interaxial angles (α , β and γ).....	28
2.9 An example of miller indices: (111).....	30
2.10 Diffraction of X-rays by a crystal	31
2.11 XRD pattern of $LaNi_{0.6}Fe_{0.4}O_3$ (perovskite structure).....	32
4.1 XRD patterns of $LaNi_{1-x}Fe_xO_3$ ($x = 0.0-1.0$) perovskites, synthesized by WC method and calcined at $700\text{ }^\circ\text{C}$ for 5h.....	43
4.2 Simulated XRD patterns of (a) $LaNiO_3$ from JCPDS: 33-0710 (b) $LaFeO_3$ from JCPDS: 37-1493.....	43
4.3 XRD patterns of $LaNi_{1-x}Fe_xO_3$ ($x = 0.0-1.0$) perovskites, synthesized by MWC method and calcined at $700\text{ }^\circ\text{C}$ for 5h	45
4.4 XRD patterns of $LaNi_{1-x}Fe_xO_3$ ($x = 0.0-1.0$) perovskites, synthesized by WC method after calcined at $900\text{ }^\circ\text{C}$ for 5h.....	47
4.5 Simulated XRD patterns of (a) $LaNiO_3$ from JCPDS: 33-0711 (b) $LaFeO_3$ from JCPDS: 37-1493.....	48
4.6 XRD patterns of $LaNi_{1-x}Fe_xO_3$ ($x = 0.0-1.0$) perovskites, synthesized by WC method after calcined at $900\text{ }^\circ\text{C}$ for 5h.....	49
4.7 The volume of formula unit of $LaNi_{1-x}Fe_xO_3$ ($x = 0.0-1.0$) perovskite, synthesized by (a) WC (b) MWC, and calcined at $700\text{ }^\circ\text{C}$ for 5h.....	52
4.8 The volume of formula unit of $LaNi_{1-x}Fe_xO_3$ ($x = 0.0-1.0$) perovskite, synthesized by (a) WC (b) MWC, and calcined at $900\text{ }^\circ\text{C}$ for 5h.....	52

Figure	page
4.9 XRD patterns of LNF-37 perovskite powder after being calcined at (a) 700 °C 5h (b) 800 °C 5h (c) 900 °C 5h (d) 1000 °C 5h and (e) 1200 °C for 5h.....	54
4.10 XRD patterns of LNF-64 perovskite powder after being calcined at (a) 700 °C 5h (b) 800 °C 5h (c) 900 °C 5h (d) 1000 °C 5h and (e) 1200 °C for 5h.....	55
4.11 The structural phase diagrams of LNF-37 and LNF-64.....	56
4.12 XRD patterns of LNF-64, synthesized by four methods (a) WC, (b) MWC, (c) NC, and (d) MNC with the calcination temperature of 1000 °C for 5 h.....	57
4.13 SEM pictures of LNF-64 with the calcination temperature of 1000 °C for 5 h (a) WC (b) MWC (c) NC (d) MNC	58
4.14 XRD patterns of (a) LNF-64 ($y = 1.00$), (b) 8-YSZ, and the powder Mixtures between LNF-64 ($y = 1.00$) and 8-YSZ: (c) the mixtures at room temperature, (d) after calcination at 800°C for 5h, (e) after calcination at 900°C for 5h, (f) after calcination at 1000 °C for 5h, (g) after calcination at 1100 °C for 5h, and (h) after calcination 1200 °C for 5h.....	59
4.15 XRD patterns between a 2θ range of $25-36^\circ$ of (a) LNF-64 ($y = 1.00$), (b) 8-YSZ, and the powder mixtures between LNF-64 ($y = 1.00$) and 8-YSZ: (c) the mixtures at room temperature, (d) after calcination at 800°C for 5h, (e) after calcination at 900°C for 5h, (f) after calcination at 1000 °C for 5h, (g) after calcination at 1100 °C for 5h, and (h) after calcination 1200 °C for 5h.....	61
4.16 XRD patterns of (a) LNF-64 ($y = 0.95$), (b) 8-YSZ, and the powder mixtures between LNF-64 ($y = 0.95$) and 8-YSZ: (c) the mixtures at room temperature, (d) after calcination at 800°C for 5h, (e) after calcination at 900°C for 5h, (f) after calcination at 1000 °C for 5h, and (g) after calcination at 1100 °C for 5h.....	62

Figure	page
4.17 XRD patterns between a 2θ range of $25-36^\circ$ of (a) LNF-64 ($y = 0.95$), (b) 8-YSZ, and the powder mixtures between LNF-64 ($y = 0.95$) and 8-YSZ: (c) the mixtures at room temperature, (d) after calcination at 800°C for 5h, (e) after calcination at 900°C for 5h, (f) after calcination at 1000°C for 5h and (h) after calcination at 1100°C for 5h.....	64
4.18 XRD patterns of (a) LNF-64 ($y = 1.05$), (b) 8-YSZ, and the powder mixtures between LNF-64 ($y = 1.05$) and 8-YSZ: (c) the mixtures at room temperature, (d) after calcination at 800°C for 5h, (e) after calcination at 900°C for 5h, (f) after calcination at 1000°C for 5h and (g) after calcination 1200°C for 5h.....	65
4.19 XRD patterns between a 2θ range of $25-36^\circ$ of (a) LNF-64 ($y = 1.05$), (b) 8-YSZ, and the powder mixtures between LNF-64 ($y = 1.05$) and 8-YSZ: (c) the mixtures at room temperature, (d) after calcination at 800°C for 5h, (e) after calcination at 900°C for 5h, (f) after calcination at 1000°C for 5h and (g) after calcination at 1100°C for 5h.....	67
4.20 SEM Maps (mode-ID-point technique) of the cross-sectioned LNF-64 (MNC method)/8-YSZ pellet after calcination at 900°C for 5 h, detected at (a) point 1, (b) point 2, and (c) point 3.....	69
4.21 SEM Maps (mode-ID-point technique) of the cross-sectioned LNF-64 (MNC method)/8-YSZ pellet after calcination at 1000°C for 5 h, detected at (a) point 1, (b) point 2, and (c) point 3.....	71
4.22 The thermal expansion behavior of LNF-64, prepared by MNC method.....	72
4.23 XRD patterns of $\text{La}_2\text{Ni}_{1-x}\text{Fe}_x\text{O}_4$ ($x=0.0-1.0$) K_2NiF_4 -typed structure, synthesized by WC method after calcined at 700°C for 5h.....	74
4.24 XRD patterns of $\text{La}_2\text{Ni}_{1-x}\text{Fe}_x\text{O}_4$ ($x=0.0-1.0$) K_2NiF_4 -typed structure, synthesized by MWC method and calcined at 700°C for 5h.....	75
4.25 XRD patterns of $\text{La}_2\text{Ni}_{1-x}\text{Fe}_x\text{O}_4$ ($x=0.0-1.0$) K_2NiF_4 -typed structure, synthesized by WC method and calcined at 900°C for 5h.....	76
4.26 XRD patterns of $\text{La}_2\text{Ni}_{1-x}\text{Fe}_x\text{O}_4$ ($x=0.0-1.0$) K_2NiF_4 -typed structure, synthesized by MWC method and calcined at 900°C for 5h.....	77
4.27 Data base of crystal structure La_2NiO_4 from JCPDS: 34-0314.....	78

Figure	page
4.28 The volume of formula unit of $\text{La}_2\text{Ni}_{1-x}\text{Fe}_x\text{O}_4$ ($x = 0.0-1.0$) K_2NiF_4 -typed structure, synthesized by (a) WC (b) MWC, and calcined at $900\text{ }^\circ\text{C}$ for 5h.....	80
4.29 XRD patterns of $\text{L}_2\text{NF-91}$, synthesized by four methods (a) WC (b) MWC (c) NC (d) MNC with the calcinations temperature of $1000\text{ }^\circ\text{C}$ for 5h.....	81
4.30 SEM picture of $\text{L}_2\text{NF-91}$ with the calcination temperature of $1000\text{ }^\circ\text{C}$ for 5 h(a) WC (b) MWC (c) NC (d) MNC	82
4.31 XRD patterns of (a) $\text{L}_2\text{NF-91}$ ($y = 1.00$), (b) 8-YSZ, and the powder mixtures between $\text{L}_2\text{NF-91}$ ($y = 1.00$) and 8-YSZ: (c) the mixtures before calcination, (d) after calcination at 800°C for 5h, (e) after calcination at 900°C for 5h, (f) after calcination at $1000\text{ }^\circ\text{C}$ for 5h, (g) after calcination at $1100\text{ }^\circ\text{C}$ for 5h, and (h) after calcination $1200\text{ }^\circ\text{C}$ for 5h.....	83
4.32 XRD patterns between a 2θ range of $25-36^\circ$ of (a) $\text{L}_2\text{NF-91}$ ($y = 1.00$), (b) 8-YSZ, and the powder mixtures between $\text{L}_2\text{NF-91}$ ($y = 1.00$) and 8-YSZ: (c) the mixtures before calcination, (d) after calcination at 800°C for 5h, (e) after calcination at 900°C for 5h, (f) after calcination at $1000\text{ }^\circ\text{C}$ for 5h, (g) after calcination at $1100\text{ }^\circ\text{C}$ for 5h, and (h) after calcination $1200\text{ }^\circ\text{C}$ for 5h.....	85
4.33 XRD patterns of (a) $\text{L}_2\text{NF-91}$ ($y = 0.95$), (b) 8-YSZ, and the powder mixtures between $\text{L}_2\text{NF-91}$ ($y = 0.95$) and 8-YSZ: (c) the mixtures before calcination, (d) after calcination at 800°C for 5h, (e) after calcination at 900°C for 5h, (f) after calcination at $1000\text{ }^\circ\text{C}$ for 5h, and (g) after calcination at $1100\text{ }^\circ\text{C}$ for 5h.....	86
4.34 XRD patterns between a 2θ range of $25-36^\circ$ of (a) $\text{L}_2\text{NF-91}$ ($y = 0.95$), (b) 8-YSZ, and the powder mixtures between $\text{L}_2\text{NF-91}$ ($y = 0.95$) and 8-YSZ: (c) the mixtures before calcination, (d) after calcination at 800°C for 5h, (e) calcination at 900°C for 5h, (f) calcination at $1000\text{ }^\circ\text{C}$ for 5h, and (g) calcination at $1100\text{ }^\circ\text{C}$ for 5h.....	88

Figure	page
4.35 XRD patterns of (a) L ₂ NF-91 (y = 1.05), (b) 8-YSZ, and the powder mixtures between L ₂ NF-91 (y = 1.05) and 8-YSZ: (c) the mixtures before calcination, (d) after calcination at 800°C for 5h, (e) after calcination at 900°C for 5h, (f) after calcination at 1000 °C for 5h and (g) after calcination at 1100 °C for 5h.....	89
4.36 XRD patterns between a 2θ range of 25-36° of (a) L ₂ NF-91 (y = 1.05), (b) 8-YSZ, and the powder mixtures between L ₂ NF-91 (y = 1.05) and 8-YSZ: (c) the mixtures before calcination, (d) after calcination at 800°C for 5h, (e) after calcination at 900°C for 5h, (f) after calcination at 1000 °C for 5h, and (g) after calcination at 1100 °C for 5h.....	91
4.37 SEM-Mapping (mode-ID-point technique) of the cross-sectioned L ₂ NF-91 (MNC method)/8-YSZ pellet after calcination at 900°C for 5 h. (a) point 1, (b) point 2, and (c) point 3.....	93
4.38 Thermal expansion behavior of L ₂ NF-91 prepared by MNC method.....	94

LIST OF SCHEMES

Scheme	Page
2.2 Schematic diagram showing the mechanism of a solid oxide fuel cell	16



สถาบันวิทยบริการ
จุฬาลงกรณ์มหาวิทยาลัย

LIST OF TABLES

Table	Page
2.1 The seven types of unit cells.....	28
3.1 Chemicals and reagents	33
3.2 A list of the experimental conditions and results for the synthesis of perovskite compounds by water citrate method.....	36
3.3 A list of the experimental conditions and results for the synthesis of perovskite compounds by modified water citrate method.....	37
3.4 A list of the experimental conditions and results for the synthesis of K_2NiF_4 compounds by water citrate method.....	38
3.5 A list of the experimental conditions and results for the synthesis of K_2NiF_4 compounds by modified water citrate method.....	39
4.1 Crystal structures and lattice parameters of $LaNi_{1-x}Fe_xO_3$ ($x = 0.0-1.0$) perovskites, synthesized by WC method and calcined at $700^\circ C$ for 5h	44
4.2 Crystal structures and lattice parameters of $LaNi_{1-x}Fe_xO_3$ ($x = 0.0-1.0$) perovskites, synthesized by MWC method and calcined at $700^\circ C$ for 5h.....	46
4.3 Crystal structures and lattice parameters of $LaNi_{1-x}Fe_xO_3$ ($x = 0.0 - 1.0$) perovskites, synthesized by WC method and calcined at $900^\circ C$ for 5h.....	48
4.4 Crystal structures and lattice parameters of $LaNi_{1-x}Fe_xO_3$ ($x = 0.0 - 1.0$) perovskites, synthesized by MWC method and calcined at $900^\circ C$ for 5h.....	50
4.5 The volume of formula unit of $LaNi_{1-x}Fe_xO_3$ ($x = 0.0-1.0$) perovskites, synthesized by WC and MWC and calcined at $700^\circ C$ for 5h.....	51
4.6 The volume of formula unit of $LaNi_{1-x}Fe_xO_3$ ($x = 0.0-1.0$) perovskites, synthesized by WC and MWC and calcined at $900^\circ C$ for 5h	51
4.7 Particle size-distribution of LNF-64 by four combustion methods.....	57
4.8 The presence of undesired phase(s) in the powder mixtures between LNF-64 ($y = 1.00$) and 8-YSZ after calcination at various temperatures for 5h.....	60

Table	Page
4.9 The presence of undesired phase(s) in the powder mixtures between LNF-64 ($y = 0.95$) and 8-YSZ after calcination at various temperatures for 5h.....	63
4.10 The presence of undesired phase(s) in the powder mixtures between LNF-64 ($y = 1.05$) and 8-YSZ after calcination at various temperatures for 5h	66
4.11 The weight percentage of metallic elements of the cross-sectioned LNF-64 (MNC method)/8-YSZ pellet after calcination at 900°C for 5 h, summarized by SEM-Maps (ID-point technique)	70
4.12 The weight percentage of metallic elements of the cross-sectioned LNF-64 (MNC method)/8-YSZ pellet after calcination at 1000°C for 5 h, summarized by SEM-Maps (ID-point technique)	72
4.13 The thermal expansion coefficients of LNF-64 samples and 8-YSZ at 800 °C.....	73
4.14.1 Crystal structure and lattice parameters of $\text{La}_2\text{Ni}_{1-x}\text{Fe}_x\text{O}_4$ ($x = 0.0-1.0$) K_2NiF_4 -typed structure, synthesized by WC method and calcined at 900 °C for 5h.....	78
4.15 Crystal structure and lattice parameters of $\text{La}_2\text{Ni}_{1-x}\text{Fe}_x\text{O}_4$ ($x = 0.0-1.0$) K_2NiF_4 -typed structure, synthesized by WC method and calcined at 900 °C for 5h	79
4.15 The volume of formula unit of $\text{La}_2\text{Ni}_{1-x}\text{Fe}_x\text{O}_4$ ($x = 0.0-0.1$) K_2NiF_4 -typed structure, synthesized by WC and MWC and calcined at 900 °C for 5h	79
4.16 The presence of undesired phase(s) in the powder mixtures between $\text{L}_2\text{NF-91}$ ($y = 1.00$) and 8-YSZ after calcination at various temperatures for 5h	84
4.18 The presence of undesired phase(s) in the powder mixtures between $\text{L}_2\text{NF-91}$ ($y = 0.95$) and 8-YSZ after calcination at various temperatures for 5h.....	87
4.19 The presence of undesired phase(s) in the powder mixtures between $\text{L}_2\text{NF-91}$ ($y = 0.95$) and 8-YSZ after calcination at various temperatures for 5h	90

Table	Page
4.20 The weight percentage of metallic elements of the cross-sectioned L ₂ NF-91 (MNC method)/8-YSZ pellet after calcination at 900°C for 5 h, summarized by SEM-Maps (ID-point technique).....	93
4.21 The thermal expansion coefficients of L ₂ NF-91 samples and 8-YSZ at 800 °C.....	94



สถาบันวิทยบริการ
จุฬาลงกรณ์มหาวิทยาลัย

LIST OF ABBREVIATIONS

K	Kelvin
°C	Degree Celsius
min	Minute or minutes
μm	Micrometer
Å	Angstrom unit
XRD	X-ray diffraction
SEM	Scanning electron microscopy
SEM-EDX	Scanning electron microscopy-energy dispersive X-ray fluorescence
TEM	Transmission electron microscopy
IS	Impedance Spectroscopy
EPMA	Electron probe microanalysis
h	Hour or hours
wt %	Percent by weight
SOFCs	Solid oxide fuel cells
IT-SOFCs	Intermediate temperature of solid oxide fuel cells
MIECs	Mixed Electronic and Ionic Conductors
ABO ₃	Perovskite structure
A ₂ BO ₄	K ₂ NiF ₄ -typed structure
TEC	Thermal expansion coefficients
COGs	Ceramic oxygen generators
p(O ₂)	Partial pressure of oxygen
8-YSZ	8 mol% Y ₂ O ₃ -stabilized ZrO ₂
TPB	Three-phases boundary
SDC	Samaria-doped ceria
GDC	Gadolinia-doped ceria
LSM	Perovskite containing La,Sr, and Mn
LNF	Perovskite containing La,Ni, and Fe
LSC	Perovskite containing La,Sr, and Co
LSF	Perovskite containing La,Sr, and Fe
LSCF	Perovskite containing La,Sr,Co, and Fe

CHAPTER I

INTRODUCTION

1.1 Background

Each year, the total worldwide energy consumption increases. It has become essential to satisfy this demand, in a way that reduces environmental impact by using fewer non renewable resources. For a growing number of power generators and users, fuel cells are the key to the nation's tomorrow power, offering the solution to some future power generating needs. For instance, fuel cells operate as stand-alone units, and produce clean power without excessive CO₂ emissions [1].

A fuel cell is an electrochemical device that converts the chemical energy in fuels to electricity. Fuel cells are different from batteries in that they consume reactants, which must be replenished, whereas batteries store electrical energy chemically in a closed system. Additionally, while the electrodes of a battery react and change as a battery is charged or discharged, those of a fuel cell remains catalytic with relative stability [2].

Solid oxide fuel cells (SOFCs) currently operate at very high temperatures up to 1000 °C. However, such high temperature operation causes material problems including electrode sintering and interfacial diffusion between electrolytes, electrodes and other highly cost materials [3-5, 10, 22]. One possible way to overcome this problem is to reduce the SOFC operating temperature so called intermediate temperature range (IT-SOFC) [5, 4]. The benefits of using SOFC at lower temperature are (i) to avoid interfacial reactions between an electrode and an electrolyte, which may cause degradation of cell performance, (ii) to avoid sample damages due to thermal expansion mismatch at high processing temperature, (iii) to provide variety of material selection, and (iv) to reduce processing cost [4-9, 11-12, 17-19, 21, 23, 24, 27, 30-32, 36, 63, 76]. The cathode of SOFCs should have high-electronic and ionic conductivities, adequate porosity for gas transport, thermal and chemical compatibilities with the electrolyte, and long-term stability. The development of new mixed ionic–electronic conductors is important for high-temperature electro-chemical applications, including solid oxide fuel cells

(SOFCs), oxygen pumps, sensors, ceramic membranes for high-purity oxygen separation and partial oxidation of hydrocarbons [10-11, 65]. In the case of solid-electrolyte cells such as SOFCs, mixed ionic electronic electrode materials can provide a considerable decrease of polarization losses due to an enlargement of the electrochemical reaction zone. Also, technologies for hydrocarbon oxidation using ceramic-mixed-conductive membranes have been developed by the integration of oxygen separation, steam reforming and partial oxidation of natural gas into one single step [10, 11]. Therefore, the interest is currently being expressed in Mixed Electronic and Ionic Conductors (MIECs), such as perovskite (ABO_3) and K_2NiF_4 -typed structure (A_2BO_4) with high conductivities [5, 6, 10-12, 14, 15, 21, 22, 24].

1.2 Literature reviews of cathode materials selection

1.2.1 Literature reviews of perovskite type structure

Mixed-conducting perovskites are of considerable interest for industrial applications such as cathodes of solid oxide fuel cells and ceramic membranes for high-purity oxygen separation and partial oxidation of hydrocarbons. Technologies of the methane oxidation using dense mixed-conductive membranes permit the integration of oxygen separation, steam reforming, and partial oxidation into a single step for the natural gas conversion. Incorporating divalent metal cations into the A-sublattice of the ABO_3 perovskites results, as a rule, is increasing ionic conductivity and oxygen permeation fluxes, due to the increase in oxygen vacancy concentration. The most important properties of cathodes are their catalytic activity for oxygen reduction and their compatibility with the electrolyte (including thermal expansion match and chemical non-reactivity) [3]. Perovskite type oxides containing Co ions in their B sites are known to have much higher conductivities than those of the most commonly used cathode material $La_{1-x}Sr_xMnO_3$ (LSM) [4-6, 9, 12, 30, 36, 47, 54, 58, 59, 70, 71, 72, 78]. However, the thermal expansion coefficients (TEC) of these materials are much larger ($22.0 \times 10^{-6} K^{-1}$) than that of $La_{0.8}Sr_{0.2}MnO_3$ ($12.0 \times 10^{-6} K^{-1}$) [5]. Although the lanthanum manganite-based materials are not the best because of their low oxide ion diffusivity that lead to the limited electrochemical activity, these are the most common perovskites that are used with 8 mol% Y_2O_3 -stabilized ZrO_2 (8-YSZ) electrolyte at $1000^\circ C$ because of their superior chemical stability [3]. It was reported that, at temperature above $1200^\circ C$, LSM reacted

with 8-YSZ to from $\text{La}_2\text{Zr}_2\text{O}_7$ and/or SrZrO_3 [3, 10, 11, 19, 44, 49, 53, 59, 66, 67, 72, 73, 80] depending on the concentration of strontium in LSM [13].

Zhu *et al.* reported that LaNiO_3 had a very high-electronic conductivity at room temperature; however, it was unstable above 850°C , where it decomposed to La_2NiO_4 and NiO [5].

Hrovat *et al.* showed that LaNiO_3 was stable at high temperature when some of the Ni was substituted by Co or Fe. For example, $\text{La}_{1-y}\text{Sr}_y\text{Ni}_{1-x}\text{Fe}_x\text{O}_3$ was stable up to 1400°C . When the Fe fraction was higher than 0.5, the materials still had a high-electronic conductivity ($\text{La}_{0.4}\text{Sr}_{0.6}\text{Ni}_{0.2}\text{Fe}_{0.8}\text{O}_3$ 435 S/cm at 800°C) and its thermal expansion coefficient (TEC) was close to that of zirconia and ceria electrolytes [7].

Bevilacqua *et al.* investigated three different preparation methods: the glycine nitrate process, the gel citrate complexation route and the coprecipitation route. The glycine nitrate synthesis produced a non-homogenous $\text{LaNi}_{0.6}\text{Fe}_{0.4}\text{O}_3$ material. Good specific conductivity was obtained only after high temperature treatments where the materials were homogenized and sintered. The gel citrate complexation route led to the homogenous $\text{LaNi}_{0.6}\text{Fe}_{0.4}\text{O}_3$ sample, which however was resistant to sinterization/densification. Finally, homogenous $\text{LaNi}_{0.6}\text{Fe}_{0.4}\text{O}_3$ is obtained with coprecipitation synthesis. This synthesis is particularly promising since the morphology of the obtained precipitate favored the sinterization at low temperatures. The benefit of using such low sintering temperature was preventing the undesirable reaction with ZrO_2 -based electrolyte [12].

Falcon *et al.* reported very good catalytic activity of $\text{LaNi}_{1-x}\text{Fe}_x\text{O}_3$ series. The materials were extensively studied using infrared spectroscopy, Mössbauer spectroscopy, magnetic measurement, electrical resistivity measurement and X-ray powder diffraction. The crystal structure in which with $0 \leq x < 0.5$ resembled the structure of LaNiO_3 , crystallized in the rhombohedral system and a space group of $\overline{\text{R3c}}$, while those with composition $0.5 < x \leq 1$ resembled the structure of LaFeO_3 , crystallized in the orthorhombic system and a space group of Pnma . For $\text{LaNi}_{0.5}\text{Fe}_{0.5}\text{O}_3$, the sample was the mixture of the rhombohedral and orthorhombic phases. The cell volume increased with the iron content. This can be ascribed to the larger ionic radius of Fe^{3+} compared to Ni^{3+} . $\text{LaFe}_{0.25}\text{Ni}_{0.75}\text{O}_3$ was found to be single phase when prepared at temperatures as high as 1000°C , indicating

an increase in the stability of the perovskite phase at high temperature when a relatively small amount of Fe (III) was substituted for Ni (III) [14].

In 1999, Provendier *et al.* reported that, within $\text{LaNi}_{1-x}\text{Fe}_x\text{O}_3$ series, the $\text{LaNi}_{0.3}\text{Fe}_{0.7}\text{O}_3$ was the best catalytic activity at the temperature of 800°C [13].

In 2003 Bontempi *et al.*, LaNiO_3 , LaFeO_3 and their solid solution $\text{LaNi}_{0.3}\text{Fe}_{0.7}\text{O}_3$ had been prepared using acetate and citrate salts as precursors. The decomposition of organic substances was obtained by calcination in mild. The symmetry of the phases of LaFeO_3 , $\text{LaNi}_{0.3}\text{Fe}_{0.7}\text{O}_3$ and LaNiO_3 at 700°C is orthorhombic, cubic and rhombohedral respectively [14].

Chiba *et al.* investigated $\text{LaNi}_{1-x}\text{Fe}_x\text{O}_3$ ($x = 0-1.0$) series. It was showed that $\text{LaNi}_{0.6}\text{Fe}_{0.4}\text{O}_3$ mixed oxide exhibited suitable properties as cathode materials for SOFC such as the high electrical conductivity and the thermal expansion coefficient closer to that of Ytria-Stabilized Zirconia (YSZ) electrolyte with respect to that of LSM [5].

Basu *et al.* prepared $\text{LaNi}_{0.6}\text{Fe}_{0.4}\text{O}_3$ using two combustion synthesis routes: citrate-gel (LNC) and urea (LNU). The powders were sintered over a wide temperature range ($900-1400^\circ\text{C}$). The thermal expansion coefficient (TEC), electrical and microstructural characteristics of LNF was thoroughly investigated. Electrical conductivities were found to be one and a half times higher than that of most commonly used cathode material, $\text{La}(\text{Sr})\text{MnO}_3$. Moreover, the TEC value of $\text{LaNi}_{0.6}\text{Fe}_{0.4}\text{O}_3$ was found to be $\approx 11.4 \times 10^{-6} \text{ K}^{-1}$ at 800°C . The study opened up a possibility of using LNF as a promising cell component for SOFC [18].

Zhen *et al.* stated that $\text{La}(\text{Ni}_{0.6}\text{Fe}_{0.4})\text{O}_3$ perovskite material has been developed as one of most promising cathode materials for the intermediate temperature-solid oxide fuel cells (IT-SOFCs) because it has high electrochemical activity for the oxygen reduction reaction and a thermal expansion coefficient close to that of zirconia electrolyte [19].

Proskurnina *et al.* synthesized $\text{LaNi}_{1-x}\text{Fe}_x\text{O}_3$ ($0 \leq X \leq 1$) with the step of $x = 0.05$ at 1100°C in air. According to the results of XRD, the homogeneity range of $\text{LaNi}_{1-x}\text{Fe}_x\text{O}_3$ solid solution laid within $0.6 \leq X \leq 0.8$ in the crystal structure with $\overline{\text{R}3\text{c}}$ space group, similar to the parent LaNiO_3 (rhombohedral structure) [18].

Knudsen *et al.* investigated the influence of A-site stoichiometry on phase stability and electrical conductivity of the perovskite based series $\text{La}(\text{Ni}_{0.59}\text{Fe}_{0.41})\text{O}_{3-\delta}$ for cathode current collection in solid oxide fuel cells. X-ray

diffraction and DC electrical conductivity studies were performed on samples, prepared by the glycine nitrate combustion method. Reaction between $\text{La}_{0.99}(\text{Ni}_{0.59}\text{Fe}_{0.41})\text{O}_{3-\delta}$ and $(\text{La}_{0.85}\text{Sr}_{0.15})_{0.91}\text{MnO}_{3-\delta}$ resulted in a single perovskite material when the compounds were co-sintered. The interface between a screen-printed layer of $\text{La}_{0.99}(\text{Ni}_{0.59}\text{Fe}_{0.41})\text{O}_{3-\delta}$ and a layer of $\text{Ce}_{0.9}\text{Gd}_{0.10}\text{O}_{3-\delta}/(\text{La}_{0.85}\text{Sr}_{0.15})_{0.91}\text{MnO}_{3-\delta}$ composite has been investigated and the extent of the reaction zone determined by energy dispersive X-ray spectroscopy [20].

The doping with nickel has been established to increase oxygen nonstoichiometry and permeation fluxes of the perovskite-like solid solutions of $\text{LaCo}(\text{Fe},\text{Ni})\text{O}_{3-\delta}$ and $\text{LaGa}(\text{Ni})\text{O}_{3-\delta}$. Kharton *et al.* reported that incorporation of nickel into the iron sublattice of LaFeO_3 , resulting in the increase of oxygen nonstoichiometry, electrical conductivity, and thermal expansion of the perovskites. Activation energy for electrical conductivity of the $\text{LaFe}_{1-x}\text{Ni}_x\text{O}_3$ ($x = 0.2-0.5$) decreased with the increase of x in the range from 23.9 to 6.6 kJ/mol, respectively. Thermal expansion coefficients of these materials calculated from the dilatometric data were $(8.9-11.9) \times 10^{-6} \text{ K}^{-1}$. Oxygen permeation through $\text{LaFe}_{1-x}\text{Ni}_x\text{O}_3$ membranes was found to increase with nickel content due to increasing oxygen vacancy concentration and bulk ionic conductivity, which are the permeation flux-limiting factors [21].

Komatsu *et al.* reported that the relationship between the chemical compatibility and electrochemical properties of $\text{La}_{0.6}\text{Sr}_{0.4}\text{Fe}_{0.8}\text{Co}_{0.2}\text{O}_3$ (LSCF), $\text{LaNi}_{0.6}\text{Fe}_{0.4}\text{O}_3$ (LNF), and $\text{La}_{0.8}\text{Sr}_{0.2}\text{MnO}_3$ (LSM) as a cathode against the Cr poisoning condition. Powder mixtures of LSCF- Cr_2O_3 , LSM- Cr_2O_3 and LNF- Cr_2O_3 were heated at 1073 K and analyzed by X-ray powder diffraction with the Rietveld refinement. It was found that LNF powder was less reactive with Cr_2O_3 than LSCF and LSM powder from the viewpoint of the consumption of Cr_2O_3 in the mixtures. Therefore, LNF is expected to be a long-life cathode with high stability against Cr poisoning in solid oxide fuel cell because of the low reactivity with Cr_2O_3 [22].

1.2.2 Literature reviews of K_2NiF_4 -typed structure

A_2BO_4 compounds (A, rare earth and/ or alkaline earth and B, transition metal) with K_2NiF_4 -typed structure have been the targets of intensive studied because of their structure similarity to the La_2NiO_4 , $La_{2-x}Sr_xCuO_4$, La_2CuO_4 superconductors [25, 28, 35]. This structure consists of layers of ABO_3 separated by AO layers in which it is possible to incorporate excess oxygen in the unusual from of an interstitial species. This excess of oxygen provides an attractive alternative to the vacancy-based conduction mechanism present in the perovskite and fluoride oxides where the dopant-vacancy interaction can limit the observed conductivity. Compared to perovskites, this layered structure has a particular interest because it allows great flexibility in the oxygen stoichiometry [24]. Results on oxygen permeation through dense ceramics of K_2NiF_4 -typed materials suggested two significant contributions to the ionic conductivity of the oxygen-hyperstoichiometric phases with K_2NiF_4 -typed structure. The oxygen interstitial migration in the rock-salt-type layers of the K_2NiF_4 like lattice increases with increasing temperature; where as, the oxygen vacancy diffusion in the perovskite layers decreased when temperature increased [10]. The electrical conductivity of the A_2BO_4 oxides was of p-type and reached values close to 100 S cm^{-1} at high oxygen partial pressures at $800 \text{ }^\circ\text{C}$ for nickelates and cobaltites [26].

$LaNiO_3$ exhibits high electronic conductivity at room temperature, but decomposes at elevated temperature into the K_2NiF_4 -typed structure La_2NiO_4 and NiO, with a reduction in conductivity [5, 6, 21]. A_2BO_4 oxides with the perovskite related K_2NiF_4 -typed structure have not been intensively investigated. Recently Daroukh *et al.* reported that the thermochemical stability of A_2BO_4 oxides ($A_{2-\alpha}A'_\alpha BO_4$, A = La, A' = Sr, B = Mn, Fe, Co, Ni) was higher than that of the perovskite ABO_3 oxides, and the thermal expansion of A_2BO_4 oxides was generally lower than that of the ABO_3 oxides with comparable cationic compositions. This implies that A_2BO_4 oxides are very likely to be the new type of cathode materials of IT-SOFCs [24, 29, 32, 33]. Recent studies on mixed conductors indicated that the K_2NiF_4 -typed structure have promising properties at intermediate operation temperatures due to their high ionic conduction and their high electrocatalytic activity [30, 36].

The oxide phases existing in the ternary La–Ni–O system included perovskite-type $LaNiO_{3-\delta}$ and Ruddlesden–Popper series [28, 30] $La_{n+1}Ni_nO_{3n+1}$; with

$\text{La}_2\text{NiO}_{4+\delta}$ having a K_2NiF_4 -typed structure as the end-member ($n = 1$). Oxygen-deficient $\text{LaNiO}_{3-\delta}$ exhibited a metallic conductivity, which was as high as about 10^3 S cm^{-1} at room temperature; however, in a narrow range of temperatures and oxygen partial pressures this phase decomposes into $\text{La}_{n+1}\text{Ni}_n\text{O}_{3n+1}$ and NiO at temperatures above 1100 K in air. The La_2NiO_4 phase is oxygen-hyperstoichiometric, a result of incorporation of interstitial oxygen anions into the rock-salt layers of intergrowth K_2NiF_4 -typed structure. In air, the equilibrium oxygen nonstoichiometry was 0.14–0.16 at 300K [26, 29, 33, 37, 41, 43] and decreased on heating. At temperatures below 600 K, $\text{La}_2\text{NiO}_{4+\delta}$ exhibited a semiconductor-type electronic conductivity, which occurred via hopping of p-type charge carriers between mixed-valence nickel cations; a smooth change to metallic-like conduction was observed at higher temperatures [28].

In 2000, Skinner *et al.* found that $\text{La}_2\text{NiO}_{4+\delta}$ have an oxygen diffusivity higher than that of $\text{La}_{0.6}\text{Sr}_{0.4}\text{Co}_{0.2}\text{Fe}_{0.8}\text{O}_3$ (LSCF). The fast oxide ion diffusion of $\text{La}_2\text{NiO}_{4+\delta}$ combined with its thermal stability indicated that this material would be a good candidate for use in ceramic oxygen generators (COGs) and solid oxide fuel cells (SOFCs) [10, 24, 30, 36, 39]. Oxygen permeability of K_2NiF_4 -typed phases such as $\text{La}_2\text{Ni}_{0.98}\text{Fe}_{0.02}\text{O}_{4+\delta}$, exhibited maximum ionic transport, $\text{La}_2\text{Ni}_{0.88}\text{Fe}_{0.02}\text{Cu}_{0.10}\text{O}_{4+\delta}$ and $\text{La}_2\text{Cu}_{0.9}\text{Co}_{0.10}\text{O}_{4+\delta}$, in about one order of magnitude lower than that of most permeable perovskite typed materials. The decreasing radii of the rare-earth cations in the A-sublattice of cuprates and nickelates led to a dramatic decrease in ionic transport, similar to perovskite oxides. Thermal expansion coefficients of the title materials varied in the range $(10.1\text{--}13.4) \times 10^{-6} \text{ K}^{-1}$ [10].

In 2003, Daroukh *et al.* confirmed that the thermal expansion coefficients of K_2NiF_4 -typed oxides were generally lower than the coefficients of the perovskite type oxides of comparable cationic compositions. The comparison of the oxidation states of AMO_{3-x} and $\text{AMO}_{3-x}\cdot\text{AO}$ gave evidence on the stabilizing influence of the AO interlayer on the perovskite layer. Comparable compositions of the perovskite and the K_2NiF_4 -type structure showed the higher oxygen to metal stoichiometries at low oxygen partial pressures for the K_2NiF_4 -typed structures, e.g. $\text{La}_{0.5}\text{Sr}_{0.5}\text{MnO}_{3-x}\cdot\text{SrO}$, demonstrating higher thermodynamic stability than that of $\text{La}_{0.5}\text{Sr}_{0.5}\text{MnO}_{3-x}$ [26].

Huang *et al.* reported that the preferred sintering temperature of $\text{La}_2\text{NiO}_{4+\delta}$ was ascertained to be 1300 °C with regard to the electrical conducting properties. $\text{La}_2\text{NiO}_{4+\delta}$ ceramic sintered at 1300 °C presented a generally uniform microstructure together with electrical conductivities of 76–95 S cm⁻¹ at 600–800 °C [29].

Recently, $\text{La}_2\text{NiO}_{4+\delta}$ was reported to show good performance in terms of electronic conductivity and thermal expansion properties [29, 32]. In 2003 Li *et al.* reported that a complex sol–gel processing was effective in fabricating dense supported membrane for oxygen permeation. Mixed conductor $\text{La}_2\text{NiO}_{4+\delta}$ was synthesized by complex sol–gel approach. Its dense membranes were obtained by coating the sol on porous alumina substrates followed by heat treatment. The supported membranes exhibited a much better performance in oxygen permeability than that of bulk membranes made from same material, showing a great potential for the application in both air separation and catalytic membrane reactor [29]. In 2004 $\text{La}_2\text{Ni}_{0.8}\text{Fe}_{0.2}\text{O}_4$ was synthesized by complex sol-gel approach its dense membranes were successfully obtained by coating the sol on porous alumina substrates followed by heat treatment. The oxygen permeation flux of supported $\text{La}_2\text{Ni}_{0.8}\text{Fe}_{0.2}\text{O}_4$ membranes is greater than 1.0×10^{-6} mol cm⁻²s⁻¹ at 750 K, which is appropriately ten times higher than that for Fe-free supported La_2NiO_4 membranes and 100 times higher than that for La_2NiO_4 bulk membranes under the experimental conditions [41].

Amow *et al.* [2004] investigated on the parent nickelate, $\text{La}_2\text{NiO}_{4+\delta}$, which is made up of alternating LaNiO_3 perovskite and La_2O_2 rock salt layers. Significant excess oxygen, δ , can be incorporated into the rock-salt layer as interstitial defects. A series of structural changes from tetragonal to orthorhombic symmetry may be induced by varying the amount of excess oxygen in the rock-salt layer. The solid solution $\text{La}_2\text{Ni}_{1-x}\text{Co}_x\text{O}_{4+\delta}$, was successfully prepared by the Pechini method using both conventional and microwave heating. Successive substitution of cobalt for nickel in this series led to a structure phase transition from tetragonal F4/mmm ($x = 0-0.5$) to orthorhombic Bmab ($x = 0.6-1.0$) [36].

Munnings *et al.* [2004] reported that the $\text{La}_2\text{NiO}_{4+\delta}$ material underwent a reversible transition from the orthorhombic Fmmm structure to the tetragonal I4/mmm structure on heating [37].

Skinner *et al.* prepared $\text{La}_{2-x}\text{Sr}_x\text{NiO}_{4+\delta}$, $x = 0, 0.1$ with an oxygen excess of up to $\delta = 0.24$. The oxygen tracer diffusion coefficient and surface exchange coefficient of the materials were determined by the isotope exchange depth profile method (IEDP). $\text{La}_2\text{NiO}_{4+\delta}$ was found to have an oxygen diffusivity higher than that of $\text{La}_{0.6}\text{Sr}_{0.4}\text{Co}_{0.2}\text{Fe}_{0.8}\text{O}_3$ (LSCF) and a one order of magnitude lower than that of the best perovskite oxide ion conductor $\text{La}_{0.3}\text{Sr}_{0.7}\text{CoO}_3$ (LSC). The fast oxide ion diffusion of $\text{La}_2\text{NiO}_{4+\delta}$ combined with its thermal stability indicated that this material would be a good candidate for use in ceramic oxygen generators (COGs) and solid oxide fuel cells (SOFCs) [39].

In 2007, Zhao *et al.* studied $\text{La}_2\text{Ni}_{0.8}\text{Co}_{0.2}\text{O}_{4+\delta}$ as the cathodes for SOFCs with doped ceria as the electrolytes. In addition, a site was doped with Sr to improve the electrode performance. Emphasis was laid on the optimization of Sr doped $\text{La}_2\text{Ni}_{0.8}\text{Co}_{0.2}\text{O}_{4+\delta}$ composite cathodes [40].

Cheng *et al.* reported the supported dense oxygen permeating membrane of mixed conductor $\text{La}_2\text{Ni}_{0.8}\text{Fe}_{0.2}\text{O}_{4+\delta}$ can be prepared by sol-gel method. The oxygen permeation flux of supported $\text{La}_2\text{Ni}_{0.8}\text{Co}_{0.2}\text{O}_{4+\delta}$ membranes was greater than $1.0 \cdot 10^{-6} \text{ mol cm}^{-2} \text{ s}^{-1}$ at 750 K, which was appropriately ten times higher than that for Fe-free supported $\text{La}_2\text{NiO}_{4+\delta}$ membranes and 100 times higher than that for $\text{La}_2\text{NiO}_{4+\delta}$ bulk membranes under the experimental conditions [41].

In 2007, Tsipis *et al.* studied the oxygen hyperstoichiometry of K_2NiF_4 -type $\text{La}_2\text{Ni}_{0.9}\text{Fe}_{0.1}\text{O}_{4+\delta}$ by thermogravimetric analysis and coulometric titration in the oxygen partial pressure range $6 \times 10^{-5} - 0.7 \text{ atm}$ at 923-1223 K. The value of the oxygen hyperstoichiometry was considerably higher than that of undoped lanthanum nickelate. The stability of La_2NiO_4 -based phase in reducing atmospheres was essentially unaffected by doping Fe ions [42]. In 2008, the some group *et al.* found that the doping of iron in K_2NiF_4 -typed lanthanum nickelate increased oxygen-ion mobility at 1173–1223 K, whilst activation energies remained essentially similar at 69–80 kJ/mol. At lower temperatures, the surface kinetics and ionic transport in $\text{La}_2\text{Ni}_{0.9}\text{Fe}_{0.1}\text{O}_{4+\delta}$ became both slower than those in $\text{La}_2\text{NiO}_{4+\delta}$, due to the possible defect-interaction [43].

1.2.3 Literature reviews of chemical and physical compatibility of cathode with the 8-YSZ electrolyte

One of the reason that make the perovskite typed structure and K_2NiF_4 -typed structure of interest as a cathode for SOFC is their relatively good chemical compatibility with 8 mol% Y_2O_3 -stabilized ZrO_2 (8-YSZ) electrolyte [4, 10, 27]. The perovskite $La_{1-x}Sr_xMnO_{3-\delta}$ (LSM) cathode has been used as a typical cathode material on electrolyte because it has low chemical reactivity and good TEC compatibility with the 8-YSZ. However, lowering of the operating temperature of SOFC below 700 °C the overpotential of LSM increased significantly, due to its relatively low reaction rate of oxygen reduction in that temperature range. On the other hand, the $La_{1-x}Sr_xCoO_{3-\delta}$ (LSC) cathode provides a higher reaction rate of oxygen reduction with an enlargement of the reaction sites. However, undesirable resistive phases such as $La_2Zr_2O_7$ or $SrZrO_3$ [4, 12, 13, 21, 23, 45, 54, 60, 67, 68, 72, 73, 75] are easily formed at the interface between the cathode and the electrolyte when the LSC cathode is directly applied onto the 8-YSZ electrolyte. The practical properties of LSC from thermal cycling and/or long-term operation become degraded due to the mismatch of the thermal expansion and the chemical reactivity between 8-YSZ and LSC. These issues have been extensively investigated in an effort to overcome the problems of the compatibility between cathodes and 8-YSZ electrolyte.

In 1999, Chiba *et al.* investigated the effect of doping in $LaNi_{0.6}M_{0.4}O_3$ (M = Al, Cr, Mn, Fe, Co, Ga) and $LaNi_{1-x}Fe_xO_3$ (x = 0.0–1.0) [5, 6, 12, 14–20, 22]. It was shown that $LaNi_{1-x}Fe_xO_3$ mixed oxides exhibited high electrical conductivity [5, 12, 14–20, 53] and thermal expansion coefficient closer to that of 8-YSZ electrolyte with respect to LSM [5, 12, 18, 19, 20, 53]. $LaNi_{1-x}Fe_xO_3$ materials were tested as cathodes in SOFCs with 8-YSZ and SASZ (Alumina-doped Scandia-Stabilized Zirconia) [2, 51]. However, the reaction with the electrolyte above 1000 °C resulted in the formation of a $La_2Zr_2O_7$ insulating layer [50, 53].

The electrical properties of $La_2Zr_2O_7$ had been reported in the literature [45, 46, 48, 53, 73]. Lee *et al.* reported the formation of new phase at the $La_{0.9}Sr_{0.1}MnO_3$ /YSZ interface that affected on the cathodic performances at 900 °C in air. The resistance caused by the interfacial product layer kept increasing with time to reach up to 40% of the total resistance after 500 h. The interfacial product was identified as $La_2Zr_2O_7$ by XRD measurement. The electrical conductivity of $La_2Zr_2O_7$ ($2.4 \times 10^{-5} \text{ S cm}^{-1}$ at 1000 °C) was 4 to 7 orders of magnitude smaller than those of

$\text{La}_{0.9}\text{Sr}_{0.1}\text{MnO}_3$ electrode with 8-YSZ electrolyte. Combining these results, a conclusion was made that the cathodic degradation came mainly from the growth of interfacial product layer and its contribution to the cell resistance [45].

In 1996, Kindermann *et al.* reported that the chemical compatibility of the LaFeO_3 based perovskites, $\text{La}_{0.6}\text{Sr}_{0.4}\text{Fe}_{0.8}\text{M}_{0.2}\text{O}_{3-\delta}$ and $(\text{La}_{0.6}\text{Sr}_{0.4})_{0.9}\text{Fe}_{0.8}\text{M}_{0.2}\text{O}_{3-\delta}$ ($\text{M} = \text{Cr}, \text{Mn}, \text{Co}, \text{Ni}$), with 8-YSZ powder mixtures by annealing at 1000°C for time periods up to 1300 h. The annealed samples were analyzed by XRD and SEM/EDS. The formation of monoclinic ZrO_2 was not observed in Co or Ni containing samples. Following the loss of strontium in significant amounts from these samples, La rich compositions were formed and reacted further with zirconia to form $\text{La}_2\text{Zr}_2\text{O}_7$ [46].

In 2000, Kostogloudis *et al.* reported the chemical reactivity of perovskite oxide SOFC with 8-YSZ. The perovskite oxides of interest $\text{La}_{1-x}\text{Sr}_x\text{Co}_{0.2}\text{Mn}_{0.8}\text{O}_{3-\delta}$, $\text{La}_{1-x}\text{Sr}_x\text{Co}_{0.2}\text{Fe}_{0.8}\text{O}_{3-\delta}$, $\text{La}_{1-x}\text{Ca}_x\text{Co}_{0.2}\text{Fe}_{0.8}\text{O}_{3-\delta}$ ($0 \leq X \leq 0.5$), the A-site deficient oxides $\text{La}_{0.6-z}\text{Sr}_{0.4}\text{Co}_{0.2}\text{Fe}_{0.8}\text{O}_{3-\delta}$, $\text{La}_{0.6}\text{Sr}_{0.4-z}\text{Co}_{0.2}\text{Fe}_{0.8}\text{O}_{3-\delta}$ and $(\text{La}_{0.6-z}\text{Sr}_{0.4})_{1-z}\text{Co}_{0.2}\text{Fe}_{0.8}\text{O}_{3-\delta}$ ($0 \leq Z \leq 0.2$). The XRD patterns of the perovskite/8-YSZ mixtures, after annealed at 1000°C for 120h, identified the presence of $\text{La}_2\text{Zr}_2\text{O}_7$ and $(\text{Sr}/\text{Ca})\text{ZrO}_3$. The contraction of lattice parameters of 8-YSZ was found, due to the diffusion of the transition metal cations from the perovskite into 8-YSZ [48].

Simner *et al.* [2003] studied the reactivity of $\text{La}_{0.8}\text{Sr}_{0.2}\text{FeO}_{3-\delta}$ and 8-YSZ at 1400°C for 2 h. While XRD data of $\text{La}_{0.8}\text{Sr}_{0.2}\text{FeO}_{3-\delta}$ /8-YSZ reaction mixtures indicated no apparent formation of the poorly conducting La and /or Sr-zirconate phases, it did reveal a significant peak shift in the LSF diffraction pattern after reaction above 1000°C , which appeared to correspond to the dissolution of Zr cations into the perovskite. The electrical conductivity of the Zr containing LSF was substantially reduced [49].

Basu *et al.* [2004] found the formation of a thick white gas-tight film at the interface between the zirconia (electrolyte) and $\text{LaNi}_{0.6}\text{Fe}_{0.4}\text{O}_3$ /8-YSZ, resulting to no voltage output when electrochemical tests are performed. This white layer started to form at $\sim 1300^\circ\text{C}$ and became thicker and thicker as the sintering temperature increased. Quantitative EDX and XRD analysis confirmed that it was $\text{La}_2\text{Zr}_2\text{O}_7$. [53].

Yang *et al.* [2006] studied the reaction occurs in the 8-YSZ thin film, electrophoretic deposited on the $\text{La}_{0.8}\text{Sr}_{0.2}\text{O}_3$ (LSM) substrate. The characterizations were conducted by zeta potential analysis, X-ray diffraction (XRD), scanning electron microscopy (SEM), and transmission electron microscopy (TEM). The $\text{La}_2\text{Zr}_2\text{O}_7$,

formed at the interface between the 8-YSZ thin film and LSM substrate after sintered at 1400°C for 52 h, was identified by XRD. $\text{La}_2\text{Zr}_2\text{O}_7$ with the thickness of 200 nm was formed at the interface between the YSZ film and the LSM substrate [72].

Sahu *et al.* studied the chemical compatibility of LSM with 8-YSZ using X-ray diffraction (XRD) and electron probe microanalysis (EPMA) techniques. No secondary phases such as lanthanum zirconate and strontium zirconate were observed in the XRD patterns of powder mixtures even after firing at 1400 °C for 6h. These results were further confirmed by EPMA studies. In other words, the LSM prepared were found to have good chemical compatibility with YSZ [13].

Anderson *et al.* reported the reactivity of $\text{Ln}_{0.8}\text{Sr}_{0.2}\text{O}_3$ ($\text{Ln} = \text{Sm}, \text{Pr}, \text{Nd}$ and a mixed lanthanide precursor) and $\text{La}_{0.8}\text{Sr}_{0.2}\text{O}_3$ ($\text{M} = \text{Ba}, \text{Ca}$) cathodes with 8-YSZ electrolyte. From this study, the most promising candidate was probably $\text{La}_{0.8}\text{Ca}_{0.2}\text{FeO}_3$ since it exhibited the least dissolution of Zr into the provskite at 1200°C, compared to the other compositions [51].

Smith *et al.* investigated the effects of microstructural and interfacial changes on the cathodic reaction occurring and times ranging at the LSM/8-YSZ interface by AC impedance spectroscopy. These effects were induced by using harsh anneals of temperatures ranging from 1250 to 1400 °C from 1 to 48h. The magnitude of the resistance of this semicircle was shown to be dependent on the time and temperature of the applied anneal. Extended interfacial pores were also shown to occur in 1400 °C annealed samples [55].

Kim *et al.* studied on the anode-supported SOFCs for intermediate temperatures, involving $\text{La}_{0.6}\text{Sr}_{0.4}\text{Co}_{0.2}\text{Fe}_{0.8}\text{O}_{3-\delta}$ (LSCF) based cathodes, 8-YSZ electrolyte, and $\text{Ce}_{0.8}\text{Gd}_{0.2}\text{O}_{2-\delta}$ (GDC). The GDC interlayer between the LSCF cathode and 8-YSZ electrolyte was used to prevent formation of insulating phases such as SrZrO_3 or $\text{La}_2\text{Zr}_2\text{O}_7$ [60].

Zhao *et al.* reported that the thermal expansion coefficient (TEC) of $\text{La}_{0.6}\text{Sr}_{0.4}\text{CoO}_{3-\delta}$ (LSC) ($\sim 23 \times 10^{-6} \text{ K}^{-1}$) is much higher than those of typical SOFC electrolytes, such as 8-YSZ [63].

Kawada *et al.* reported the reactivity between LaMnO_3 and 8-YSZ. Electrical conductivity of 8-YSZ decreased when Mn dissolved in the cubic phase of 8-YSZ. Oxidation state of the dissolving Mn varied with partial pressure of oxygen and affected the electrical properties of 8-YSZ [67].

Nasrallah *et al.* explored the chemical compatibility of $\text{La}_{1-x}\text{Sr}_x\text{Co}_{1-y}\text{Fe}_y\text{O}_3$ system with 8-YSZ and found that the stoichiometric compositions, i.e. $z = 0$, for a particular range of x and y showed no reaction with 8-YSZ [71].

Orui *et al.* investigated electrochemical properties of the LNF-SDC composite cathode combined with an 8-YSZ electrolyte in order to reveal effects of the composite microstructure on the cell performance [73].

Nie *et al.* studied on preparation, thermal expansion, chemical compatibility, electrical conductivity and polarization of K_2NiF_4 -typed $\text{A}_{2-\alpha}\text{A}'_{\alpha}\text{MO}_4$ ($\text{A} = \text{Pr}, \text{Sm}$; $\text{A} = \text{Sr}$; $\text{M} = \text{Mn}, \text{Ni}$; $\alpha = 0.3, 0.6$). The results showed a low reactivity with 8-YSZ. The thermal expansion coefficient (TEC) values were changed with the ionic radius of A. The specific conductivities of the nickelates were higher than those of manganites. While the nickelates showed a lower cathodic polarization in comparison with manganites [79].

Although there were some reports on synthesis and properties of lanthanum nickel iron oxides, the effect of different synthetic methods had not been conducted thoroughly for both perovskites and K_2NiF_4 -typed structures. Furthermore the compatibility of both structures were not compared.

In this thesis, the full series were investigated and some selected metal oxides of both structures tested on the thermal stabilities, and compatibility with 8-YSZ.

1.3 The objectives of this study

1. To prepare the single-phased $\text{LaNi}_{1-x}\text{Fe}_x\text{O}_3$ (perovskite structure; LNF) and $\text{La}_2\text{Ni}_{1-x}\text{Fe}_x\text{O}_4$ (K_2NiF_4 -typed structure; L_2NF) with $x = 0.0-1.0$ by using the water citrate and modified water citrate methods.

2. To compare the effect of using four combustion methods: (i) water citrate (WC), (ii) modified water citrate (MWC), (iii) nitric citrate (NC), (ii) modified nitric citrate (MWC) in the synthesis of the selected LNF perovskites in terms of structures and particle sizes.

3. To study the chemical compatibility of the LNF/ L_2NF and 8-YSZ using XRD and SEM/EDX to follow the reaction occurred at higher temperatures up to 1200°C .

4. To study the physical compatibility of the LNF/L₂NF and 8-YSZ in a term of their similarity in thermal expansion coefficients.



สถาบันวิทยบริการ
จุฬาลงกรณ์มหาวิทยาลัย

CHAPTER II

THEORY

A fuel cell is an electrochemical device that converts the chemical energy in fuels (such as hydrogen, methane, butane or even gasoline and diesel) into electrical energy by exploiting the natural tendency of oxygen and hydrogen to react. By controlling the means by which such a reaction occurs and directing the reaction through a device, it is possible to harvest the energy given off by the reaction. Fuel cells are simple devices, containing no moving parts and only four functional component elements: cathode, electrolyte, anode and interconnect. Much development has focused on solid oxide fuel cells (SOFC), both because they are able to convert a wide variety of fuels and because they do so with such high efficiency (40-60% unassisted, up to 70% in pressurized hybrid system) compared to engines and modern thermal power plants (30-40% efficient) [1-3]. SOFCs are attractive as energy sources because they are clean, reliable, and almost entirely nonpolluting. Because there are no moving parts and the cells are therefore vibration-free, the noise pollution associated with power generation is also eliminated.

The SOFC has been in development since the late 1950s and has two configurations that are being investigate: planar (flat panel) and tubular [1, 65].

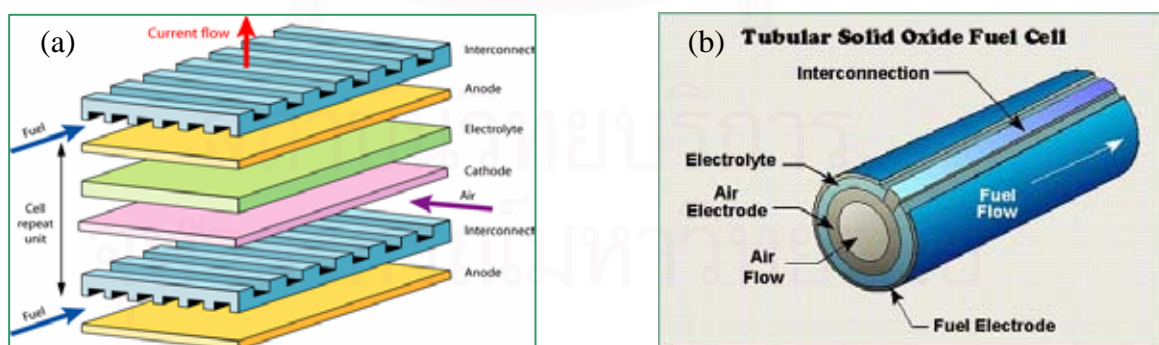


Figure 2.1 Solid oxide fuel cells with two configurations (a) Flat panel [2]
(b) Tubular [3].

The SOFC is currently the highest-temperature fuel cell in development and can be operated over a wide temperature range from 600°C–1000°C allowing a number of fuels to be used. To operate at such high temperatures, the electrolyte is a thin, solid ceramic material (solid oxide) that is conductive to oxygen ions (O^{2-}).

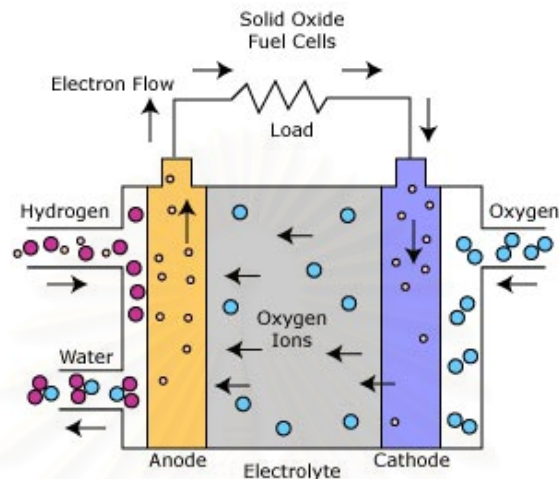
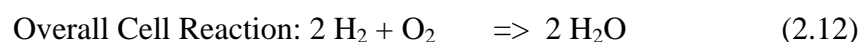
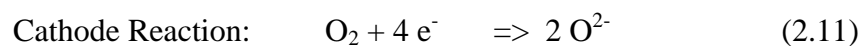
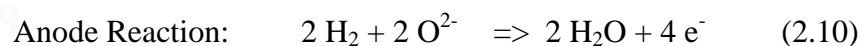


Figure 2.2 Schematic diagram showing the mechanism of a solid oxide fuel cell [1].

The cell is constructed with two porous electrodes which sandwich an electrolyte member. Air flows along the cathode (which is therefore also called the "air electrode"). When an oxygen molecule contacts the cathode/electrolyte interface, it catalytically acquires four electrons from the cathode and splits into two oxygen ions. The oxygen ions diffuse into the electrolyte material and migrate to the other side of the cell where they encounter the anode (also called the "fuel electrode"). The oxygen ions encounter the fuel at the anode/electrolyte interface and react catalytically, giving off water, heat, and most importantly electrons. The electrons transport through the anode to the external circuit and back to the cathode, providing a source of useful electrical energy in an external circuit.



The very high operating temperature of the SOFC has both advantages and disadvantages. The high temperature enables them to tolerate relatively impure fuels, such as those obtained from the gasification of coal or gasses from industrial process and other sources. However, the high temperatures require more expensive materials of construction.

2.1 Materials Issues (SOFC)

2.1.1 Cathode (Air Electrode) and Anode (H₂/CO Electrode)

1. High electronic conductivity
2. Chemical and mechanical stability (at 600-1000 °C in oxidizing conditions for the cathode and in highly reducing conditions for the anode)
3. Thermal expansion coefficient that matches that of electrolyte
4. Sufficient porosity to facilitate transport of O₂ from the gas phase to the electrolyte

2.1.2 Electrolyte (Air Electrode)

1. Free of porosity
2. High oxygen ion conductivity
3. Very low electronic conductivity

2.1.3 Interconnect (between Cathode and Anode)

1. Free of porosity
2. High electronic conductivity and negligible ionic conductivity
3. Stable in both oxidizing and reducing atmospheres
4. Chemical and thermal expansion compatibility with other Components

One of the major problems encountered today to develop intermediate temperature solid fuel cells (IT-SOFC) is the large cathode overpotential caused by the reduced operation temperature. Mixed ionic and electronic conductors (MIECs) have been widely studied as cathodes for IT-SOFC. The electrical overpotential on the MIEC oxide cathode presents a combined activation barrier of many underlying transport processes that contributes significantly to the total energy loss, particularly at low operating temperature. Therefore, it is very important to understand the knowledge on the mechanism and kinetics of the oxygen exchange with MIEC to

improve the development of cathode materials for this technology. The elementary steps in the cathodic oxygen reduction reaction on a mixed conducting electrode material can be resumed as follows [32]:

1. Diffusion of O₂ molecules in the gas phase to the electrode
2. Adsorption of O₂ on the surface of the electrode
3. Dissociation of molecular into atomic oxygen species
4. Charge transfer from the electrode to oxygen species before or after dissociation
5. Incorporation of oxide ions in the crystal lattice of the electrode
6. Bulk transportation of O²⁻ ions through the electrode to the electrode/electrolyte interface
7. Transportation of O²⁻ ions across the electrode/electrolyte interface

Cathodes for solid oxide fuel cells (SOFCs) have to possess many properties including high electrical conductivity, high catalytic activity for oxygen reduction, and compatibility with other cell components. In the earliest stages of SOFC development, platinum was used as cathode since other appropriate materials were not available. However, platinum is expensive and its use in cost-effective commercial SOFCs for power generation is not practical. Less expensive perovskites and K₂NiF₄-typed methods also poses the required properties and have consequently attracted much interest.

2.2 Physical and physicochemical properties of cathode materials

2.2.1 Perovskite-type structure

Perovskite is one of the most frequently encountered structures in solid-state inorganic chemistry, and it accommodates most of the metallic ions in the periodic table with a significant number of different anions. An ideal perovskite structure has an ABO₃ stoichiometry and a cubic crystal structure, which is composed of a three-dimensional framework of corner-sharing BO₆ octahedron. The A-site cation fills the 12 coordinate cavities formed by the BO₃ network and is surrounded by 12 equidistant anions [4, 56, 57, 81], as seen in Figure 2.3.

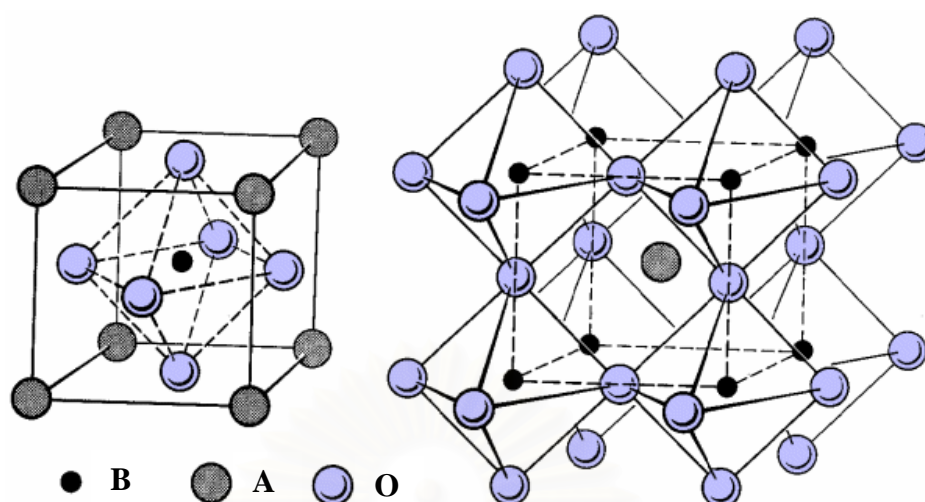


Figure 2.3 Ideal perovskite structure illustrated for ABO_3 . Note the corner shared octahedra, extending in three dimensions [82].

Although majority of the perovskite compounds are oxides or fluorides, other forms like heavier halides, sulphides, hydrides, cyanides, oxyfluorides and oxynitrides are also reported [56, 57, 81]. Perovskite and perovskite-related materials are important crystal structure due to their diverse physical/chemistry properties over a wide temperature range. For example, perovskite ceramics with ferroelectric and/or piezoelectric properties, such as $BaTiO_3$ and $Pb(ZrTi)O_3$ play a dominant role in the electroceramics industry. Other industry interests of perovskites are: colossal magnetoresistance ($(SrCaLa)MnO_3$), PTC thermistor ($BaTiO_3$), electrooptical modulator ($(PbLa)(ZrTi)O_3$, $BaTiO_3$), optical switch ($LiNbO_3$), battery material ($Li_{0.5-x}La_xTiO_3$), etc. It is of interest to find out regularities governing the formation of perovskite-type compounds and use it to further guide the exploration of new materials. The structure is very versatile having many useful technological applications such as ferroelectrics, catalysts, sensors, and superconductors.

In early 1920s, Goldschmidt has proposed a “tolerance factor”

$$t = (r_A + r_O) / \sqrt{2} (r_B + r_O) \quad (2.13)$$

Where r_A , r_B and r_O are the ionic radii of A, B and O, respectively to study the stability of perovskites. Geometrically, for an ideal perovskite, the ratio of $D(A-O)$, the bond length of A–O bond, to $D(B-O)$, the bond length of B–O bond, is $\sqrt{2} : 1$. Thus, if the bond length is roughly assumed to be the sum of two ionic radii, the t value of an

ideal perovskite should be equal to 1.0. However, Goldschmidt found that, as an experimental fact, t values of most cubic perovskites are in the range of 0.8–0.9, and distorted perovskites occur in somewhere wider range of t . Goldschmidt's tolerance factor t has been widely accepted as a criterion for the formation of the perovskite structure, a number of researchers have used it to discuss the perovskite stability, including oxides, fluorides, chlorides. Up to now, almost all known perovskite compounds have t values in the range of 0.75–1.00. However, it seems that $t = 0.75$ –1.00 is not a sufficient condition for the formation of the perovskite structure, as indicated later, for some systems whose t are even within the most favourable range (0.8–0.9), no perovskite structure is stable.

2.2.2 K_2NiF_4 -typed structure

Daroukh *et al.* reported that the thermochemical stability of A_2BO_4 oxides is higher than the perovskite ABO_3 oxides and the thermal expansion of A_2BO_4 oxides is generally lower than that of the ABO_3 oxides with comparable cationic compositions [24, 25]. This implies that A_2BO_4 oxides are very likely to be the new type of cathode materials of IT-SOFCs. The phase behaviors of the ternary A_2BO_4 oxides with the K_2NiF_4 typed structure have received considerable interest in recent years, particularly since the discovery of superconductivity in $La_{2-x}Ba_xCuO_4$, $La_{2-x}Sr_xCuO_4$, La_2CuO_4 and Sr_2RuO_4 [10, 62].

The idealized, two-dimensional structure of A_2BO_4 oxides consists of perovskite-like, corner linked BO_6 sheets interleaved by rock-salt like AO layers. The large A cations are arranged in layers with nine nearest O neighbors, 4+4 from one BO_4 layer and 1 much shorter interaction from the adjacent layer of stoichiometry BO_4 , as in Figure 2.4.

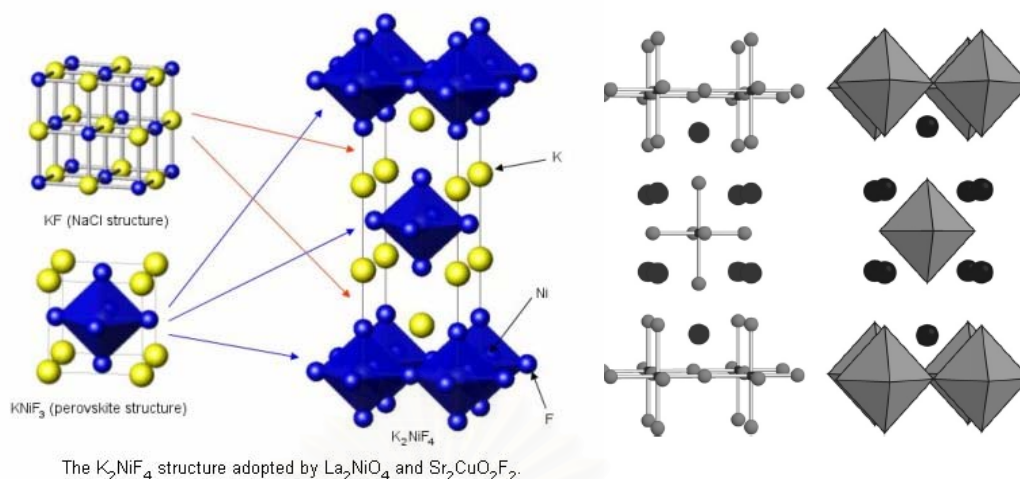


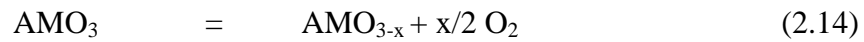
Figure 2.4 Ideal K_2NiF_4 -typed structure illustrated for A_2BO_4 showing the NiF_6 octahedra and potassium ions (black spheres) [9, 75].

The BO_6 octahedra are not perfectly regular consisting, typically, of four short in-plane B–O distances (equatorial) plus two slightly longer apical B–O interactions. As with many complex oxide structures built from BO_n polyhedra the potential exists for these units to tilt or rotate around their centers while maintaining the basic structure type. Such rotations and tilts of the BO_n polyhedra in these structures generally result in a reduction of the unit cell symmetry but also allows improved coordination to the A-type cations. Thus one important factor that determines the structure of the A_2BO_4 compounds is the matching between the perovskite-like BO_6 layers and the A-type cations. A measure of the bond length matching can be calculated from a version of the Goldsmidt tolerance factor $t = (r_A + r_O) / \sqrt{2} (r_B + r_O)$ for perovskite and perovskite derived structure types; ideal matching between the A cation and one layer of linked BO_6 octahedra occurs for $t \approx 1$ and the structure formed is tetragonal described in the space group $I4/mmm$ (no. 139) [33, 75].

The parent nicklate, $La_2NiO_{4+\delta}$, is made up of alternating $LaNiO_3$ perovskite and La_2O_2 rock salt layers. Significant excess oxygen, δ , can be incorporated into the rock-salt layer as interstitial defects [24, 36, 38].

2.2.3 Fundametal [26]

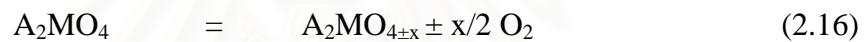
Corresponding to the thermodynamic stabilities of the oxides within the range of phase stability, the oxide AMO_3 undergoes a partial reduction/oxidation reaction resulting in the well-known oxygen vacancy and electron hole-type defect structure, which determines the electrical transport properties of the oxides.



At higher temperatures and lower oxygen partial pressures, the AMO_3 phase becomes unstable and reacts to A_2MO_4 :



Reaction (2.15) can be assumed as a proof of the higher thermochemical stability of the A_2MO_4 -type compounds compared with the AMO_3 -type oxides. A_2MO_4 -type oxides undergo partial reduction/oxidation reactions as well, corresponding to their thermodynamic stabilities within the range of existence of the phase.



The perovskite and the K_2NiF_4 -typed oxide are characterized by a range of existence expressed by the oxygen to metal stoichiometry range $(3-x)$ and $(4-x)$, respectively.

$$X = f(T, pO_2) \quad (2.17)$$

2.2.4 Thermal expansion

To minimize stresses during cell fabrication and cell operation. Thermal expansion of the cathode should be matched with other SOFC component materials, especially electrolyte and interconnect.

Thermal Expansion

Over small temperature ranges, the linear nature of thermal expansion leads to expansion relationships for length in terms of the linear expansion coefficient.

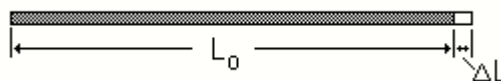


Figure 2.5 The relationship for length in terms of the linear expansion [69].

Linear Expansion

Over small temperature ranges, the fractional thermal expansion of uniform linear objects is proportional to the temperature change. The calculation is set up in the form [68]

$$L/L_0 = \alpha L_0 / \Delta T \quad (2.18)$$

Where L_0 is original length (mm).

L is length change (mm).

ΔT is original temperature – final temperature.

The thermal expansion coefficients (α) of K_2NiF_4 -typed oxides are generally lower than the thermal expansion coefficients of the perovskite typed oxides of comparable cationic compositions. The differences in thermal expansion between measurements in air and in argon environment are smaller for K_2NiF_4 -typed oxides compared with the differences for the ABO_3 oxides [26].

2.3 Reactivity of perovskite cathode with YSZ

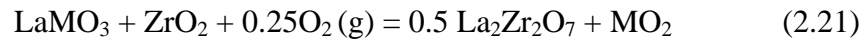
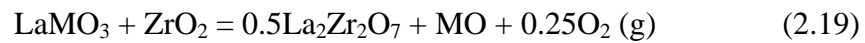
2.3.1 Thermodynamic considerations

The perovskite are lattice provskites a strong stabilization effect on the transition metal ions in B sites. For example, the trivalent Co^{3+} ions are well stabilized in the perovskite structure, although this valence state is not fully stable in other crystal structures. This stabilization is due to the geometrical matching of the A-site and the B-site ions. When the tolerance factor derived from the ionic sizes is close to unity, large stabilization energy is achieved. For the rare earth transition metal perovskites, the tolerance factor is less than unity suggesting that rare earth ions are small as A-site cations. Among rare earth ions, the largest ions, La^{3+} , therefore exhibit the largest stabilization. When comparison is made between Ca and Sr, the stabilization energy of SrO-based perovskites is generally larger because of better geometrical fitting.

Yttria-stabilized zirconia also exhibits strong stabilization on forming solid solutions in the fluorite structure. Pure zirconia has the stable monoclinic phase in which the zirconia ions are coordinated with 7 oxide ions, whereas the cubic phases with 8 coordinates becomes stable only at high temperature. On doping with Y_2O_3 , the oxide ion vacancies are formed preferentially around the zirconium ion, which leads to stabilization of zirconia in the cubic phases. Perovskite cathodes and 8-YSZ electrolyte can react in several ways as discussed below [4].

2.3.2 Reaction of perovskites with the zirconia component in YSZ

The La_2O_3 component in perovskite can react with the zirconia component in YSZ to form lanthanum zirconia, $\text{La}_2\text{Zr}_2\text{O}_7$.



Where M is the transition metal and MO_n is its binary oxide. During cell fabrication at high temperatures, reaction becomes important because of its large entropy change. During cell operation, oxygen potential dependence becomes important. Since YSZ is an oxide ion conductor, the oxygen potential in the vicinity of the electrode/electrolyte interface is important in determining how electrolyte/electrode chemical reactions proceed under cell operation [4].

2.4 The synthesis of perovskite and K_2NiF_4 -typed structure synthesis

The procedure for preparing perovskite and K_2NiF_4 -typed membranes consists of three steps: powder synthesis, shaping and sintering. Powder synthesis, as the first step, plays a critical role in determining the particle size of the powder, and consequently has an influence on the microstructure of the membrane. There are many routes to synthesize powders, such as a conventional solid-state reaction method and a wet chemical process that includes thermal decomposition of cyanide, metal-EDTA, chemical co-precipitation and the sol-gel process.

2.4.1 Solid-state reaction

The solid state reaction is very convenient but the impurities are introduced from raw materials, milling media, and the calcinations container. Because of the high temperature required for the complete reactions between metal-carbonates, hydroxides, and oxides. LSCF represents a typical case, Raw materials La_2O_3 , SrCO_3 , CoO_3 , and Fe_2O_3 were mixed and ball-milled. After drying, then the mixed powders were calcined at $1,000^\circ\text{C}$ to remove impurities and to achieve single-phase powder.

2.4.2 Solution reaction

A convenient way of classifying the methods, which state from solution, is to consider the means used for solvent removal. Two basic classes exist. The first is based upon precipitation with subsequent filtration, centrifugation, etc.,

used to separate the solid and liquid phases. The second basic method depends upon thermal processes, e.g., evaporation, sublimation, combustion, etc., to remove the solvent. The latter method is preferred because of the possible contemporaneous conversion of the residue into the desired product.

The solution reaction method is potentially advantageous in comparison with other methods for achieving homogeneous mixing at lower processing temperature, better control the stoichiometry and purity, easily generated porous its and enhanced ability to control particle size.

2.5 Powder sizing

A single particle size does not produce good packing. Optimum packing for particles with all the same size results in over 30% void space. Adding particles of a size equivalent to the largest voids reduces the void pore volume to 23 %. Therefore, to achieve maximum particle packing, a range of particle sizes is required. Powder particles are influenced on compacting and sintering. The objective of the pressing step is to achieve maximum particle packing and uniformity.

The primary driving force for densification of a compacted powder at high temperature is the change in surface free energy. Very small particles have high surface areas. The high surface free energy and very strong thermodynamic drive force decrease their surface by bonding them together. The particle with approximate sizes of 1 μm or less can be compacted into a porous shape and sintered at a high temperature to near theoretical density. Typically, the finer the powder, the greater its surface area, and the lower the temperature and shorter time for densification. Long times of the sintering temperature was a result of the increasing in grain growth which causes lower strength.

2.5.1 Powder compacting by uniaxial pressing

Uniaxial pressing involves the compaction of powder into a rigid die by applying pressure in a single axial direction through a rigid punch or piston. The presses are usually mechanical or hydraulic. Pressing results in the direct contact of particles, reduces the average distance between particles, and changes the shape of particles. The apparent density of a compact was controlled by mixing of the proper various particles size fractions. To enhance the compacting, before pressing, the powder should be disaggregated by mixing the powder with solvent such as

isopropanol in the ultrasonic bath or added a couple drops of acetone to reduce the surface tension.

2.5.2 Sintering

Sintering is a process of permanent chemical and physical change by the decreasing of porosity by the grain growth high temperature. When an aggregated powder is sintered, necks of inter agglomerate are formed between the particles, and the density of aggregate is increased. The growth of the neck is increased with the transport of matter or the counter-flow of vacancies between the particles and the pored. The sintering can be classified into three stages.

In the first stage which the necks form at points of particle contact and the particles usually approach each other at the center. At this stage the individual particles are still distinguishable. The second stage is that the necks become large, resulting in the formation of an interconnected pore structure. The third or the final stages, the pores become isolated. The interconnectivity of pores eliminates surface and vapor transport.

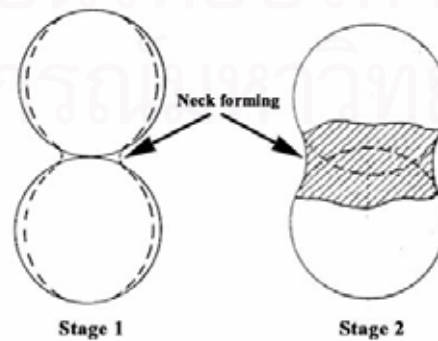
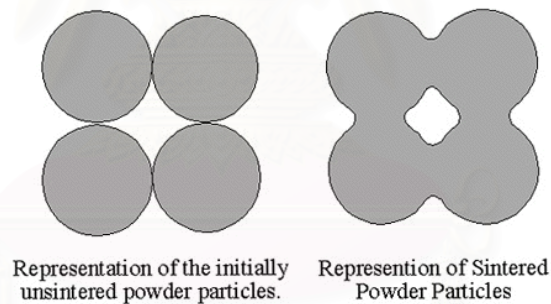


Figure 2.6 Mechanism of sintering [77].

2.6 Screen printing

The screen-printing technique is one of the most important methods to fabricate cathode film. Process parameters may affect the electrochemical active area, the electronic conductivity of the electrodes and the gas diffusion for the reactants. The binders used in preparing the screen-printed cathode films are often the ethyl cellulose, polyvinyl–butyral, terpineol and polyvinyl alcohol [63, 67, 74].

2.7 Crystal structure

2.7.1 Lattice and unit cell

Solid is composed of an array of atoms/ions/molecules. If the arrays of atoms/ions/molecules are arranged in a particular ordered pattern, that solid is referred as “crystalline”. If the arrays of atoms/ions/molecules are arranged in non-uniform pattern, solid is referred as “amorphous”. Position of atoms/ions/molecules in the array is referred to as “Lattice point”.

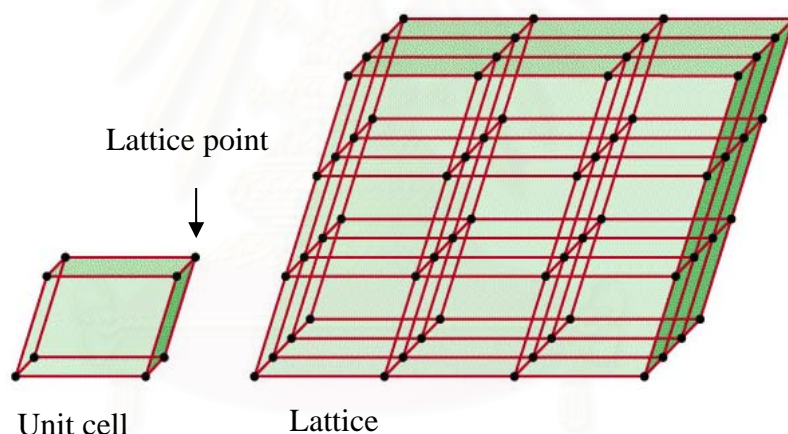


Figure 2.7 Unit cell and lattice [61].

The unit cell is the basic building block of a crystal, repeated infinitely in three dimensions. It is characterized by three vectors (a , b , c) that form the edges of a parallelepiped cell, and the angles between these vectors: α (alpha), the angle between b and c ; β (beta) the angle between a and c ; γ (gamma), the angle between a and b .

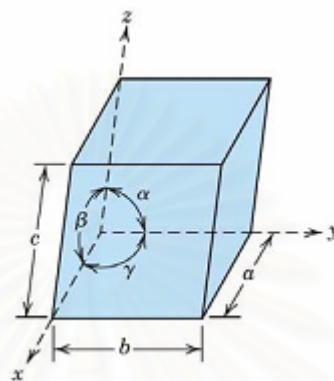
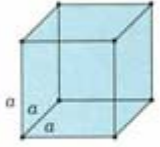
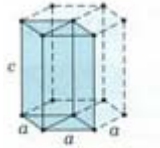
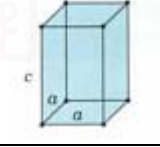

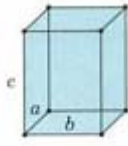
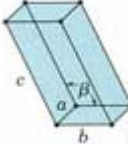
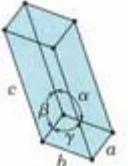


Figure 2.8 A unit cell with x , y and z coordinate axes, showing the lattice parameters: axial lengths (a , b and c) and interaxial angles (α , β and γ) [61].

2.7.2 Crystal systems and Bravais Lattices

Table 2.1 The seven types of unit cells [61]

Crystal System	Axial Relationships	Interaxial Angles	Unit Cell Geometry
Cubic	$a = b = c$	$\alpha = \beta = \gamma = 90^\circ$	
Hexagonal	$a = b \neq c$	$\alpha = \beta = 90^\circ, \gamma = 120^\circ$	
Tetragonal	$a = b \neq c$	$\alpha = \beta = \gamma = 90^\circ$	
Rhombohedral	$a = b = c$	$\alpha = \beta = \gamma \neq 90^\circ$	

Orthorhombic	$a \neq b \neq c$	$\alpha = \beta = \gamma = 90^\circ$	
Monoclinic	$a \neq b \neq c$	$\alpha = \gamma, \beta \neq 90^\circ$	
Triclinic	$a \neq b \neq c$	$\alpha \neq \beta \neq \gamma \neq 90^\circ$	

2.7.3 Miller Indices

To determine the Miller Indices (hkl) of a plane, the following steps must be taken.

1. Choose an atom as the origin of the coordinate system and three crystallographic directions.
2. Determine the intercepts of the plane along each of the three crystallographic directions.
3. Take the reciprocals of the intercepts to obtain the values for hkl .
4. If this results in fractions, then multiply each value by the denominator of the smallest fraction.

สถาบันวิทยบริการ
จุฬาลงกรณ์มหาวิทยาลัย

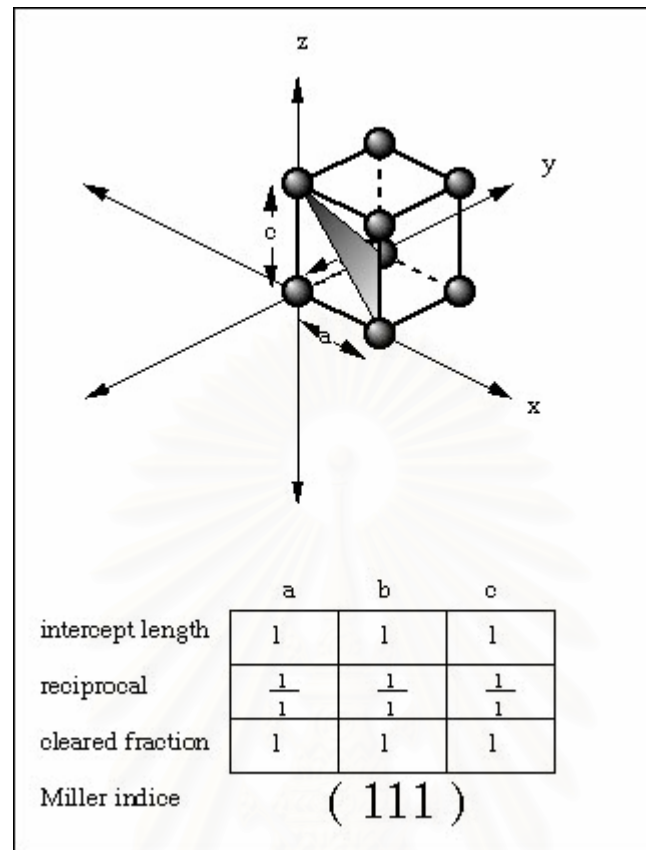


Figure 2.9 An example of miller indices: (111).

2.8 Characterization of materials

2.8.1 X-ray Diffraction (XRD)

Powder X-Ray Diffraction (XRD) is a versatile and non-destructive technique that reveals a detailed information about the chemical composition and crystallographic structure of natural and manufactured solid materials. It is an efficient analytical technique used to identify and characterize unknown crystalline materials. Monochromatic x-rays are used to determine the interplanar spacings of the unknown materials. Samples are analyzed as powders with grains in random orientations to ensure that all crystallographic directions are sampled by the beam. When the Bragg condition for constructive interference is obtained, a reflection is produced, and the relative peak height is generally proportional to the number of grains in a preferred orientation.

The main components of XRD instrument are an X-ray source, a specimen holder and a detector.

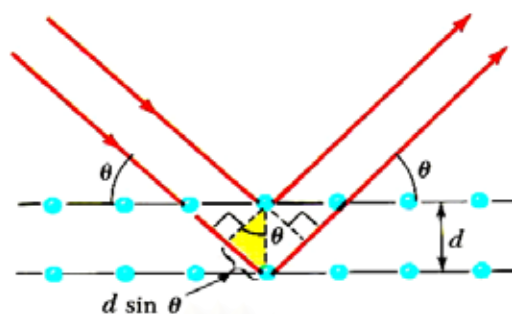


Figure 2.10 Diffraction of X-rays by a crystal [77].

Figure 2.10 shows a monochromatic beam of X-ray incident on the surface of atomic arrays at angle θ . The scattered intensity can be measured as a function of a scattering angle, 2θ . The interaction of X-rays with a sample creates secondary “diffracted” beams (actually generated in the form of cones) of X-rays related to interplanar spacings in the crystalline powder according to a mathematical relation called “Bragg’s Law”.

$$n\lambda = 2d \sin\theta \quad (2.22)$$

Where n is an integer, λ is the wavelength of the X-rays, d is the interplanar spacing generating the diffraction, and θ is the diffraction angle. λ and d are measured in the same units, usually angstroms.

The diffraction pattern, comprised of positions (2θ angle) and intensities of the diffracted beam, is obtained by varying the incidence angle. Positions and intensities of the diffracted peaks act as a distinctive “fingerprint” which provides several information about the sample. Identification of crystalline compounds can be obtained by comparing the acquired pattern with the Joint Committee on Powder Diffraction Standards (JCPDS) database.

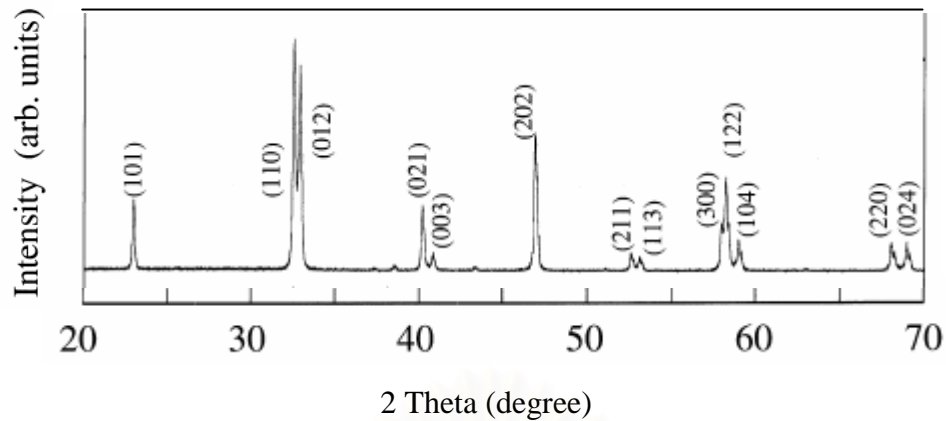


Figure 2.11 XRD pattern of LaNi_{0.6}Fe_{0.4}O₃ (perovskite structure) from JCPDS:33-0711 database.

Relationship between d-value and the lattice constants

$$\lambda = 2d \sin\theta \quad \text{“Bragg’s Law”}$$

The wavelength (λ) is known and Theta (θ) is the half value of the peak position ; therefore, can be calculated

For an orthorhombic

$$\text{From} \quad 1/d^2 = \frac{h^2}{a^2} + \frac{k^2}{b^2} + \frac{l^2}{c^2}$$

- h, k and l are the miller indices of the peaks.
- a, b and c are lattice parameter of the elementary cell.
- If a, b and c are known it is possible to calculate the peak position.
- If the peak position is known it is possible to calculate the lattice parameter.

CHAPTER III

EXPERIMENTAL

In this thesis, the perovskite and K_2NiF_4 -typed lanthanum nickel iron oxides were synthesized by the combustion method. Furthermore, their chemical and physical compatibilities with 8-YSZ, the commercial electrolytic material for SOFC, were also investigated.

3.1 Chemicals:

The Chemicals listed in Table 3.1, were used without further purification.

Table 3.1 Chemicals and reagents

Reagents	Formula weight	Purity (%)	Company
Citric acid	192.43	99.5-100.5	Fluka
$Fe(NO)_3 \cdot 9HO$	404.00	98	Ajax
HNO_3	63.01	65	Merck
$La(NO)_3 \cdot 6HO$	433.02	99.0	Fluka
$NH_4 OH$	35.05	25	Merck
$Ni(NO)_3 \cdot 6HO$	290.81	97-	Unilab
8 mol % ZrO_2 / Y_2O_3	123.22	99.9	Aldrich

3.2 Synthesis of perovskite and K_2NiF_4 -typed powders

The powders of perovskite and K_2NiF_4 -typed structures were prepared by four combustion synthesis routes: (a) water citrate, (b) modified water citrate, (c) nitric citrate, and (d) modified nitric citrate.

3.2.1 Synthesis of perovskite and K_2NiF_4 powders by water citrate method (WC)

The perovskite $LaNi_{1-x}Fe_xO_3$ ($x = 0-1.0$) and the K_2NiF_4 -typed $La_2Ni_{1-x}Fe_xO_4$ ($x = 0-1.0$) were synthesized. The stoichiometric amounts of $La(NO)_3 \cdot 6H_2O$, $Ni(NO)_2 \cdot 6H_2O$ and $Fe(NO)_3 \cdot 9H_2O$ were dissolved in water. The citric acid was added with a citric acid-to-nitrate mole ratio of 2:1 for perovskite powders, and of 1:1 for K_2NiF_4 -typed powders. The pH of the solution was $\approx 0-1$. The mixture solution was stirred on a hot plate for 3-5 h.

The combustion of the homogeneous mixture solution was carried out on a hot plate around 200-300 °C in a three-liter beaker covered with a fine sieve to prevent the loss of fine powder during combustion. The water was evaporated until a sticky gel was obtained. Then it became a large swelling viscous mass. The combustion lasted for about 10-20 seconds. The sponge-like black solid expanded to occupy almost 2/3 of the beaker volume at the end. The obtained black powders were calcined at 700-1200 °C with the increasing rate of 2 °C/min for 5h to yield the desired LNF and L₂NF samples.

3.2.2 Synthesis of perovskite and K₂NiF₄ powders by modified water citrate method (MWC)

The perovskite LaNi_{1-x}Fe_xO₃ (x = 0-1.0) and the K₂NiF₄-typed La₂Ni_{1-x}Fe_xO₄ (x = 0-1.0) were synthesized. The stoichiometric amounts of La(NO₃)₃.6H₂O, Ni(NO)₂.6H₂O and Fe(NO)₃.9H₂O were dissolved in water. The citric acid was added with a citric acid-to-nitrate mole ratio of 2:1 for perovskite powders, and of 1:1 for K₂NiF₄-typed powders. The mixture solution was added slowly with aq.NH₃ at the controlled rate of 2-3 ml/min. The pH of the solution was adjusted to ≈ 9-10. The mixture solution was stirred on a hot plate for 3-5 h. The combustion method was the same as WC method.

3.2.3 Synthesis of perovskite and K₂NiF₄ powders by nitric citrate method (NC)

The perovskite LaNi_{1-x}Fe_xO₃ (x = 0-1.0) and the K₂NiF₄-typed La₂Ni_{1-x}Fe_xO₄ (x = 0-1.0) were synthesized. The stoichiometric amounts of La(NO₃)₃.6H₂O, Ni(NO)₂.6H₂O and Fe(NO)₃.9H₂O were dissolved in HNO₃ and H₂O. The citric acid was added with a citric acid-to-nitrate mole ratio of 2:1 for perovskite powders, and of 1:1 for K₂NiF₄-typed powders. The pH of the solution was ≈ 0-1. The mixture solution was stirred on a hot plate for 3-5 h. The combustion method was the same as WC method.

3.2.4 Synthesis of perovskite and K_2NiF_4 powders by modified nitric citrate method (MNC)

The perovskite $LaNi_{1-x}Fe_xO_3$ ($x = 0-1.0$) and the K_2NiF_4 -typed $La_2Ni_{1-x}Fe_xO_4$ ($x = 0-1.0$) were synthesized. The stoichiometric amounts of $La(NO_3)_3 \cdot 6H_2O$, $Ni(NO)_2 \cdot 6H_2O$ and $Fe(NO)_3 \cdot 9H_2O$ were dissolved in HNO_3 and H_2O . The citric acid was added with a citric acid-to-nitrate mole ratio of 2:1 for perovskite powders, and of 1:1 for K_2NiF_4 -typed powders. The mixture solution was added slowly with aq. NH_3 at the controlled rate of 2-3 ml/min. The pH of the solution was adjusted to $\approx 9-10$. The mixture solution was stirred on a hot plate for 3-5 h. The combustion method was the same as WC method.



Table 3.2 A list of the experimental conditions and results for the synthesis of perovskite compounds by water citrate method

Materials	Code	Color	pH	Spontaneous combustion time (min) and material appearance	The calcination temperature (°C)
$\text{LaNi}_0\text{Fe}_{1.0}\text{O}_3$	LNF-01	Yellow bright	0.86	18 / yellow powder	700 900
$\text{LaNi}_{0.1}\text{Fe}_{0.9}\text{O}_3$	LNF-19	Yellow bright	0.67	20 / black powder	700 900
$\text{LaNi}_{0.2}\text{Fe}_{0.6}\text{O}_3$	LNF-28	Yellow brown	0.50	24 / black powder	700 900
$\text{LaNi}_{0.3}\text{Fe}_{0.7}\text{O}_3$	LNF-37	Yellow brown	0.56	51 / black powder	700 900
$\text{LaNi}_{0.4}\text{Fe}_{0.6}\text{O}_3$	LNF-46	Yellow brown	0.72	12 / black powder	700 900
$\text{LaNi}_{0.5}\text{Fe}_{0.5}\text{O}_3$	LNF-55	Yellow brown	0.75	38 / black powder	700 900
$\text{LaNi}_{0.6}\text{Fe}_{0.4}\text{O}_3$	LNF-64	Yellow brown	0.75	44 / black powder	700 900
$\text{LaNi}_{0.7}\text{Fe}_{0.3}\text{O}_3$	LNF-73	Yellow green	0.80	50 / black powder	700 900
$\text{LaNi}_{0.8}\text{Fe}_{0.2}\text{O}_3$	LNF-82	Green bright	0.63	40 / black powder	700 900
$\text{LaNi}_{0.9}\text{Fe}_{0.1}\text{O}_3$	LNF-91	Green bright	0.59	30 / black powder	700 900
$\text{LaNi}_{1.0}\text{Fe}_0\text{O}_3$	LNF-10	Green bright	0.87	21 / dark brown powder	700 900

Table 3.3 A list of the experimental conditions and results for the synthesis of perovskite compounds by modified water citrate method

Materials	Code	Color and appearance changing during titration	pH	Spontaneous combustion time (min) and material appearance	The calcination temperature (°C)
$\text{LaNi}_0\text{Fe}_{1.0}\text{O}_3$	LNF-01	Yellow bright to yellow green to dark yellow green to yellow bright	9.47	44 / yellow powder	700 900
$\text{LaNi}_{0.1}\text{Fe}_{0.9}\text{O}_3$	LNF-19	Yellow bright to yellow green to dark green	9.29	44 / black powder	700 900
$\text{LaNi}_{0.2}\text{Fe}_{0.6}\text{O}_3$	LNF-28	Yellow brown to yellow green to dark green	9.44	33 / black powder	700 900
$\text{LaNi}_{0.3}\text{Fe}_{0.7}\text{O}_3$	LNF-37	Yellow brown to dark yellow to green to dark green	9.57	33 / black powder	700 900
$\text{LaNi}_{0.4}\text{Fe}_{0.6}\text{O}_3$	LNF-46	Yellow brown to dark yellow to green to dark green	9.57	45 / black powder	700 900
$\text{LaNi}_{0.5}\text{Fe}_{0.5}\text{O}_3$	LNF-55	Yellow brown to dark yellow to green to dark green	9.59	39 / black powder	700 900
$\text{LaNi}_{0.6}\text{Fe}_{0.4}\text{O}_3$	LNF-64	Yellow brown to yellow green to green to dark green	9.46	29 / black powder	700 900
$\text{LaNi}_{0.7}\text{Fe}_{0.3}\text{O}_3$	LNF-73	Yellow green bright to green bright to dark green	9.57	30 / black powder	700 900
$\text{LaNi}_{0.8}\text{Fe}_{0.2}\text{O}_3$	LNF-82	Green bright to green to dark green to dark blue	9.54	36 / black powder	700 900
$\text{LaNi}_{0.9}\text{Fe}_{0.1}\text{O}_3$	LNF-91	Green bright to green to dark green to dark blue	9.36	25 / black powder	700 900
$\text{LaNi}_{1.0}\text{Fe}_0\text{O}_3$	LNF-10	Green bright to green to dark green to dark blue	9.12	28 / dark brown powder	700 900

Table 3.4 A list of the experimental conditions and results for the synthesis of K_2NiF_4 compounds by water citrate method

Materials	Code	Color	pH	Spontaneous combustion time (min) and material appearance	The calcination temperature ($^{\circ}C$)
$La_2Ni_0Fe_{1.0}O_3$	LNF-01	Yellow brown red	0.43	31 / yellow powder	700 900
$La_2Ni_{0.1}Fe_{0.9}O_3$	LNF-19	Yellow brown red	0.36	30 / black powder	700 900
$La_2Ni_{0.2}Fe_{0.6}O_3$	LNF-28	Yellow brown red	0.39	20 / black powder	700 900
$La_2Ni_{0.3}Fe_{0.7}O_3$	LNF-37	Yellow brown red	0.32	24 / black powder	700 900
$La_2Ni_{0.4}Fe_{0.6}O_3$	LNF-46	Yellow brown red	0.86	15 / black powder	700 900
$La_2Ni_{0.5}Fe_{0.5}O_3$	LNF-55	Yellow brown red	0.39	25 / black powder	700 900
$La_2Ni_{0.6}Fe_{0.4}O_3$	LNF-64	Yellow brown red	0.42	25 / black powder	700 900
$La_2Ni_{0.7}Fe_{0.3}O_3$	LNF-73	Yellow brown red	0.42	23 / black powder	700 900
$La_2Ni_{0.8}Fe_{0.2}O_3$	LNF-82	Green yellow	0.41	35 / black powder	700 900
$La_2Ni_{0.9}Fe_{0.1}O_3$	LNF-91	Green yellow	0.43	23 / black powder	700 900
$La_2Ni_{1.0}Fe_{0.0}O_3$	LNF-10	Green	0.44	30 / dark brown powder	700 900

Table 3.5 A list of the experimental conditions and results for the synthesis of K_2NiF_4 compounds by modified water citrate method

Materials	Code	Color and appearance changing during titration	pH	Spontaneous combustion time (min) and material appearance	The calcination temperature ($^{\circ}C$)
$La_2Ni_0Fe_{1.0}O_3$	LNF-01	Yellow brown red to yellow to green to yellow bright	9.33	35 / yellow powder	700 900
$La_2Ni_{0.1}Fe_{0.9}O_3$	LNF-19	Yellow brown red to yellow to green bright	9.02	30 / black powder	700 900
$La_2Ni_{0.2}Fe_{0.6}O_3$	LNF-28	Yellow brown red to yellow to green bright	9.27	55 / black powder	700 900
$La_2Ni_{0.3}Fe_{0.7}O_3$	LNF-37	Yellow brown red to yellow to green dark green	9.48	40 / black powder	700 900
$La_2Ni_{0.4}Fe_{0.6}O_3$	LNF-46	Yellow brown red to yellow to green dark green	9.04	25 / black powder	700 900
$La_2Ni_{0.5}Fe_{0.5}O_3$	LNF-55	Yellow brown red to yellow green to green to dark green	9.09	41 / black powder	700 900
$La_2Ni_{0.6}Fe_{0.4}O_3$	LNF-64	Yellow brown red to yellow green to green to dark green	9.07	40 / black powder	700 900
$La_2Ni_{0.7}Fe_{0.3}O_3$	LNF-73	Yellow brown red to yellow green to green to dark green	8.98	60 / black powder	700 900
$La_2Ni_{0.8}Fe_{0.2}O_3$	LNF-82	Green yellow to green to dark green	9.35	50 / black powder	700 900
$La_2Ni_{0.9}Fe_{0.1}O_3$	LNF-91	Green yellow to green to dark green blue	9.08	40 / black powder	700 900
$La_2Ni_{1.0}Fe_0O_3$	LNF-10	Green to green blue to dark blue	9.24	34 / dark brown powder	700 900

3.3 Chemical compatibility

The investigation of chemical compatibility between LNF or L₂NF and 8-YSZ was done by two approaches, the reaction of the powder mixtures and the reaction at the interface of their membranes.

3.3.1 The mixtures of LNF and L₂NF powders with 8-YSZ

LNF/L₂NF was mixed with 8-YSZ in a 50/50 wt. % ratio. The resulting mixture was then pressed into disks before heated from 800-1200°C with 1000 °C intervals for 5 h. Heated samples were analyzed by XRD for phase identification.

3.3.2 The membrane of LNF and L₂NF powder with 8-YSZ by screen-printing technique

The electrolyte pellet was made by uniaxially pressing 3 g of 8-YSZ and sintering at 1500°C for 2 h in air. The selected LNF/ L₂NF sample was calcined at 1000°C and dispersed in butyl acetate as an organic binder to obtain a paste. The paste was applied on 8-YSZ pellet by screen printing and firing at 1000°C for 2 h in air. The compatibility of LNF64 coated on 8YSZ pellet was characterized by SEM/EDX with a point & ID mode.

3.4 Physical compatibility

The physical compatibility between LNF/L₂NF and 8-YSZ was investigated in term of the thermal expansion coefficient (TEC). The selected LNF/L₂NF sample, after calcined at 1000 °C, was made into a sample bar by the uniaxially pressing of 7 g sample, then the bar was sintered at 1200 °C for 2h in air. The thermal expansion behavior was using Unitherm Model 1161. The thermal study started from room temperature up to 1200 °C at a heating rate of 3 °C/min.

3.5 Characterization of materials

3.5.1 Powder X-ray diffraction (XRD)

The XRD patterns of LNF and L₂NF samples were obtained by a Rigaku, Dmax 2200/Ultima⁺ diffractometer, equipped with a monochromator and Cu K α radiation. The tube voltage and current were set at 40 kV and 30 mA,

respectively. The diffraction pattern was recorded in the 2-theta ranged from 20 to 70 degree (step time 0.5 s., scan step 0.020 degree).

3.5.2 Scanning electron microscopy (SEM)

The morphology and size of LNF and L₂NF particles were identified by a JSM-5800 LV scanning electron microscopy, Oxford Instrument (link ISIS series 300) at the Scientific and Technological Research Equipment center (STREC), Chulalongkorn University. Specimens were sputtering coated with gold to reduce charge effects.

As a conjunction with SEM micrographs, EDX analysis with the line-scan and ID-point modes was used to determine the elements in cross-sectioned membranes.

3.5.3 Particle size analysis

Particle size distribution of LNF and L₂NF powders was obtained by Master Sizer-S. (Malvern Instrument, England), based on laser diffraction. In order to prepare the sample, 0.2-1 g LNF/L₂NF was dispersed in the 20 ml solution of sodium pyrophosphate in DI water, and then sonicated for 4 min.

CHAPTER IV

RESULTS AND DISCUSSION

In this thesis, the preparation of single-phased perovskite and K_2NiF_4 -typed materials were studied. Furthermore, their compatibility with 8-YSZ, the commercial electrolytic material for SOFC, was also investigated. Four combustion methods, the water citrate (WC), the modified water citrate (MWC), the nitric citrate (NC) and the modified nitric citrate (MNC), were employed in the preparation of these materials. The products of different synthesis methods were compared in terms of structure and morphology. The selected samples were further investigated for chemical and physical compatibilities with 8-YSZ at elevated temperatures.

4.1 Perovskite powders

The goal was to prepare the single-phased of $LaNi_{1-x}Fe_xO_3$ perovskites for the whole series of $x = 0.0-1.0$.

4.1.1 Crystal structure

A. Crystal structure of $LaNi_{1-x}Fe_xO_3$ by the WC method at 700°C

The XRD patterns of the $LaNi_{1-x}Fe_xO_3$ ($x = 0.0-1.0$) are shown in Figure 4.1. These samples were synthesized by WC method and calcined at 700°C for 5h. As x is 0.0-0.5, the crystal structure is cubic, which is similar to that of $LaNiO_3$ (JCPDS: 33-0710, simulated in Figure 4.2a). As x is 0.6-1.0, the crystal structure is orthorhombic, similar to that of $LaFeO_3$ (JCPDS: 37-1493, simulated in Figure 4.2b). All prepared perovskites in this series were found to be single-phased.

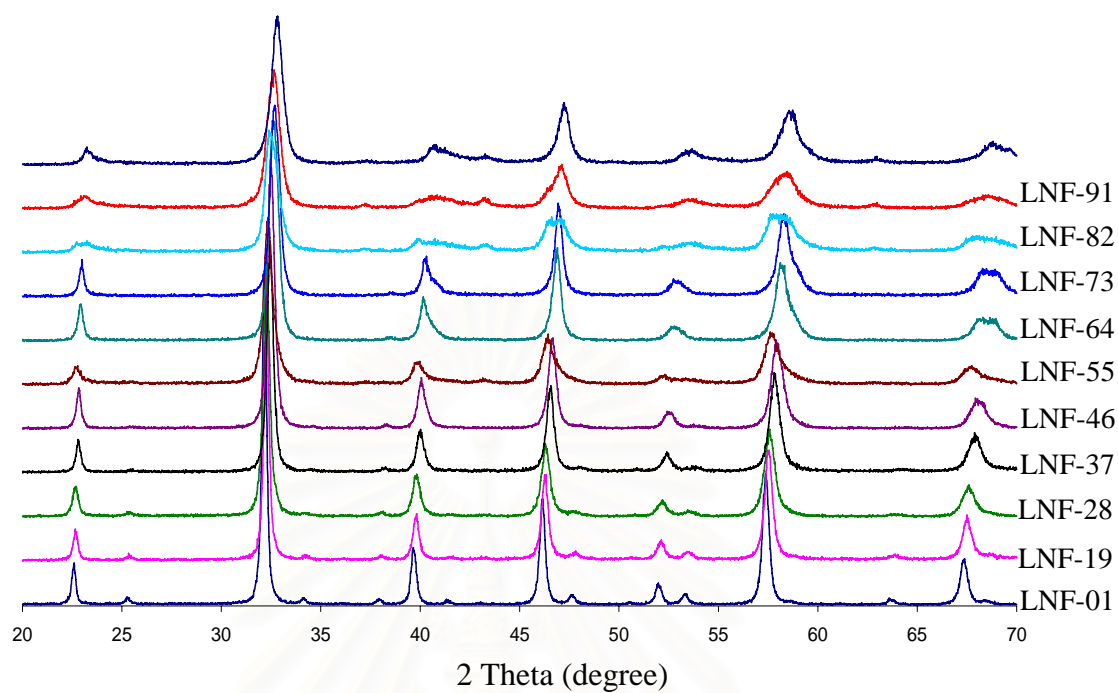


Figure 4.1 XRD patterns of $\text{LaNi}_{1-x}\text{Fe}_x\text{O}_3$ ($x = 0.0-1.0$) perovskites, synthesized by WC method and calcined at 700°C for 5h.

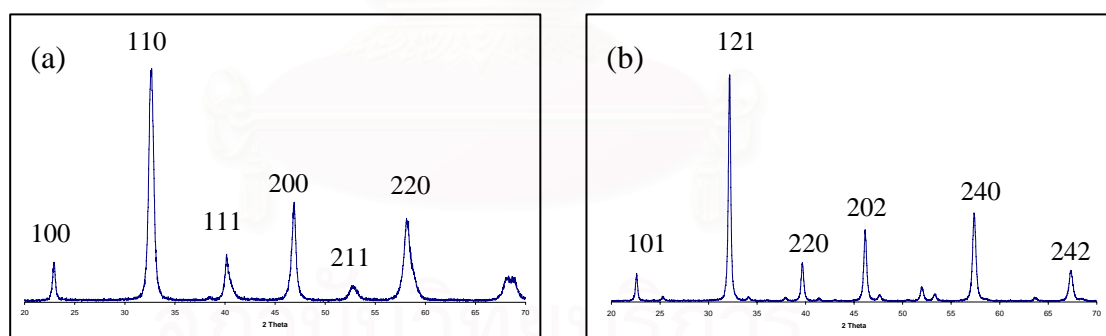


Figure 4.2 Simulated XRD patterns of (a) LaNiO_3 from JCPDS: 33-0710
(b) LaFeO_3 from JCPDS: 37-1493.

Table 4.1 Crystal structures and lattice parameters of $\text{LaNi}_{1-x}\text{Fe}_x\text{O}_3$ ($x = 0.0-1.0$) perovskites, synthesized by WC method and calcined at 700°C for 5h

Perovskite type	Crystal structure	Lattice parameters (\AA)		
		a	b	c
LaFeO_3	Orthorhombic	5.5669	7.8547	5.5530
LaNiO_3	Cubic	3.8610	3.8610	3.8610
x	Crystal structure	Lattice parameters (\AA)		
		a	b	c
1.0	Orthorhombic	5.5645	7.8586	5.5542
0.9	Orthorhombic	5.5468	7.8289	5.5406
0.8	Orthorhombic	5.5387	7.8384	5.5418
0.7	Orthorhombic	5.5332	7.8105	5.5238
0.6	Orthorhombic	5.5136	7.8053	5.5080
0.5	Cubic	3.8950	3.8950	3.8950
0.4	Cubic	3.8765	3.8765	3.8765
0.3	Cubic	3.8695	3.8695	3.8695
0.2	Cubic	3.8606	3.8606	3.8606
0.1	Cubic	3.8590	3.8590	3.8590
0	Cubic	3.8490	3.8490	3.8490

To obtain the lattice parameters for each composition in Table 4.1, the 100,110,111,200,211,220 reflections were used in the case of the cubic phase, as labeled in Figure 4.2 (a), and the 101, 121, 220, 202, 240, 242 reflections were used in the case of the orthorhombic phase as labeled in Figure 4.2 (b). For both phases, the lattice constants decrease with the decrease in x of the $\text{LaNi}_{1-x}\text{Fe}_x\text{O}_3$ systems, because the radius of Fe ion is larger than that of Ni ion.

B. Crystal structure of $\text{LaNi}_{1-x}\text{Fe}_x\text{O}_3$ by the MWC method at 700°C

The XRD patterns of the $\text{LaNi}_{1-x}\text{Fe}_x\text{O}_3$ ($x = 0.0-1.0$) are shown in Figure 4.3. These samples were synthesized by MWC method and calcined at 700°C for 5h. As x is 0.0-0.5, the crystal structure is cubic, which is similar to that of LaNiO_3 (JCPDS: 33-0710, simulated in Figure 4.2a). As x is 0.6-1.0, the crystal structure is orthorhombic, similar to that of LaFeO_3 (JCPDS: 37-1493, simulated in Figure 4.2b). All prepared perovskites in this series were found to be single-phased.

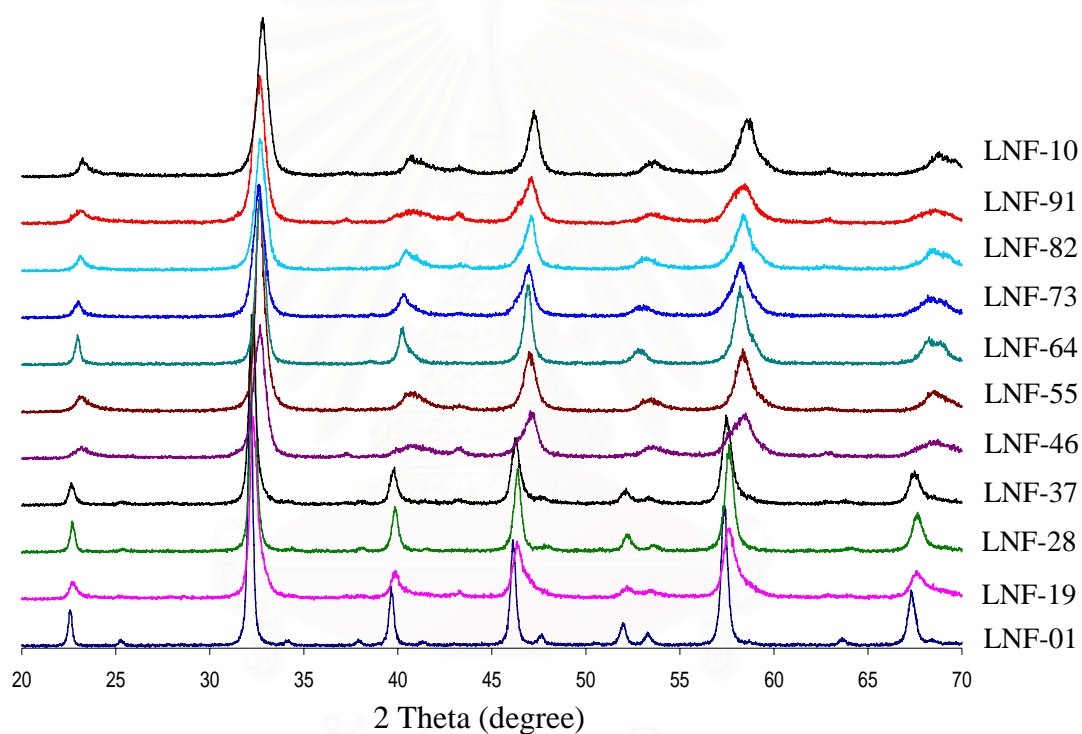


Figure 4.3 XRD patterns of $\text{LaNi}_{1-x}\text{Fe}_x\text{O}_3$ ($x = 0.0-1.0$) perovskites, synthesized by MWC method and calcined at 700°C for 5h.

Table 4.2 Crystal structures and lattice parameters of $\text{LaNi}_{1-x}\text{Fe}_x\text{O}_3$ ($x = 0.0-1.0$) perovskites, synthesized by MWC method and calcined at $700\text{ }^\circ\text{C}$ for 5h

Perovskite type	Crystal structure	Lattice parameters (Å°)		
		a	b	c
LaFeO_3	Orthorhombic	5.5669	7.8547	5.5530
LaNiO_3	Cubic	3.8610	3.8610	3.8610
x	Crystal structure	Lattice parameters (Å°)		
		a	b	c
1.0	Orthorhombic	5.5722	7.8503	5.5636
0.9	Orthorhombic	5.5344	7.8244	5.5454
0.8	Orthorhombic	5.5475	7.8153	5.5303
0.7	Orthorhombic	5.5404	7.8120	5.5285
0.6	Orthorhombic	5.5138	7.8060	5.5090
0.5	Cubic	3.8920	3.8920	3.8920
0.4	Cubic	3.8736	3.8736	3.8736
0.3	Cubic	3.8636	3.8636	3.8636
0.2	Cubic	3.8614	3.8614	3.8614
0.1	Cubic	3.8607	3.8607	3.8607
0	Cubic	3.8497	3.8497	3.8497

To obtain the lattice parameters for each composition in Table 4.2, the 100, 110, 111, 200, 211, 220 reflections were used in the case of the cubic phase, as labeled in Figure 4.2 (a), and the 101, 121, 220, 202, 240, 242 reflections were used in the case of the orthorhombic phase as labeled in Figure 4.2 (b). For both phases, the lattice constants decrease with the decrease in x of the $\text{LaNi}_{1-x}\text{Fe}_x\text{O}_3$ systems, similar to the those synthesized by MWC methods.

C. Crystal structure of $\text{LaNi}_{1-x}\text{Fe}_x\text{O}_3$ by the WC method at 900°C

The XRD patterns of the $\text{LaNi}_{1-x}\text{Fe}_x\text{O}_3$ ($x = 0.0-1.0$) are shown in Figure 4.4. These samples were synthesized by WC method and calcined at 900°C for 5h. As x is 0.0-0.5, the crystal structure is cubic, which is similar to that of LaNiO_3 (JCPDS: 33-0711, simulated in Figure 4.5 a). As x is 0.6 - 1.0, the crystal structure is orthorhombic, similar to that of LaFeO_3 (JCPDS: 37-1493, simulated in Figure 4.5 b). All prepared perovskites in this series were found to be single-phased.

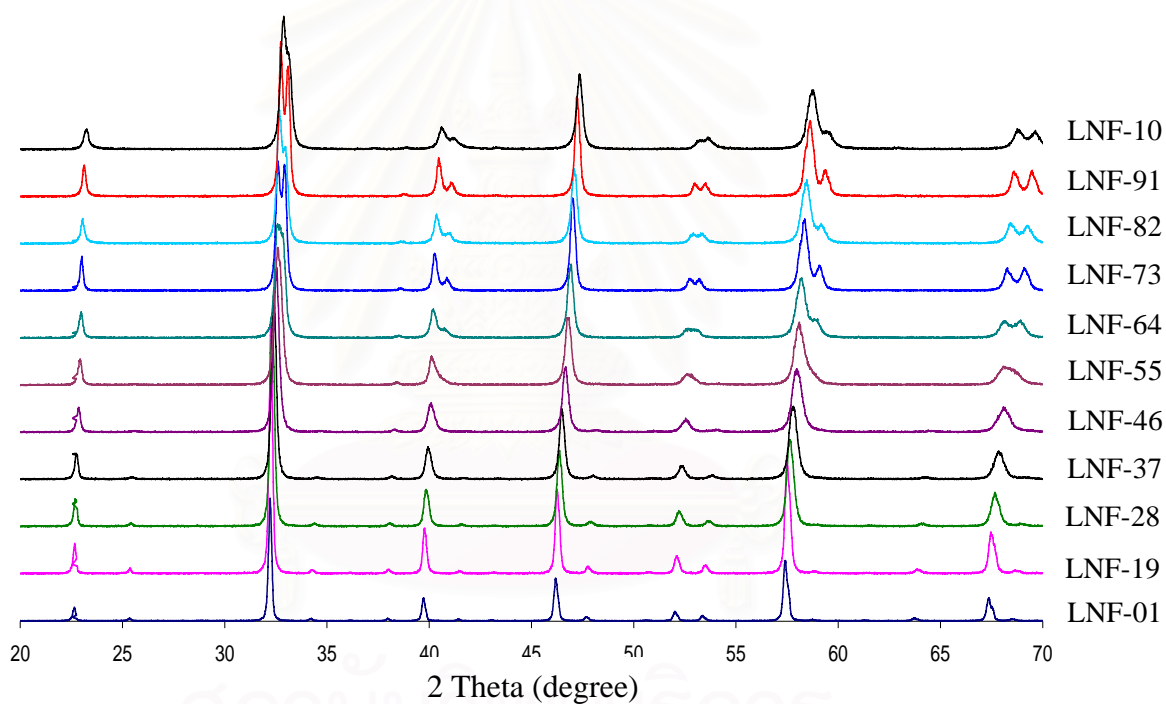


Figure 4.4 XRD patterns of $\text{LaNi}_{1-x}\text{Fe}_x\text{O}_3$ ($x = 0.0-1.0$) perovskites, synthesized by WC method and calcined at 900°C for 5h.

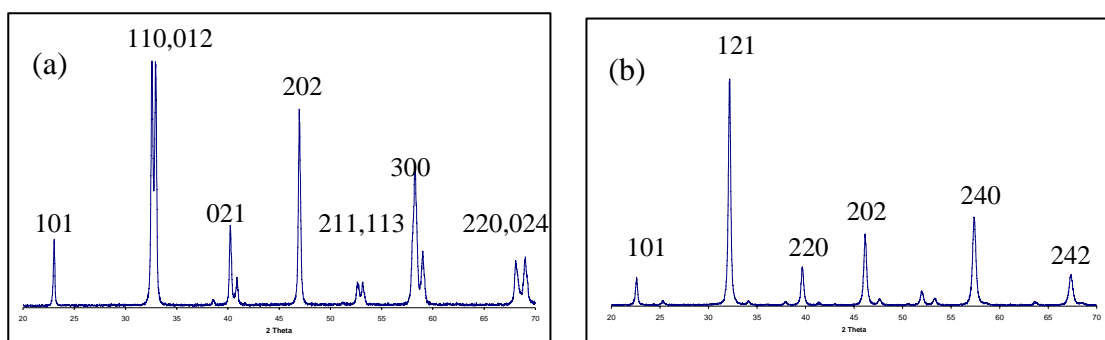


Figure 4.5 Simulated XRD patterns of (a) LaNiO_3 from JCPDS: 33-0711
(b) LaFeO_3 from JCPDS: 37-1493.

Table 4.3 Crystal structures and lattice parameters of $\text{LaNi}_{1-x}\text{Fe}_x\text{O}_3$ ($x = 0.0-1.0$) perovskites, synthesized by WC method and calcined at 900°C for 5h

Perovskite type	Crystal structure	Lattice parameters (Å°)		
		a	b	c
LaFeO_3	Orthorhombic	5.5669	7.8547	5.5530
LaNiO_3	Rhombohedral	5.4570	5.4570	6.5720
x	Crystal structure	Lattice parameters (Å°)		
		a	b	c
1.0	Orthorhombic	5.5511	7.8505	5.5477
0.9	Orthorhombic	5.5444	7.8461	5.5513
0.8	Orthorhombic	5.5320	7.8256	5.5326
0.7	Orthorhombic	5.5219	7.8102	5.5216
0.6	Orthorhombic	5.4988	7.7760	5.4991
0.5	Orthorhombic	5.4889	7.7541	5.4855
0.4	Rhombohedral	5.4921	5.4921	6.6413
0.3	Rhombohedral	5.4886	5.4886	6.6213
0.2	Rhombohedral	5.4766	5.4766	6.6112
0.1	Rhombohedral	5.4729	5.4729	6.6026
0	Rhombohedral	5.4499	5.4499	6.5420

To obtain the lattice parameters for each composition in Table 4.3, the 100, 110, 111, 200, 211, 220 reflections were used in the case of the cubic phase, as labeled in Figure 4.5 (a), and the 101, 110, 012, 021, 202, 300 reflections were used in the case of the

orthorhombic phase as labeled in Figure 4.5 (b). For both phases, the lattice constants decrease with the decrease in x of the $\text{LaNi}_{1-x}\text{Fe}_x\text{O}_3$ systems, similar to those synthesized at 900°C .

D. Crystal structure of $\text{LaNi}_{1-x}\text{Fe}_x\text{O}_3$ by the MWC method at 900°C

The XRD patterns of the $\text{LaNi}_{1-x}\text{Fe}_x\text{O}_3$ ($x = 0.0-1.0$) are shown in Figure 4.6. These samples were synthesized by MWC method and calcined at 900°C for 5h. As x is 0.0-0.5, the crystal structure is cubic, which is similar to that of LaNiO_3 (JCPDS: 33-0711, simulated in Figure 4.5 a). As x is 0.6-1.0, the crystal structure is orthorhombic, similar to that of LaFeO_3 (JCPDS: 37-1493, simulated in Figure 4.6 b). All prepared perovskites in this series were found to be single-phased.

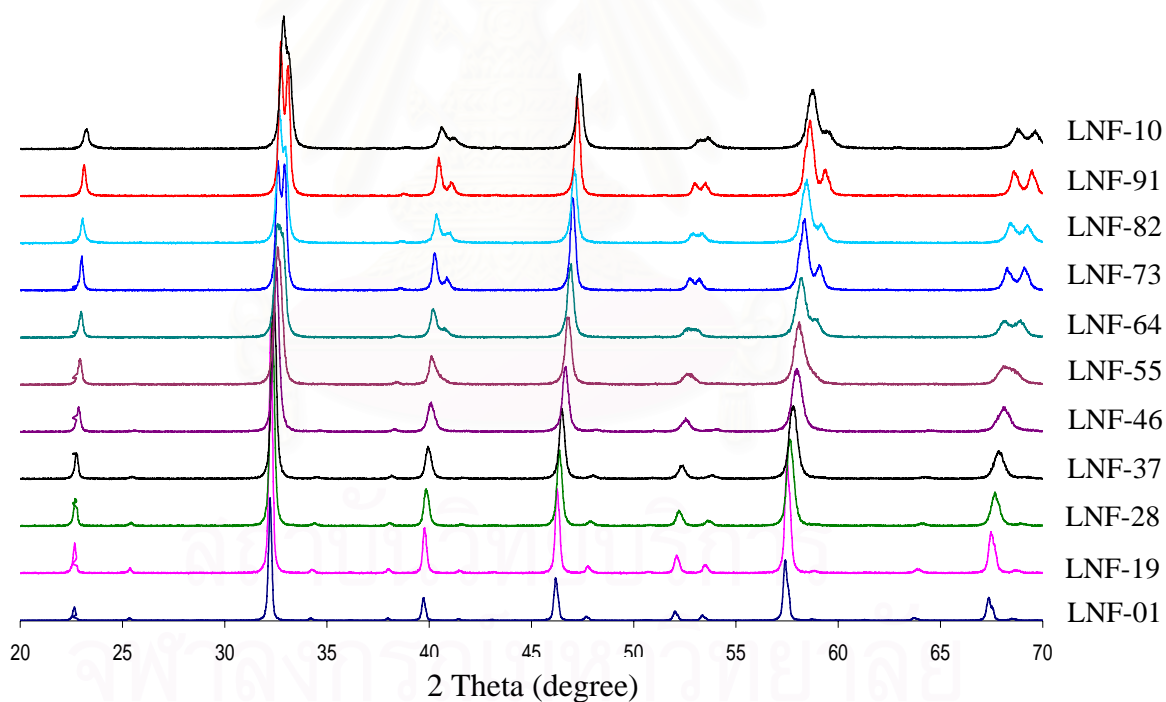


Figure 4.6 XRD patterns of $\text{LaNi}_{1-x}\text{Fe}_x\text{O}_3$ ($x = 0.0-1.0$) perovskites, synthesized by MWC method and calcined at 900°C for 5h.

Table 4.4 Crystal structures and lattice parameters of $\text{LaNi}_{1-x}\text{Fe}_x\text{O}_3$ ($x = 0.0-1.0$) perovskites, synthesized by MWC method and calcined at $900\text{ }^\circ\text{C}$ for 5h

Perovskite type	Crystal structure	Lattice parameters (Å)		
		a	b	c
LaFeO_3	Orthorhombic	5.5669	7.8547	5.5530
LaNiO_3	Rhombohedral	5.4570	5.4570	6.5720
x	Crystal structure	Lattice parameters (Å)		
		a	b	c
1.0	Orthorhombic	5.5572	7.8580	5.5467
0.9	Orthorhombic	5.5474	7.8356	5.5270
0.8	Orthorhombic	5.5352	7.8280	5.5350
0.7	Orthorhombic	5.5184	7.8035	5.5203
0.6	Orthorhombic	5.5054	7.7849	5.5043
0.5	Orthorhombic	5.4922	7.7562	5.4909
0.4	Rhombohedral	5.4897	5.4897	6.6309
0.3	Rhombohedral	5.4873	5.4873	6.6191
0.2	Rhombohedral	5.4628	5.4628	6.5953
0.1	Rhombohedral	5.4645	5.4645	6.5836
0	Rhombohedral	5.4448	5.4448	6.5743

To obtain the lattice parameters for each composition in Table 4.4, the 100, 110, 111, 200, 211, 220 reflections were used in the case of the cubic phase, as labeled in Figure 4.5 (a), and the 101, 110, 012, 021, 202, 300 reflections were used in the case of the orthorhombic phase as labeled in Figure 4.5 (b). For both phases, the lattice constants decrease with the decrease in x of the $\text{LaNi}_{1-x}\text{Fe}_x\text{O}_3$ systems, similar to those synthesized at $900\text{ }^\circ\text{C}$.

E. The volume per formula unit of $\text{LaNi}_{1-x}\text{Fe}_x\text{O}_3$ perovskites

Table 4.5 and Table 4.6 shows the volume per formula unit of $\text{LaNi}_{1-x}\text{Fe}_x\text{O}_3$ ($x = 0.0-1.0$) perovskites by WC and MWC after calcination at $700\text{ }^\circ\text{C}$ and $900\text{ }^\circ\text{C}$ for 5h. The volumes of unit cell were calculated from the unit cell

parameters from XRD patterns, and then normalized by the number of formula per unit cell.

Table 4.5 The volume of formula unit of $\text{LaNi}_{1-x}\text{Fe}_x\text{O}_3$ ($x = 0.0-1.0$) perovskites, synthesized by WC and MWC and calcined at 700°C for 5h

x	Volume of formula unit (\AA^3)	
	WC	MWC
1.0	60.72	60.84
0.9	60.15	60.03
0.8	60.14	59.94
0.7	59.68	59.82
0.6	58.25	59.28
0.5	59.09	58.95
0.4	58.25	58.12
0.3	57.93	57.67
0.2	57.53	57.57
0.1	57.46	57.54
0	57.02	57.05

Table 4.6 The volume of formula unit of $\text{LaNi}_{1-x}\text{Fe}_x\text{O}_3$ ($x = 0.0-1.0$) perovskites, synthesized by WC and MWC and calcined at 900°C for 5h

x	Volume of formula unit (\AA^3)	
	WC	MWC
1.0	60.44	60.55
0.9	60.37	60.06
0.8	59.87	59.95
0.7	59.53	59.43
0.6	59.28	58.97
0.5	58.37	58.47
0.4	57.82	57.68
0.3	57.57	57.53
0.2	57.24	56.81
0.1	57.08	56.74
0	56.09	56.24

Figure 4.7 and Figure 4.8 show the trend of the volume of formula unit of said materials as the function of Fe content (x in $\text{LaNi}_{1-x}\text{Fe}_x\text{O}_3$).

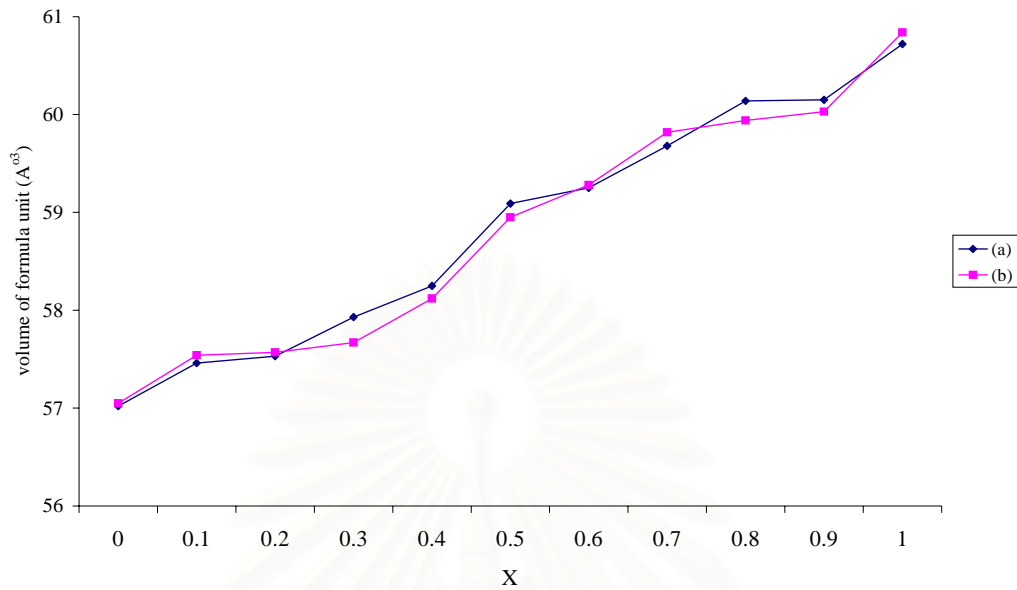


Figure 4.7 The volume of formula unit of $\text{LaNi}_{1-x}\text{Fe}_x\text{O}_3$ ($x = 0.0-1.0$) perovskite, synthesized by (a) WC (b) MWC, and calcined at $700\text{ }^\circ\text{C}$ for 5h.

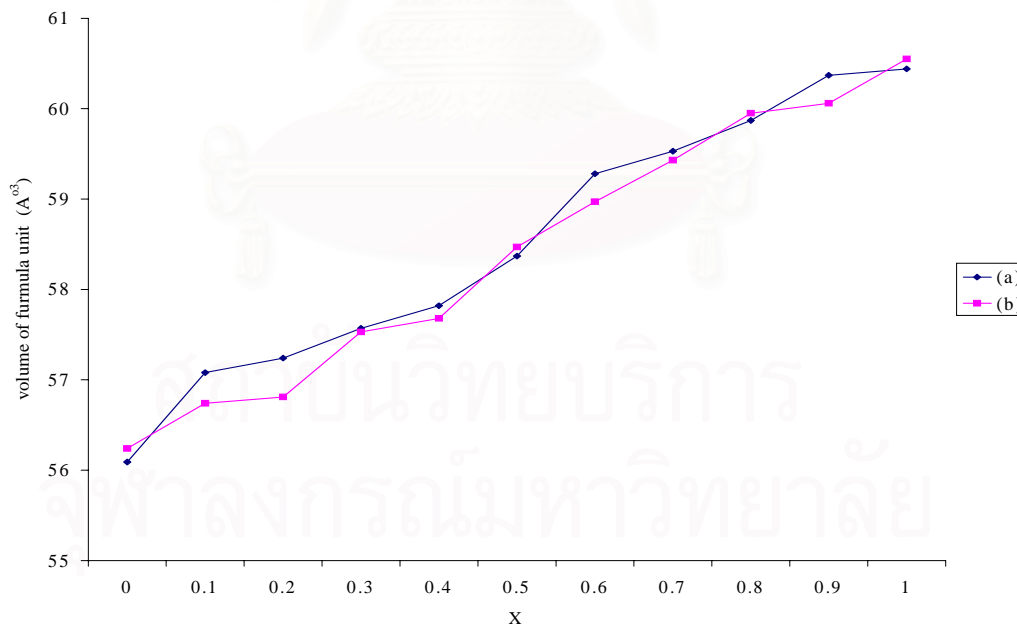


Figure 4.8 The volume of formula unit of $\text{LaNi}_{1-x}\text{Fe}_x\text{O}_3$ ($x = 0.0-1.0$) perovskite, synthesized by (a) WC (b) MWC, and calcined at $900\text{ }^\circ\text{C}$ for 5h.

It is clear to see the increasing trend of the volume per formula unit when Fe content increases. This is simply explained by the reason that the Fe ion radius (0.64 Å) is larger than that of Ni ion (0.56 Å). This increasing trend was previously reported by Chiba *et al.* [5]. The group investigated the same series of $\text{LaNi}_{1-x}\text{Fe}_x\text{O}_3$ ($x = 0-1.0$), synthesized by solid state method. Using the calcination temperature of 900 °C when $x = 0.4$, their samples are orthorhombic, which is the same structure as that of LaFeO_3 . As $x = 0.3$ and 0.2, their samples are basically in the rhombohedral phase, with a trace amount of the orthorhombic phase. As $x < 0.2$, their samples are a mixture of the orthorhombic and tetragonal phases. [5] Despite of the same trend of the volume per formula unit, all compositions are single-phased in this thesis. Unlike the conventional solid-state synthesis that generally uses the powder of metal carbonate and metal oxide as the reactants, the combustion method starts with the mixing of the solution of metal ion in a stoichiometric ratio. Thus, all metallic components distribute homogeneously in the solution. Moreover, the citrate anion used in this thesis acts as a chelating agent of these metal ions. The self-combustion process releases the heat throughout the reaction chambers, in order to convert metal citrate complexes to perovskite oxides. The solid state synthesis, on the other hand, needs high temperature to induce the metal ion in solid lattice of one reactant to diffuse into the lattice of another reactant, and forms the desired complex; therefore, the method takes long time. The purity of the products also depends on the grain size of starting materials. The starting materials with large grain sizes require higher diffusion ability to be able to be homogeneous. Many desired products that are unstable at high temperature cannot be obtained by solid state synthesis.

F. The phase diagram of LNF perovskite powders

Within the series of $\text{LaNi}_{1-x}\text{Fe}_x\text{O}_3$, LNF-37 and LNF-64 were chosen as the representatives of two structural systems for high and low Fe contents, respectively. There are other reasons of choosing these two compositions, based on their superior catalytic and electronic properties, respectively.

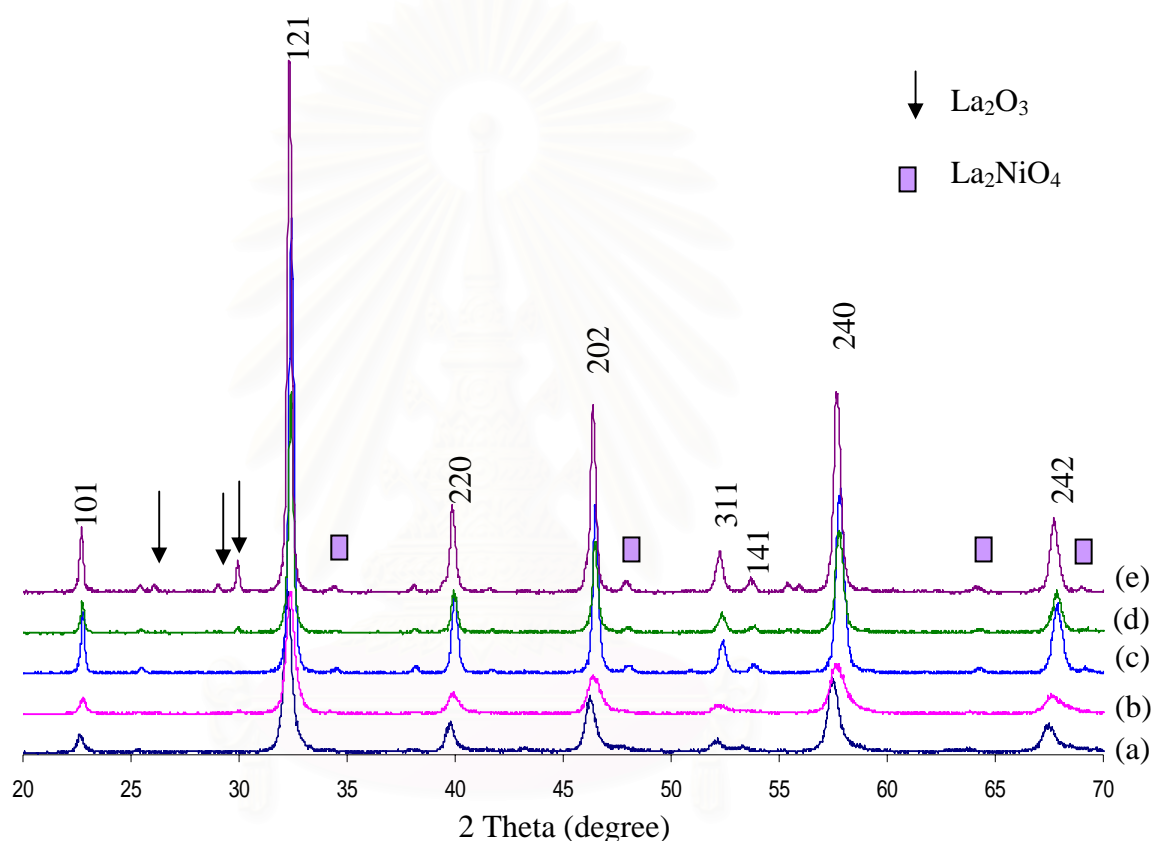


Figure 4.9 XRD patterns of LNF-37 perovskite powder after being calcined at (a) 700 °C 5h (b) 800 °C 5h (c) 900 °C 5h (d) 1000 °C 5h and (e) 1200 °C for 5h.

Figure 4.9 shows the XRD patterns of LNF-37 perovskite powders. The XRD patterns of LNF-37 at 700-1200 °C were obtained in order to investigate its phase stability. The sample remains single-phased up to 900 °C. At 1000 °C, the small amount of La_2O_3 (JCPDS: 24-0554) was observed. At 1200 °C, the fingerprint of La_2O_3 was clearly seen. The higher and shaper peaks of perovskite are due to the larger grain

size after firing at higher temperature. The LNF-37 perovskite powder is unstable above 900 °C and decomposes to La_2NiO_4 (JCPDS: 34-0314) [5, 6] and La_2O_3 .

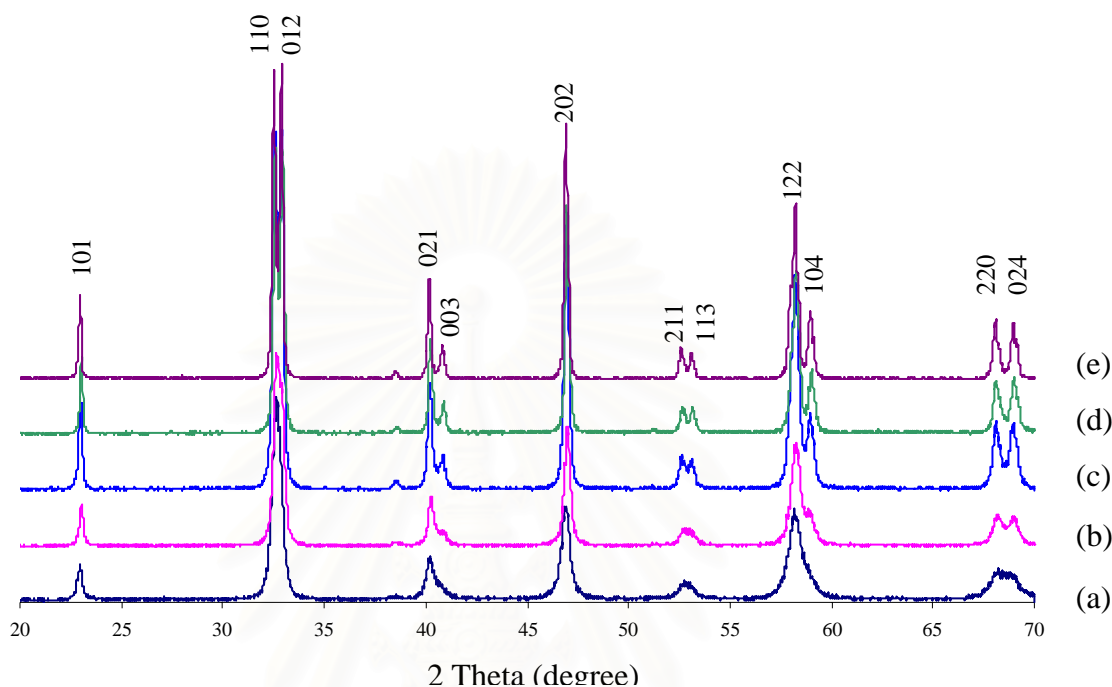


Figure 4.10 XRD patterns of LNF-64 perovskite powder after being calcined at (a) 700 °C 5h (b) 800 °C 5h (c) 900 °C 5h (d) 1000 °C 5h and (e) 1200 °C for 5h.

Unlike LNF-37, the structural change of LNF-64 perovskite powder is clearly observed around the calcination temperature of 800-900 °C, as shown in the XRD patterns (Figure 4.10). The sample is cubic at 700-800 °C, and becomes rhombohedral at 900-1200 °C. Despite of the phase change, LNF-64 still maintains only single phase from room temperature up to 1200 °C.

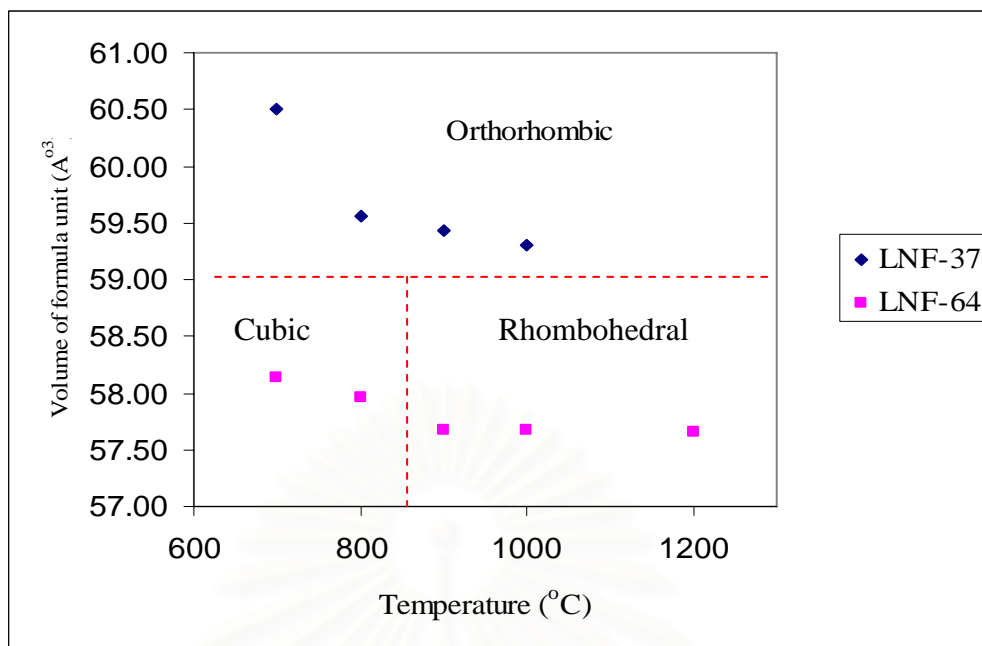


Figure 4.11 The structural phase diagrams of LNF-37 and LNF-64.

Since the Fe ion can form complexes with more varieties of oxidation states and shapes than the Ni ion can, this flexibility allows the structural change of LNF-64 and maintains its phase homogeneity at high temperature at the same time.

4.1.2 The comparison of four combustion methods in the synthesis of LNF-64

As previously mentioned, LNF-64 has a high potential as a cathode for IT-SOFC because the high electrical conductivity and the suitable thermal expansion. It was selected here to study the effect of different synthesis methods, including WC, MWC, NC and MNC by means of the structure and the particle size.

As shown in Figure 4.12, the structures of LNF-64 synthesized by four combustion methods gave the same structure, similar to that of LaNiO_3 , with the lattice parameters of 5.4570 Å, 5.4570 Å, 6.5720 Å. The difference was found in the term of particle size as shown in Table 4.7. The particle sizes of LNF-64 can be arranged from the smallest to the largest by synthesis using the methods of MNC, MWC, WC and NC, respectively. These results were further confirmed by SEM. The particle size distribution profiles are presented in Appendix C.

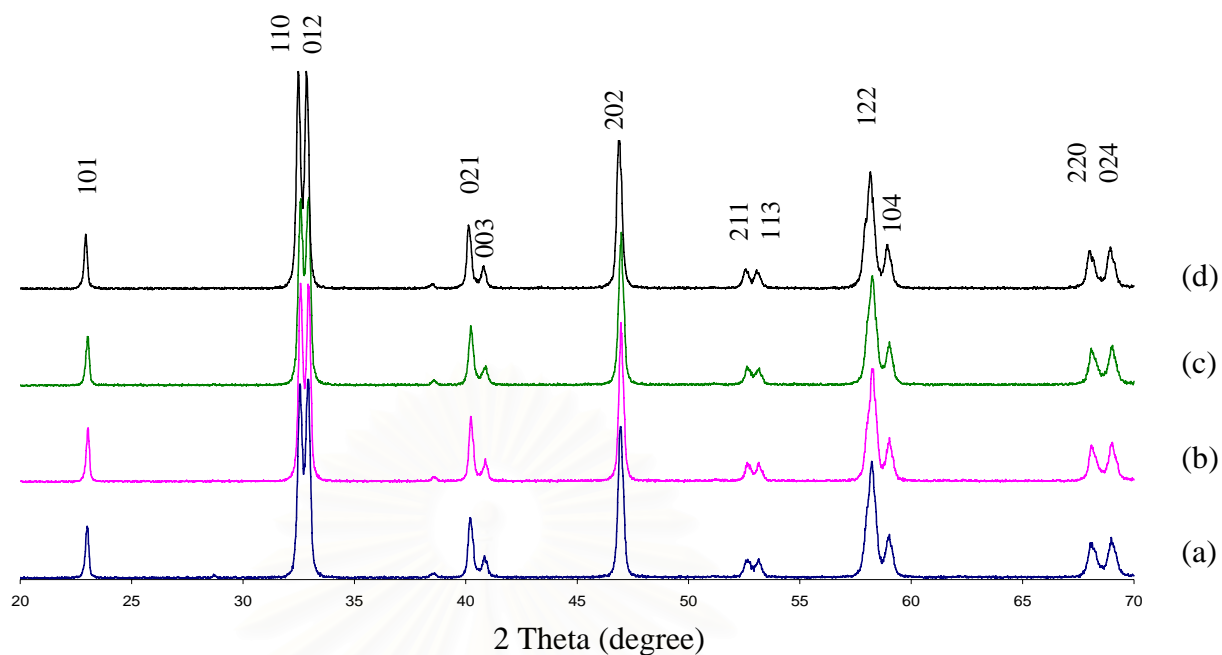


Figure 4.12 XRD patterns of LNF-64, synthesized by four methods (a) WC, (b) MWC, (c) NC, and (d) MNC with the calcination temperature of 1000 °C for 5 h.

Table 4.7 Particle size-distribution of LNF-64 by four combustion methods

Method	Particle size (μm)	
	The highest population	The 2 nd highest population
WC	4.61	1.71
NC	3.46	1.15
MWC	2.61	0.08
MNC	1.61	-

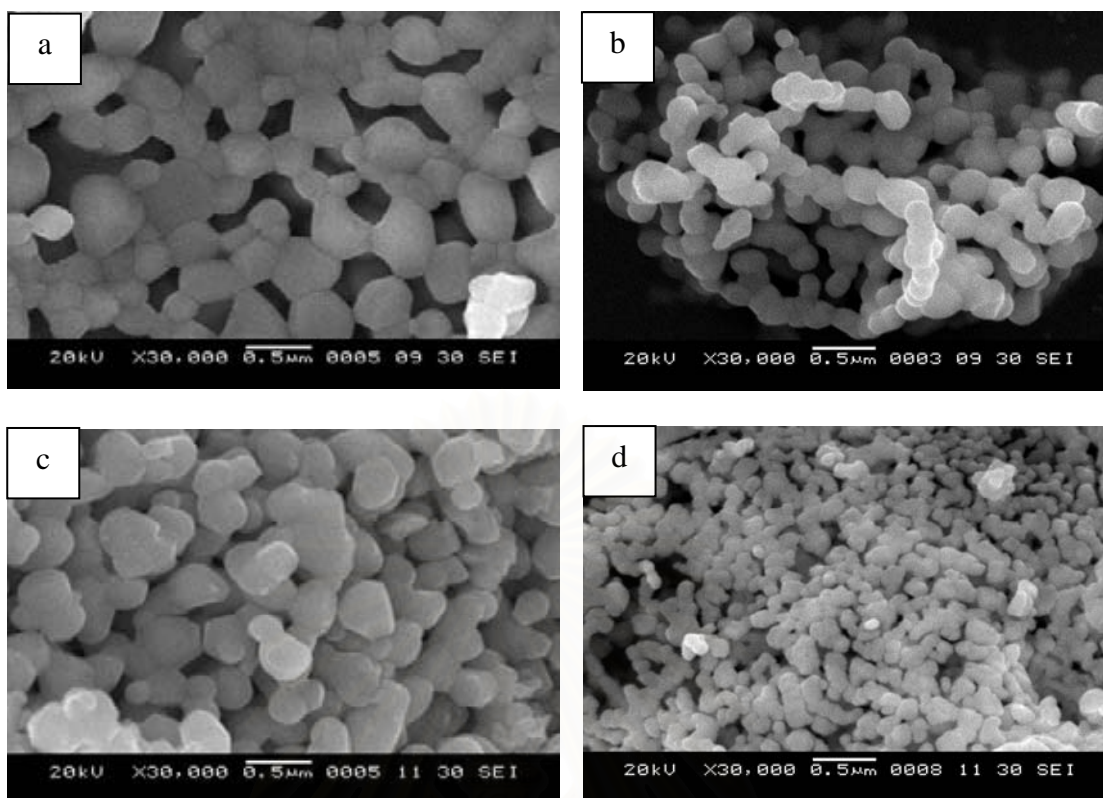


Figure 4.13 SEM pictures of LNF-64 with the calcination temperature of 1000 °C for 5 h (a) WC (b) MWC (c) NC (d) MNC.

The increasing trend of particle size was confirmed by SEM results. The size of MNC ($\sim 0.17 \mu\text{m}$) were found to be the smallest, followed by that of MWC ($\sim 0.26 \mu\text{m}$) NC ($\sim 0.35 \mu\text{m}$) and WC ($\sim 0.45 \mu\text{m}$) respectively. The difference in a particle size is due to the nature of powder synthesis process. The exothermic auto-ignition process is fuel-rich for modified citrate method (MNC and MWC) because of the addition of ammonia during the complexation step, where tiny glowing flints propagate within in the mixture at the combustion step until the reaction completes. For unmodified method, without an additional ammonia as a fuel, the low ignition temperature from fuel-lean results to non-uniform heat distribution and leads to the small particle size.

The MNC method was selected in synthesis of perovskite because it resulted to the particles with narrow pore size distribution and small particle size, which can form the homogenous and dense cathode membrane for SOFC by the sintering process.

4.1.3 Chemical compatibility with 8-YSZ electrolyte

4.1.3.1 The mixtures of LNF-64 perovskite powders with 8-YSZ

The chemical compatibility of both stoichiometric and non-stoichiometric LNF-64 perovskites was investigated in its mixture with 8-YSZ of 50/50 wt % at room temperature to 1200 °C. The new phase(s) formed by the undesired chemical reaction was followed by XRD and characterized using the JCDPS database.

A. Stoichiometric perovskite of $\text{La}(\text{Ni}_{0.6}\text{Fe}_{0.4})_y\text{O}_3$ ($y = 1.00$) with 8-YSZ mixtures

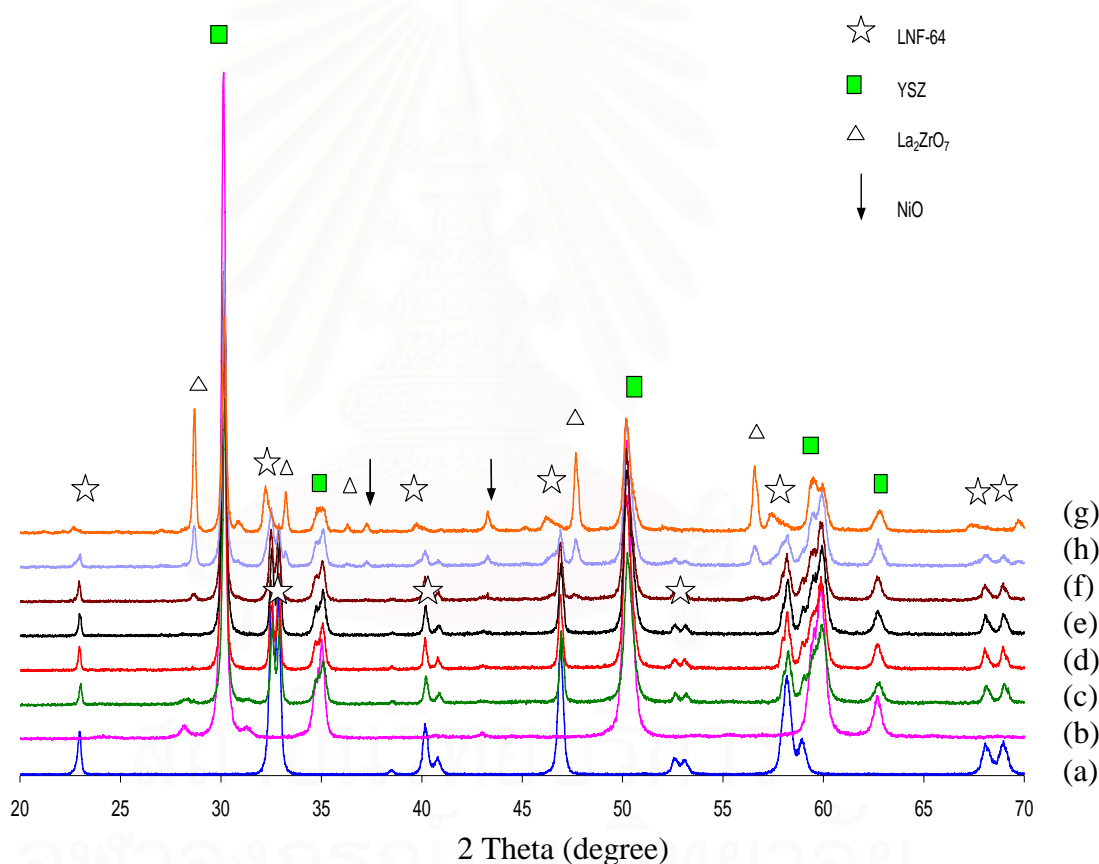


Figure 4.14 XRD patterns of (a) LNF-64 ($y = 1.00$), (b) 8-YSZ, and the powder mixtures between LNF-64 ($y = 1.00$) and 8-YSZ: (c) the mixtures at room temperature, (d) after calcination at 800°C for 5h, (e) after calcination at 900°C for 5h, (f) after calcination at 1000 °C for 5h, (g) after calcination at 1100 °C for 5h, and (h) after calcination 1200 °C for 5h.

Table 4.8 The presence of undesired phase(s) in the powder mixtures between LNF-64 ($y = 1.00$) and 8-YSZ after calcination at various temperatures for 5h

The calcination temperature (°C)	Synthesis methods			
	WC	MWC	NC	MNC
RT	none	none	none	none
800	none	none	none	none
900	none	none	none	none
1000	trace amount of $\text{La}_2\text{Zr}_2\text{O}_7$	trace amount of $\text{La}_2\text{Zr}_2\text{O}_7$	trace amount of $\text{La}_2\text{Zr}_2\text{O}_7$	trace amount of $\text{La}_2\text{Zr}_2\text{O}_7$
1100	$\text{La}_2\text{Zr}_2\text{O}_7$ and NiO	$\text{La}_2\text{Zr}_2\text{O}_7$ and NiO	$\text{La}_2\text{Zr}_2\text{O}_7$ and NiO	$\text{La}_2\text{Zr}_2\text{O}_7$ and NiO
1200	$\text{La}_2\text{Zr}_2\text{O}_7$ and NiO	$\text{La}_2\text{Zr}_2\text{O}_7$ and NiO	$\text{La}_2\text{Zr}_2\text{O}_7$ and NiO	$\text{La}_2\text{Zr}_2\text{O}_7$ and NiO

$\text{La}(\text{Ni}_{0.6}\text{Fe}_{0.4})_y\text{O}_3$ ($y = 1.00$) is designated in this section as LNF-64 ($y = 1.00$). The XRD results show in Figure 4.14, and Table 4.8 summarizes the undesired specie found at different calcination temperatures. The patterns at the calcination temperatures of 800-900°C contains the peaks of LNF-64 ($y = 1.00$) and 8-YSZ only, indicating the good chemical compatibility from room temperature up to 900°C. Besides the original components, the new phases of $\text{La}_2\text{Zr}_2\text{O}_7$ (JCDPS: 17-0450) started to form at 1000°C. At 1100 and 1200°C, the $\text{La}_2\text{Zr}_2\text{O}_7$ and NiO (JCPDS: 47-1049) phases were clearly observed and the original components disappeared.

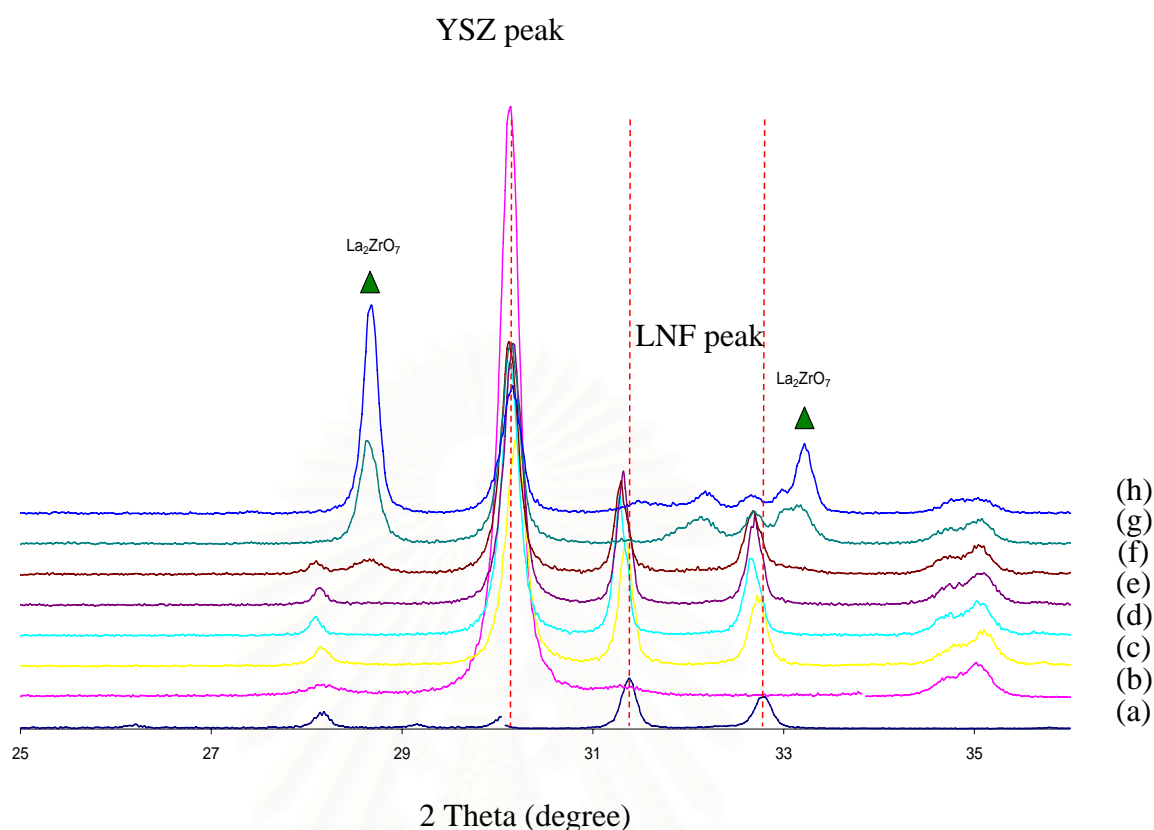


Figure 4.15 XRD patterns between a 2θ range of $25\text{-}36^\circ$ of (a) LNF-64 ($y = 1.00$), (b) 8-YSZ, and the powder mixtures between LNF-64 ($y = 1.00$) and 8-YSZ: (c) the mixtures at room temperature, (d) after calcination at 800°C for 5h, (e) after calcination at 900°C for 5h, (f) after calcination at 1000°C for 5h, (g) after calcination at 1100°C for 5h, and (h) after calcination 1200°C for 5h.

In Figure 4.15, the portion of XRD with a 2θ range of $25\text{-}36^\circ$ was blown up. The shift of the LNF peaks to the lower diffraction angle indicates the volume expansion of perovskite phase, caused by the dissolution of larger Zr cations into the perovskite structure [48, 50]. Even though the new phases were not found at lower temperature by XRD, the small amount of Zr may exist in the LNF structure as the impurity atom.

B. Non-stoichiometric perovskite of $\text{La}(\text{Ni}_{0.6}\text{Fe}_{0.4})_y\text{O}_3$

($y = 0.95$) with 8-YSZ mixtures

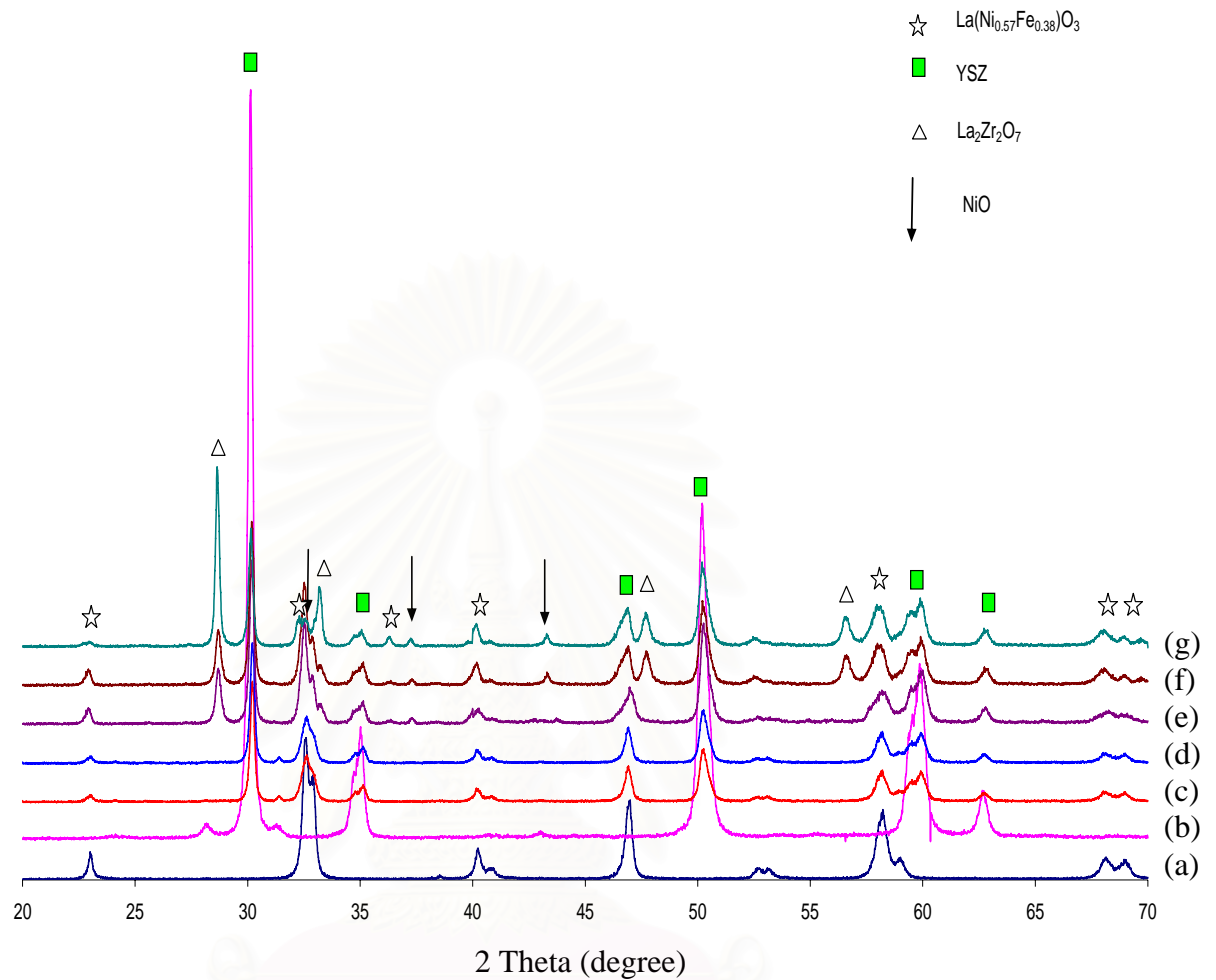


Figure 4.16 XRD patterns of (a) LNF-64 ($y = 0.95$), (b) 8-YSZ, and the powder mixtures between LNF-64 ($y = 0.95$) and 8-YSZ: (c) the mixtures at room temperature, (d) after calcination at 800°C for 5h, (e) after calcination at 900°C for 5h, (f) after calcination at 1000 °C for 5h, and (g) after calcination at 1100 °C for 5h.

Table 4.9 The presence of undesired phase(s) in the powder mixtures between LNF-64 ($y = 0.95$) and 8-YSZ after calcination at various temperatures for 5h

The calcination temperature (°C)	Synthesis methods	
	MWC	MNC
RT	none	none
800	none	none
900	La ₂ Zr ₂ O ₇ and NiO	La ₂ Zr ₂ O ₇ and NiO
1000	La ₂ Zr ₂ O ₇ and NiO	La ₂ Zr ₂ O ₇ and NiO
1100	La ₂ Zr ₂ O ₇ and NiO	La ₂ Zr ₂ O ₇ and NiO

La(Ni_{0.6}Fe_{0.4})_yO₃ ($y = 0.95$) is designated in this section as LNF-64 ($y = 0.95$). The XRD results show in Figure 4.16, and Table 4.9 summarizes the undesired specie found at different calcination temperatures. The patterns at the calcination temperatures of 800 °C contains the peaks of LNF-64 ($y = 1.00$) and 8-YSZ only, indicating the good chemical compatibility from room temperature to 800°C only. Besides the original components, the new phases of La₂Zr₂O₇ (JCDPS: 17-0450) and NiO (JCPDS: 47-1049) started to form at 900°C. At 1000-1100°C, the La₂Zr₂O₇ and NiO phases were clearly observed and the original components disappeared.

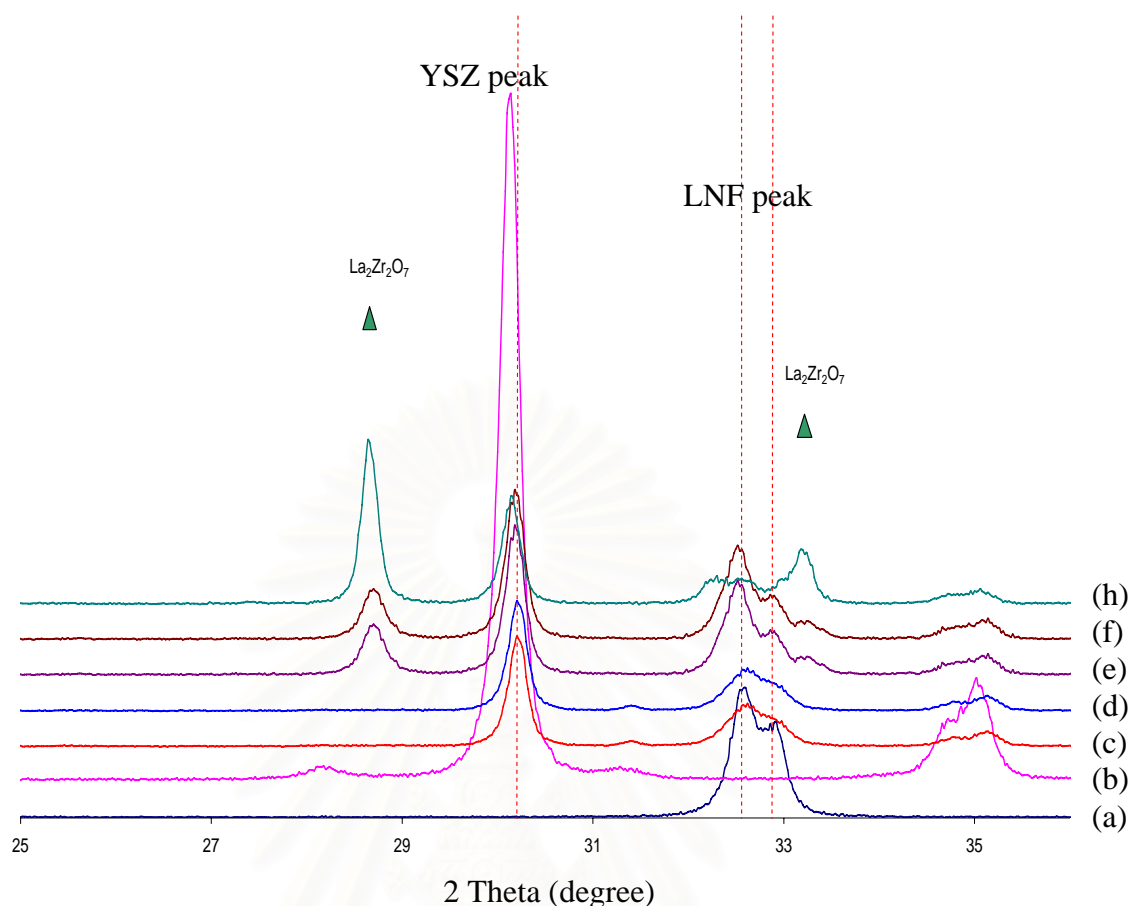


Figure 4.17 XRD patterns between a 2θ range of $25\text{-}36^\circ$ of (a) LNF-64 ($y = 0.95$), (b) 8-YSZ, and the powder mixtures between LNF-64 ($y = 0.95$) and 8-YSZ: (c) the mixtures at room temperature, (d) after calcination at 800°C for 5h, (e) after calcination at 900°C for 5h, (f) after calcination at 1000°C for 5h and (h) after calcination at 1100°C for 5h.

In Figure 4.17, the portion of XRD with a 2θ range of $25\text{-}36^\circ$ was blown up. The small shift of the LNF peaks to the lower diffraction angle indicates the volume expansion of perovskite phase, caused by the dissolution of larger Zr cations into the perovskite structure [48, 50]. Even though the new phases were not found at lower temperature by XRD, the small amount of Zr may exist in the LNF structure as the impurity atom.

C. Non-stoichiometric perovskite of $\text{La}(\text{Ni}_{0.6}\text{Fe}_{0.4})_y\text{O}_3$
($y = 1.05$) with 8-YSZ mixtures

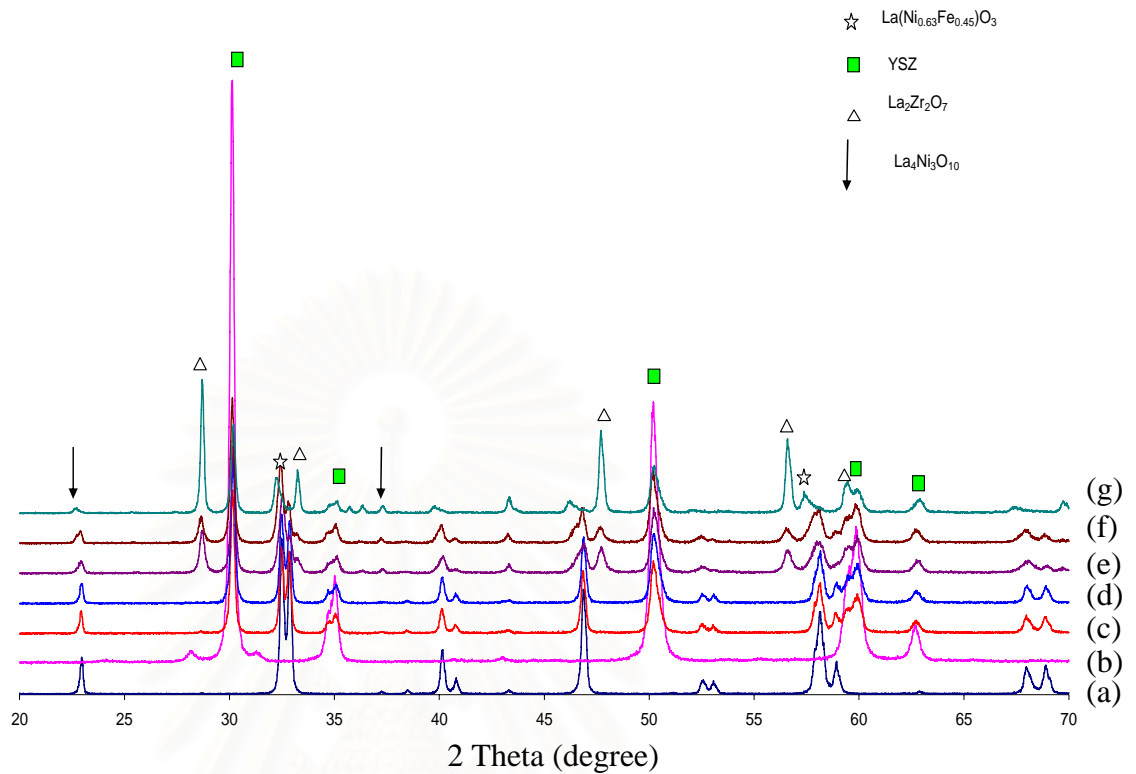


Figure 4.18 XRD patterns of (a) LNF-64 ($y = 1.05$), (b) 8-YSZ, and the powder mixtures between LNF-64 ($y = 1.05$) and 8-YSZ: (c) the mixtures at room temperature, (d) after calcination at 800°C for 5h, (e) after calcination at 900°C for 5h, (f) after calcination at 1000°C for 5h and (g) after calcination 1200°C for 5h.

สถาบันวิทยบริการ
 จุฬาลงกรณ์มหาวิทยาลัย

Table 4.10 The presence of undesired phase(s) in the powder mixtures between LNF-64 ($y = 0.95$) and 8-YSZ after calcination at various temperatures for 5h

The calcination temperature (°C)	Synthesis methods	
	MWC	MNC
RT	none	none
800	none	none
900	La ₂ Zr ₂ O ₇ and La ₄ Ni ₃ O ₁₀	La ₂ Zr ₂ O ₇ and La ₄ Ni ₃ O ₁₀
1000	La ₂ Zr ₂ O ₇ and La ₄ Ni ₃ O ₁₀	La ₂ Zr ₂ O ₇ and La ₄ Ni ₃ O ₁₀
1100	La ₂ Zr ₂ O ₇ and La ₄ Ni ₃ O ₁₀	La ₂ Zr ₂ O ₇ and La ₄ Ni ₃ O ₁₀

La(Ni_{0.6}Fe_{0.4})_yO₃ ($y = 0.95$) is designated in this section as LNF-64 ($y = 0.95$). The XRD results show in Figure 4.18 and Table 4.10 summarizes the undesired specie found at different calcination temperatures. The patterns at the calcination temperatures of 800 °C contains the peaks of LNF-64 ($y = 1.00$) and 8-YSZ only, indicating the good chemical compatibility from room temperature to 800°C only. Besides the original components, the new phases of La₂Zr₂O₇ (JCDPS: 17-0450) and La₄Ni₃O₁₀ (JCDPS: 83-1164) started to form at 900°C. At 1000-1100°C, the La₂Zr₂O₇ and La₄Ni₃O₁₀ phases were clearly observed and the original components disappeared.

สถาบันวิทยบริการ
จุฬาลงกรณ์มหาวิทยาลัย

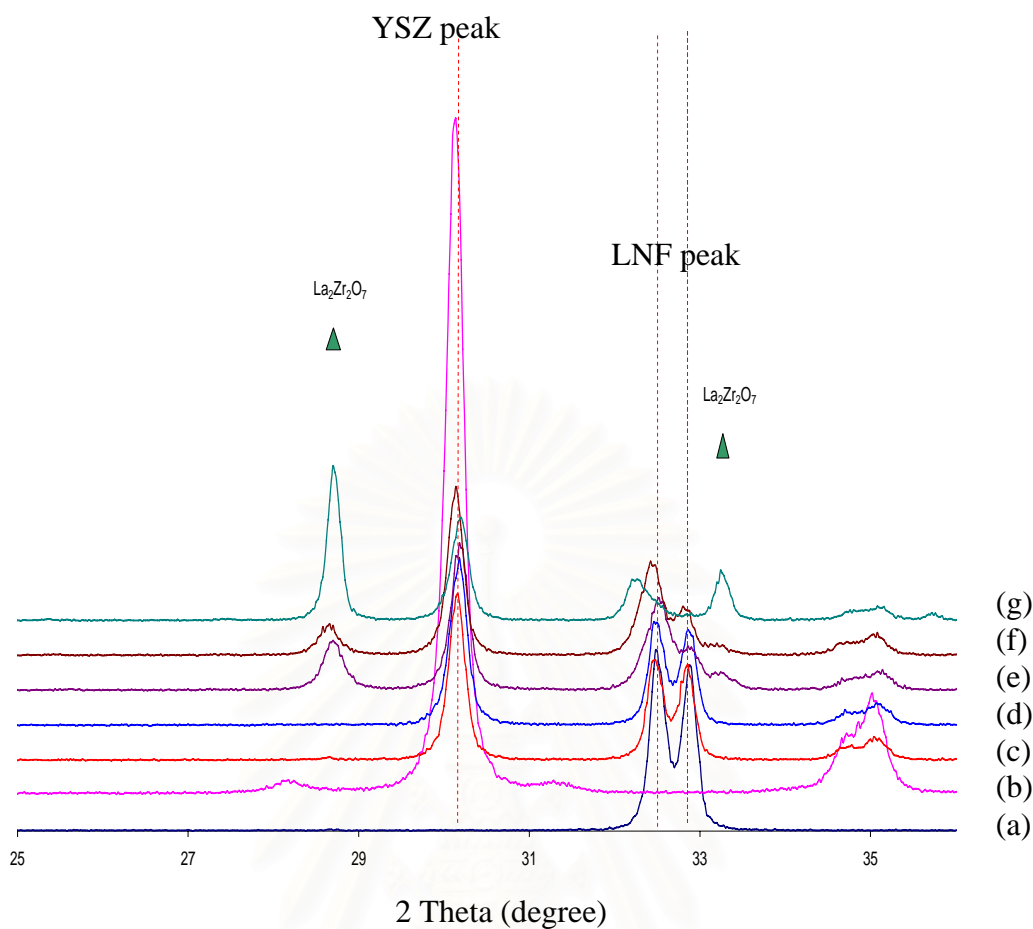


Figure 4.19 XRD patterns between a 2θ range of $25\text{-}36^\circ$ of (a) LNF-64 ($y = 1.05$), (b) 8-YSZ, and the powder mixtures between LNF-64 ($y = 1.05$) and 8-YSZ: (c) the mixtures at room temperature, (d) after calcination at 800°C for 5h, (e) after calcination at 900°C for 5h, (f) after calcination at 1000°C for 5h and (g) after calcination at 1100°C for 5h.

The portion of XRD with a 2θ range of $25\text{-}36^\circ$ was blown up in Figure 4.19. The small shift of the LNF peaks to the lower diffraction angle indicates the volume expansion of perovskite phase, caused by the dissolution of larger Zr cations into the perovskite structure [48, 50]. Even though the new phases were not found at lower temperature by XRD, the small amount of Zr may exist in the LNF structure as the impurity atom.

4.1.3.2 The membrane of LNF-64 perovskite powder with 8-YSZ

To simulate the SOFC configuration, the chemical compatibility was studied at the surface between LNF-64 and 8-YSZ. The LNF64 prepared by MNC method route was chosen in this studied since it has a smallest particle size. The screen-printing technique was used to apply LNF-64 powder on 8-YSZ electrolyte pellet. From section 4.1.3.1 A, it was found that the LNF-64 can withstand the reaction with 8-YSZ up to 900 °C; therefore, in this section the study was focused on the temperature at 900 °C and 1000 °C to observe any change corresponding to the XRD results. The membrane of LNF-64 and 8-YSZ was cross-sectioned and its metallic composition was detected by SEM Maps (mode-ID-point technique).



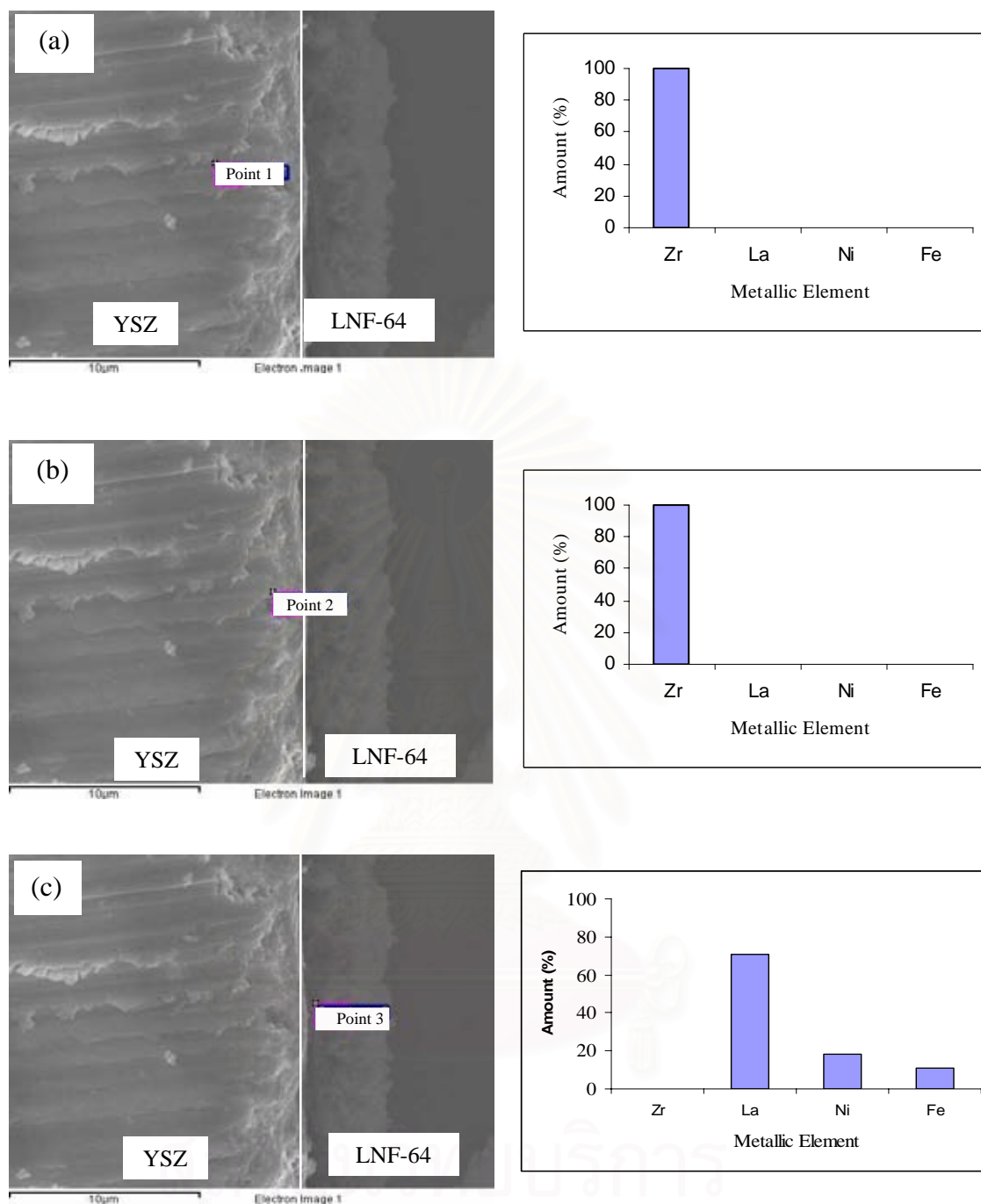


Figure 4.20 SEM-Maps (mode-ID-point technique) of the cross-sectioned LNF-64 (MNC method)/8-YSZ pellet after calcination at 900°C for 5 h, detected at (a) point 1, (b) point 2, and (c) point 3.

Table 4.11 The weight percentage of metallic elements of the cross-sectioned LNF-64 (MNC method)/8-YSZ pellet after calcination at 900°C for 5 h, summarized by SEM-Maps (ID-point technique)

Metallic Element	Amount (wt %)		
	point 1	point 2	point 3
Zr	100	100	0
La	0	0	70.51
Ni	0	0	18.36
Fe	0	0	11.13

From Figure 4.20, and table 4.11, there is only Zr as the metallic element at point 1 and 2, both located within the side of 8-YSZ pellet. At point 3, only La, Ni, and Fe were found. This result confirms XRD results in section 4.1.3.1 A that the reaction between LNF-64 and 8-YSZ does not occur at 900°C. In the other words, the prepared LNF-64 was found to have a good chemical compatibility with YSZ at room temperature up to 900°C.

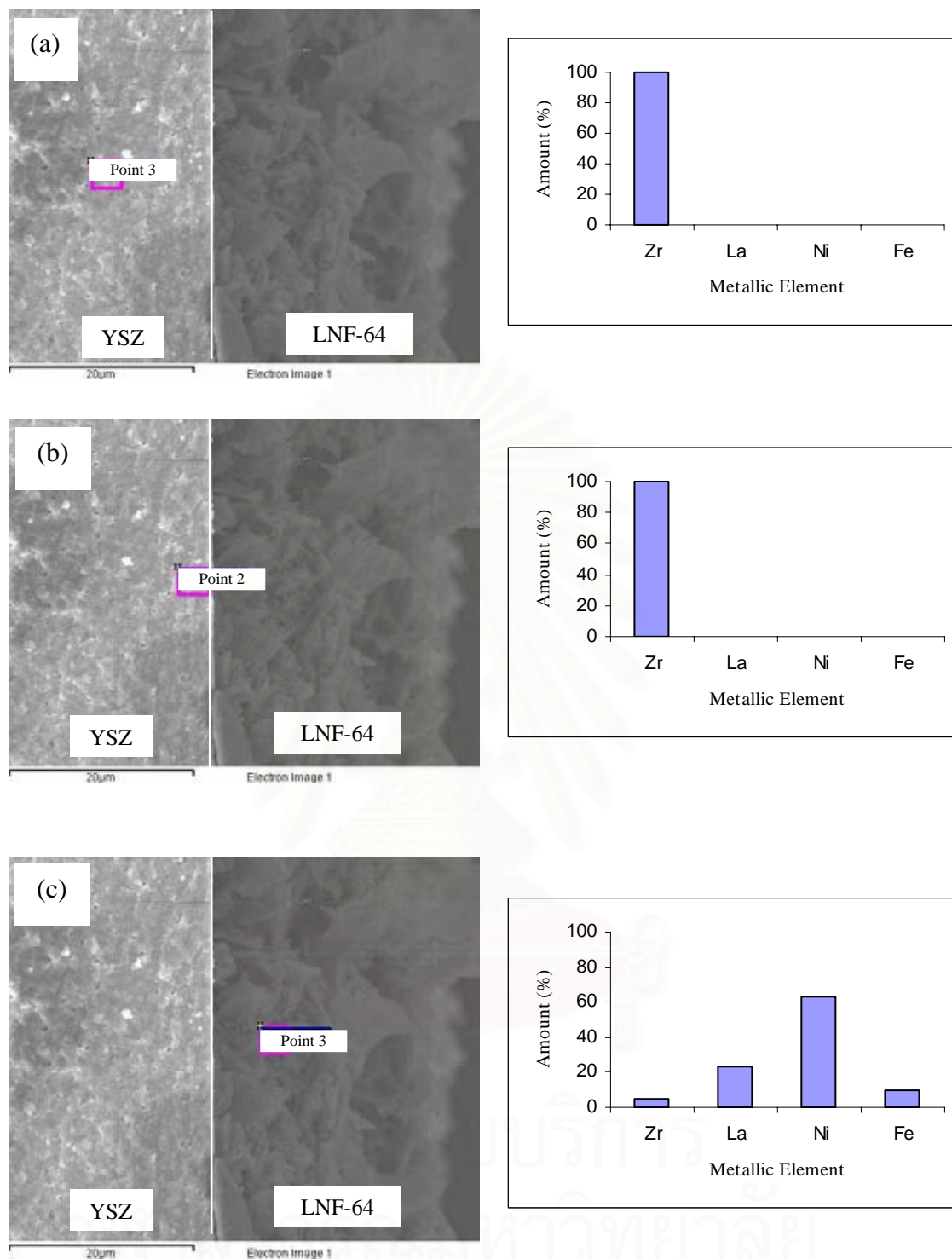


Figure 4.21 SEM-Maps (mode-ID-point technique) of the cross-sectioned LNF-64 (MNC method)/8-YSZ pellet after calcination at 1000°C for 5 h, detected at point 1, (b) point 2, and (c) point 3.

Table 4.12 The weight percentage of metallic elements of the cross-sectioned LNF-64 (MNC method)/8-YSZ pellet after calcination at 1000°C for 5 h, summarized by SEM-Maps (ID-point technique)

Metallic Element	Amount (wt %)		
	point 1	point 2	point 3
Zr	99.64	99.75	4.37
La	0.10	0.12	22.90
Ni	0.06	0.10	63.50
Fe	0.20	0.03	9.23

From Figure 4.21 and table 4.12, the small amount of La, Ni, and Fe were found at point 1 and 2, both locating within the side of 8-YSZ pellet. At point 3 locating within the side of LNF-64, the small amount of Zr was found. Again, this result confirms XRD results in section 4.3.1.1 A that the unwanted reaction between LNF-64 and 8-YSZ starts at 1000°C.

4.1.4 Physical compatibility of LNF-64 with 8-YSZ electrolyte

The physical compatibility between LNF and 8-YSZ was investigated in term of the thermal expansion coefficient (TEC). The closed TEC values of both materials are the requirement in use as the components for SOFC.

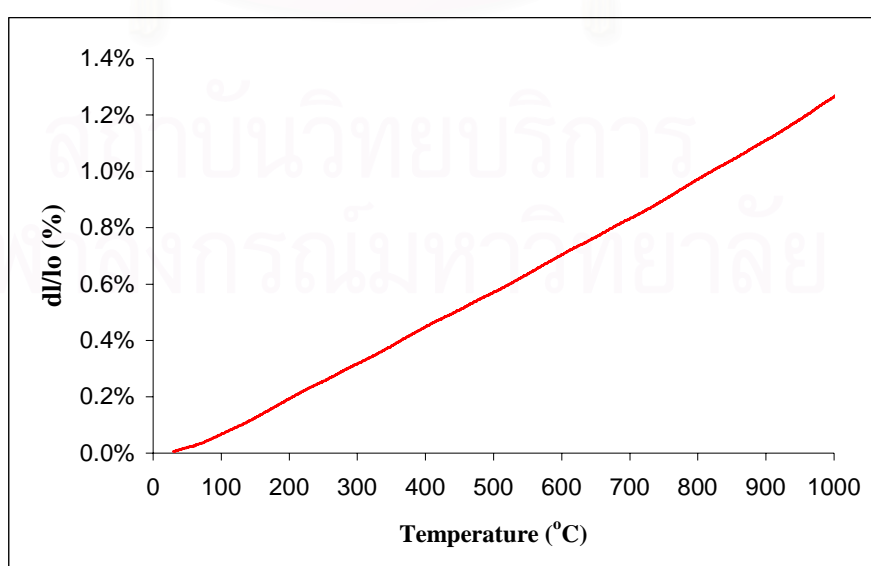


Figure 4.22 The thermal expansion behavior of LNF-64, prepared by MNC method.

Figure 4.22 shows the thermal expansion behavior of LNF-64, its slope indicates TEC of materials at each temperature. The straight line was obtained for LNF-64, indicating the constant TEC values of $13.2 \times 10^{-6} \text{ K}^{-1}$ from room temperature up to $1000 \text{ }^\circ\text{C}$.

Table 4.13 The thermal expansion coefficients of LNF-64 samples and 8-YSZ at $800 \text{ }^\circ\text{C}$

Materials	Synthesis method (s)	TEC ($\times 10^{-6} \text{ K}^{-1}$)
LNF-64 [in this thesis]	MNC	13.2
^a LNF-64	Citrate gel and urea	11.8
^b LNF-64	Solid state reaction	11.4
^c $\text{La}_{0.8}\text{Sr}_{0.2}\text{Fe}_{0.9}\text{Co}_{0.1}\text{O}_3$	Solid state reaction	13.9
^c $\text{Pr}_{0.8}\text{Sr}_{0.2}\text{Fe}_{0.8}\text{Co}_{0.2}\text{O}_3$	Solid state reaction	13.2
^d 8-YSZ	-	10.5

^aBasu *et al.* [18], ^bChiba *et al.* [5], ^cDaroukh *et al.* [26], and ^dSingnal *et al.* [4]

The thermal expansion coefficient of LNF-64, obtained in this thesis, is higher than those previously reported of the same materials, as shown in Table 4.13. This may be explained that the materials synthesized by MNC methods has the smallest particle size, which causes the best packing efficiency during the preparation of TEC sample bars. The smaller particles are more close-packed during loading and packing steps. The firing step also causes the shrinkage of the sample bar. Therefore, the increase of a bar length to the original length can be obtained during the TEC test. However, the TEC of LNF-64, synthesized in this thesis, is still in the same range with that of 8-YSZ. It could be concluded here that LNF-64 has the good physical compatibility with 8-YSZ.

4.2 K_2NiF_4 powders

4.2.1 Crystal structure

A. Crystal structure of $La_2Ni_{1-x}Fe_xO_4$ by the WC method at 700 °C

The XRD patterns of $La_2Ni_{1-x}Fe_xO_4$ ($x = 0.0-1.0$) samples are shown in Figure 4.23. These samples were synthesized by WC method and calcined at 700 °C for 5 h. As x is 0.0-0.1, the pattern of K_2NiF_4 -typed compound was observed; the secondary phase is also formed as La_2O_3 (JCPDS: 24-0554). As x is 0.2-0.5, La_2O_3 and $LaNiO_3$ perovskite (JCPDS: 33-0710) were found. As x 0.6-1.0, La_2O_3 and $LaFeO_3$ perovskite (JCPDS: 37-1493) were fomed WC mehod failed to prepared $La_2Ni_{1-x}Fe_xO_4$ series at 700 °C.

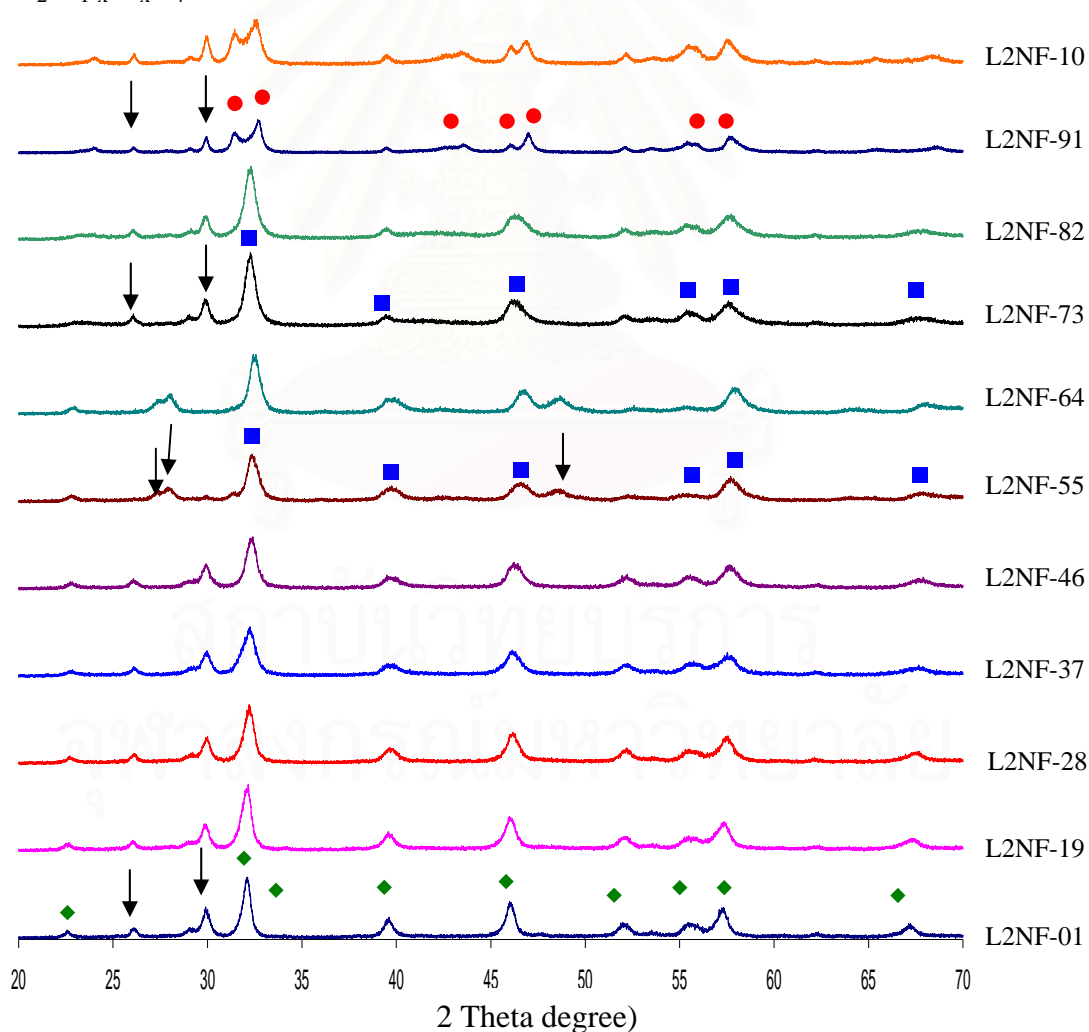


Figure 4.23 XRD patterns of $La_2Ni_{1-x}Fe_xO_4$ ($x = 0.0-1.0$) K_2NiF_4 -typed structure, synthesized by WC method after calcined at 700 °C for 5h.

↓ La_2O_3 , ◆ $LaFeO_3$, ■ $LaNiO_3$ and ● La_2NiO_4

Note:

B. Crystal structure of $\text{La}_2\text{Ni}_{1-x}\text{Fe}_x\text{O}_4$ by the MWC method at 700°C

The XRD patterns of $\text{La}_2\text{Ni}_{1-x}\text{Fe}_x\text{O}_4$ ($x = 0.0-1.0$) samples are shown in Figure 4.24. These samples were synthesized by MWC method and calcined at 700°C for 5 h. The results were the same as found in WC method; therefore, MWC method also failed to prepare $\text{La}_2\text{Ni}_{1-x}\text{Fe}_x\text{O}_4$ series at 700°C .

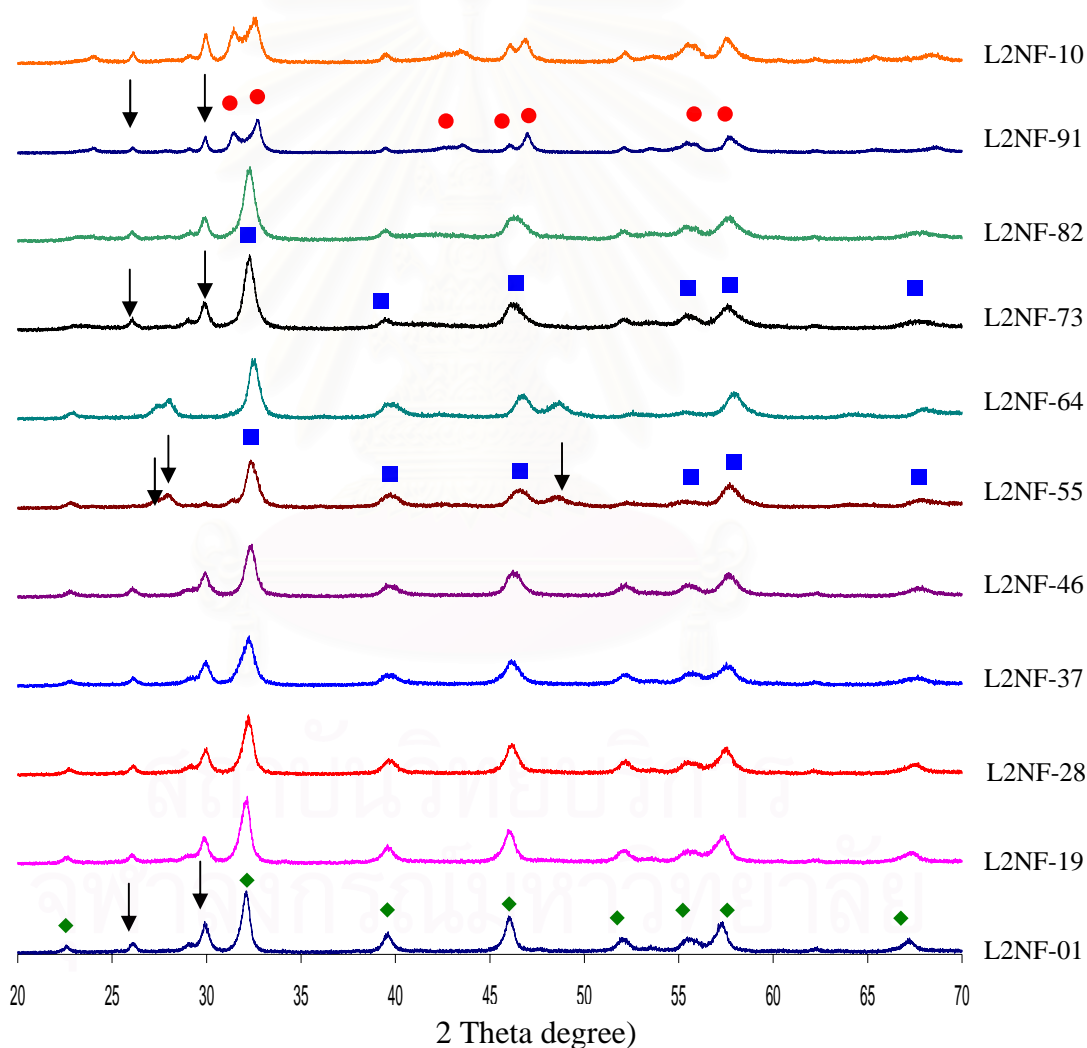
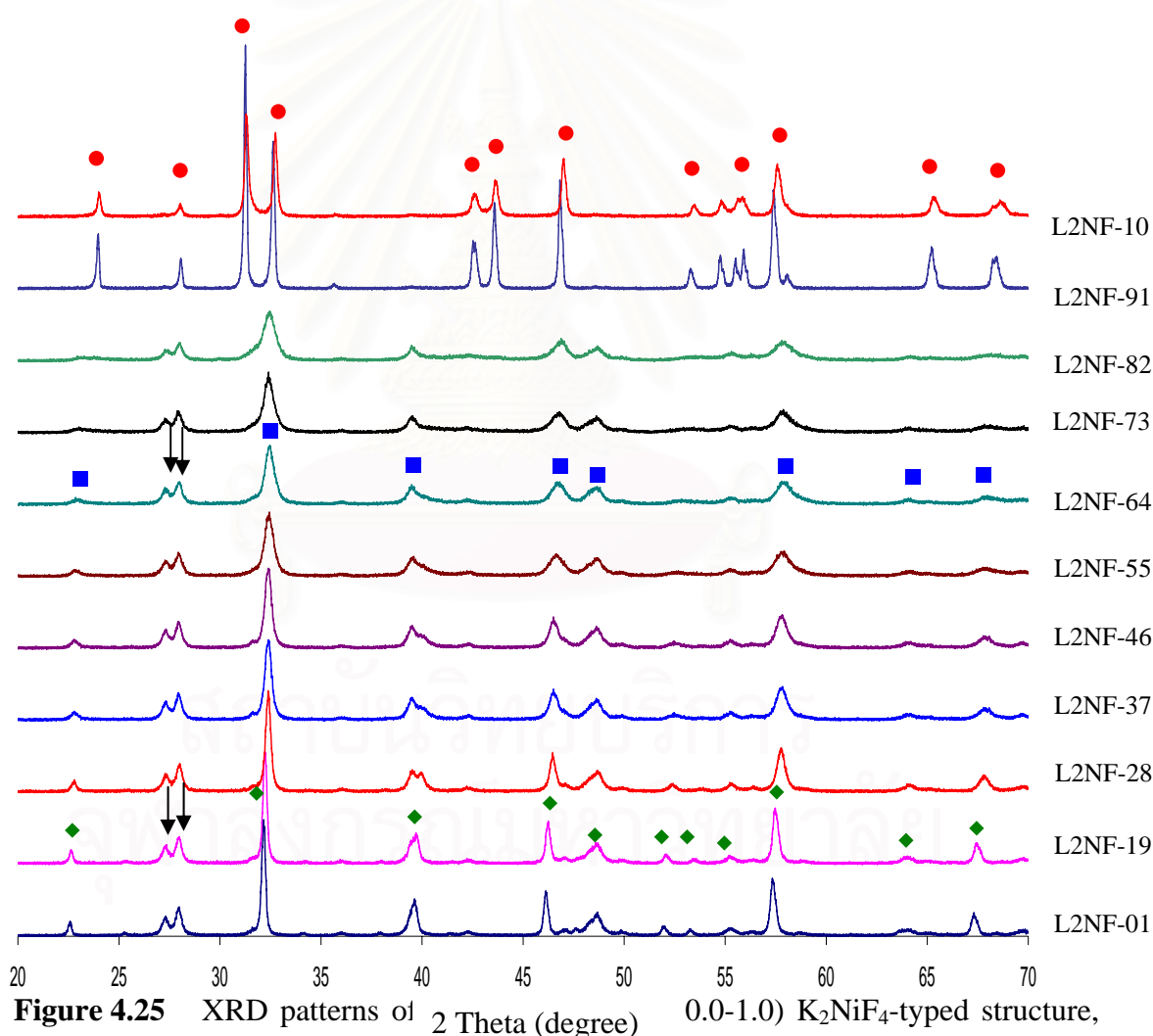


Figure 4.24 XRD patterns of $\text{La}_2\text{Ni}_{1-x}\text{Fe}_x\text{O}_4$ ($x = 0.0-1.0$) K_2NiF_4 -typed structure, synthesized by MWC method and calcined at 700°C for 5h.

Note : \blacktriangledown La_2O_3 , \blacklozenge LaFeO_3 , \blacksquare LaNiO_3 and \bullet La_2NiO_4

C. Crystal structure of $\text{La}_2\text{Ni}_{1-x}\text{Fe}_x\text{O}_4$ by the WC method at $900\text{ }^\circ\text{C}$

The XRD patterns of $\text{La}_2\text{Ni}_{1-x}\text{Fe}_x\text{O}_4$ ($x = 0.0-1.0$) samples are shown in Figure 4.25. These samples were synthesized by WC method and calcined at $900\text{ }^\circ\text{C}$ for 5 h. As x is 0.0 and 0.1, both samples are the single phase of a tetragonal system, which is similar to that of La_2NiO_4 (JCPDS: 34-0314, Figure 4.27). As x is 0.2-0.5, La_2O_3 and LaNiO_3 perovskite (JCPDS: 33-0710) were found. As x 0.6-1.0, La_2O_3 and LaFeO_3 perovskite (JCPDS: 37-1493).



Note : \downarrow La_2O_3 , \blacklozenge LaFeO_3 , \blacksquare LaNiO_3 and \bullet La_2NiO_4

D. Crystal structure of $\text{La}_2\text{Ni}_{1-x}\text{Fe}_x\text{O}_4$ by the MWC method at 900 °C

The XRD patterns of $\text{La}_2\text{Ni}_{1-x}\text{Fe}_x\text{O}_4$ ($x = 0.0-1.0$) samples are shown in Figure 4.26. These samples were synthesized by MWC method and calcined at 900 °C for 5 h. As x is 0.0 and 0.1, both samples are the single phase of a tetragonal system, which is similar to that of La_2NiO_4 (JCPDS: 34-0314, Figure 4.27). As x is 0.2-0.5, La_2O_3 and LaNiO_3 perovskite (JCPDS: 33-0710) were found. As x 0.6-1.0, La_2O_3 and LaFeO_3 perovskite (JCPDS: 37-1493).

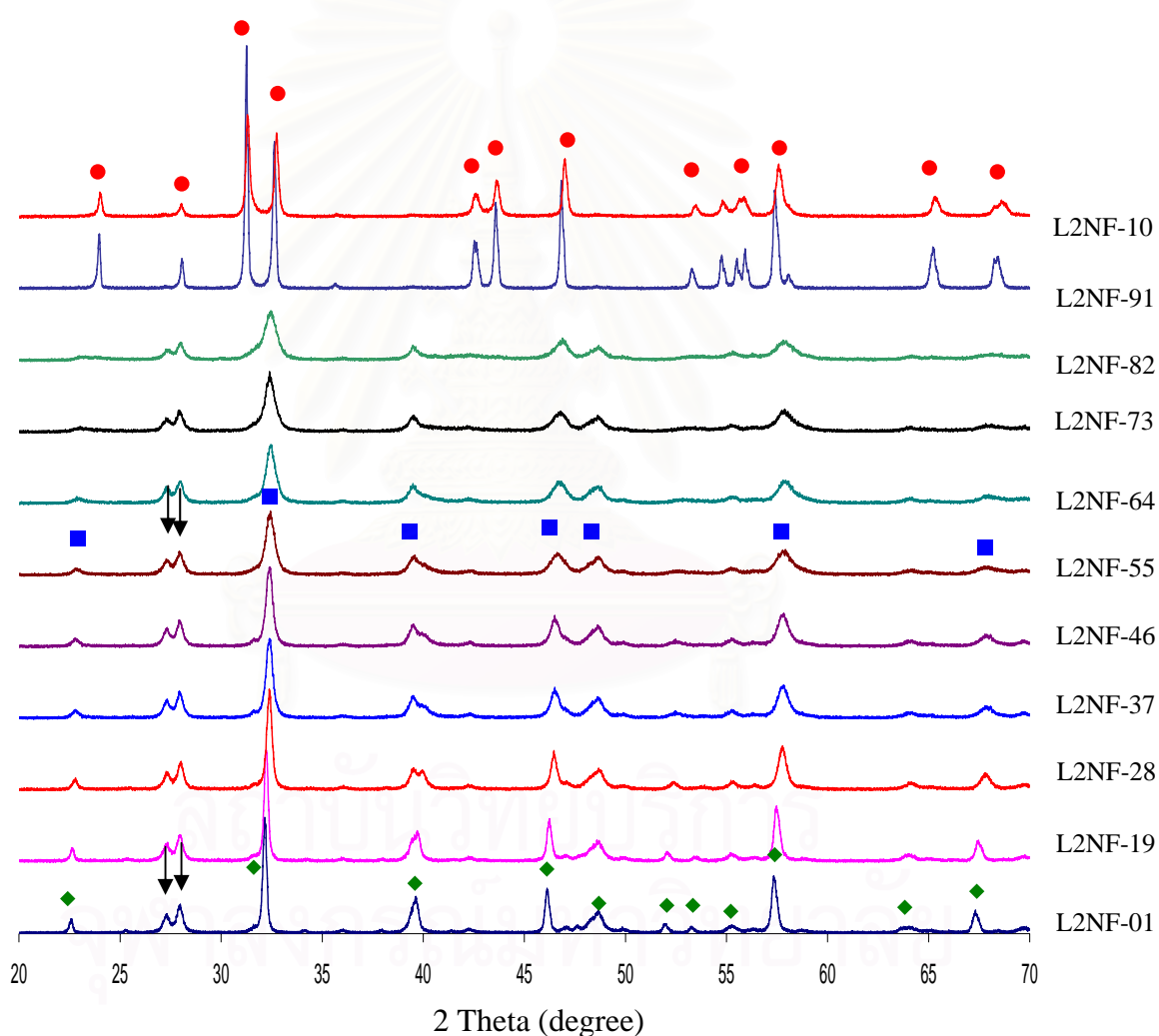


Figure 4.26 XRD patterns of $\text{La}_2\text{Ni}_{1-x}\text{Fe}_x\text{O}_4$ ($x = 0.0-1.0$) K_2NiF_4 -typed structure, synthesized by WC method and calcined at 900 °C for 5h.

Note: ↓ La_2O_3 , ◆ LaFeO_3 , ■ LaNiO_3 and ● La_2NiO_4

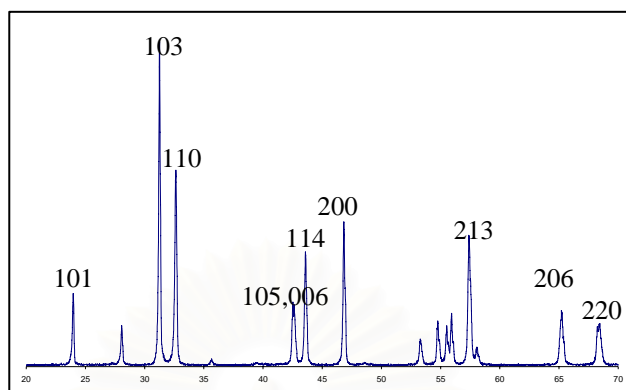


Figure 4.27 Data base of crystal structure La_2NiO_4 from JCPDS: 34-0314.

Table 4.14 Crystal structures and lattice parameters of $\text{La}_2\text{Ni}_{1-x}\text{Fe}_x\text{O}_4$ ($x = 0.0-1.0$) K_2NiF_4 -typed structure, synthesized by WC method and calcined at 900°C for 5h

K_2NiF_4 -typed	Crystal structure	Lattice parameters (\AA)		
		a	b	c
La_2NiO_4	Tetragonal	3.8617	3.8617	12.683
x	Crystal structure	Lattice parameters (\AA)		
		a	b	c
0.1	Tetragonal	3.8732	3.8732	12.6646
0	Tetragonal	3.8658	3.8658	12.6515

To obtain the lattice parameters for each composition in Table 4.14 the 101,103,110,114, 200, 213 reflections were used in the case of the tetragonal phase as labeled in Figure 4.27), which is similar to that of La_2NiO_4 (JCPDS: 34-0314). The lattice constants decrease with the decrease in x of the $\text{La}_2\text{Ni}_{1-x}\text{Fe}_x\text{O}_4$ systems, because the Fe ion radius is larger than that of Ni ion.

Table 4.15 Crystal structures and lattice parameters of $\text{La}_2\text{Ni}_{1-x}\text{Fe}_x\text{O}_4$ ($x = 0.0-1.0$) K_2NiF_4 typed structure, synthesized by MWC method and calcined at 900°C for 5h

K_2NiF_4 -typed	Crystal structure	Lattice parameters (\AA)		
		a	b	c
La_2NiO_4	Tetragonal	3.8617	3.8617	12.683
x	Crystal structure	Lattice parameters (\AA)		
		a	b	c
0.1	Tetragonal	3.8944	3.8944	12.5711
0	Tetragonal	3.8529	3.8529	12.7671

To obtain the lattice parameters for each composition in Table 4.15, the 101,103,110,114,200,213 peaks were used in the case of the tetragonal phase as labeled in Figure 4.27), which is similar to that of La_2NiO_4 (JCPDS: 34-0314). The lattice constants decrease with the decrease in x of the $\text{La}_2\text{Ni}_{1-x}\text{Fe}_x\text{O}_4$ systems, similar to these synthesized by MWC methods.

E. The volume per formula unit of $\text{La}_2\text{Ni}_{1-x}\text{Fe}_x\text{O}_4$

Table 4.19 shows the volume per formula unit of $\text{La}_2\text{Ni}_{1-x}\text{Fe}_x\text{O}_4$ ($x = 0.0-1.0$) K_2NiF_4 typed structure, synthesized by WC and MWC methods and calcined at 900°C for 5h. The volumes of unit cell were calculated from the unit cell parameters from XRD results, and then normalized by the number of formula per unit cell.

Table 4.16 The volume of formula unit of $\text{La}_2\text{Ni}_{1-x}\text{Fe}_x\text{O}_4$ ($x = 0.0-0.1$) K_2NiF_4 -typed structure, synthesized by WC and MWC methods and calcined at 900°C for 5h

x	Volume of formula unit (\AA^3)	
	WC	MWC
0.1	95.00	95.32
0	94.53	94.76

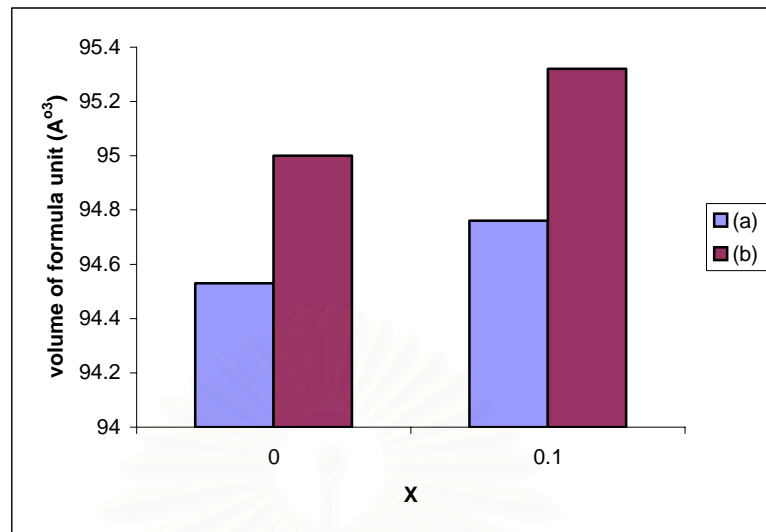


Figure 4.28 The volume of formula unit of $\text{La}_2\text{Ni}_{1-x}\text{Fe}_x\text{O}_4$ ($x = 0.0-1.0$), synthesized by (a) WC (b) MWC and calcined at $900\text{ }^\circ\text{C}$ for 5h.

Similar to the case of lanthanum nickel iron K_2NiF_4 -typed structure, the volume per formula unit increases when Fe content increases.

4.2.2 The comparison of four combustion methods on the synthesis of $\text{L}_2\text{NF-91}$

The selection of $\text{La}_2\text{Ni}_{0.9}\text{Fe}_{0.1}\text{O}_4$ ($\text{L}_2\text{NF-91}$) is significant interest for high-temperature. For SOFC operation high temperature ($900-1000\text{ }^\circ\text{C}$). Tsipis *et al.* [31, 41, 42] was found that the oxygen partial pressure of $\text{La}_2\text{Ni}_{0.9}\text{Fe}_{0.1}\text{O}_4$ is higher than that of La_2NiO_4 at the high temperature of $900-1000\text{ }^\circ\text{C}$. It was selected here to study the effect of the different synthetic methods, including WC, MWC, NC and MNC.

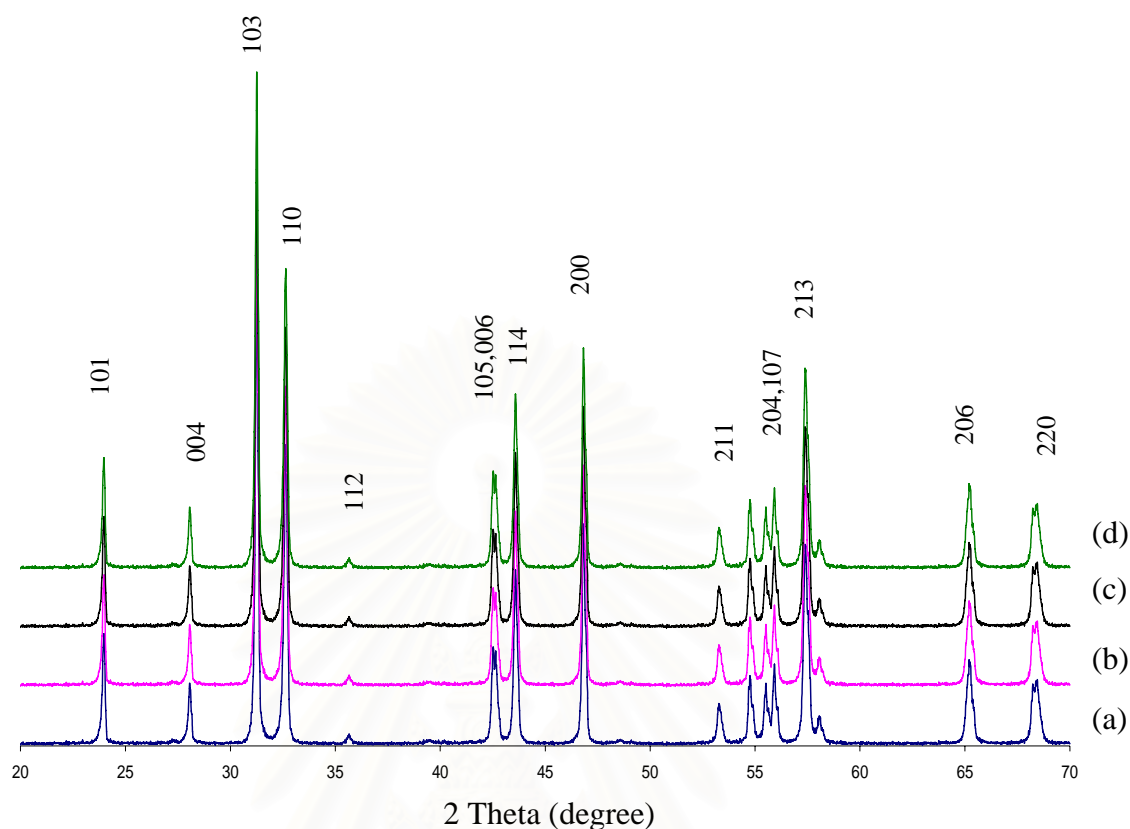


Figure 4.29 XRD patterns of L_2NF-91 , synthesized by four methods (a) WC (b) MWC (c) NC (d) MNC with the calcinations temperature of $1000\text{ }^\circ\text{C}$ for 5h.

As shown in Figure 4.29, the L_2NF-91 samples synthesized by four combustion methods, WC, MWC, NC, and MNC at $1000\text{ }^\circ\text{C}$ for 5h gave the same crystal structure which is the tetragonal with the lattice a, b, and c parameters of 3.8617 \AA , 3.8617 \AA , 12.683 \AA , respectively.

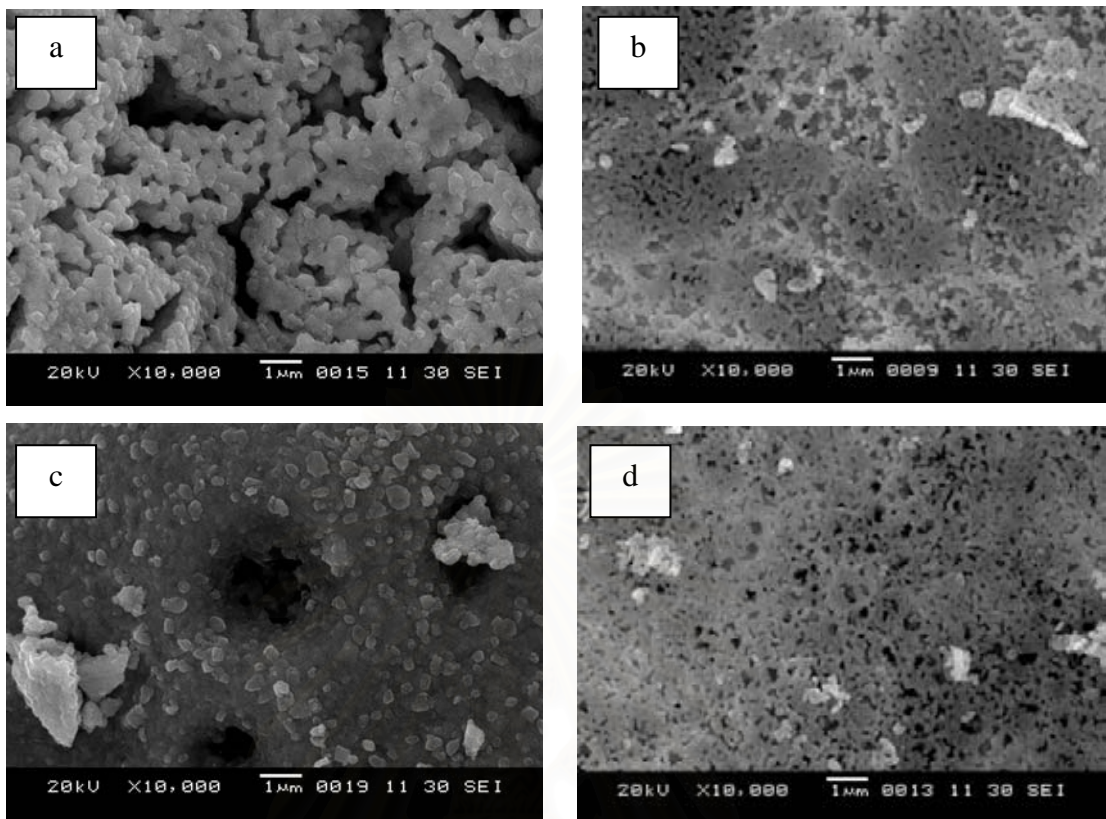


Figure 4.30 SEM pictures of L_2NF-91 with the calcination temperature of $1000\text{ }^\circ\text{C}$ for 5 h (a) WC (b) MWC (c) NC (d) MNC.

Although L_2NF-91 samples, synthesized by four combustion methods, have the same structure, the difference was found in the term of particle size as shown in SEM pictures (Figure 4.30). The particle sizes can be arranged from the smallest to the largest by synthesis using the methods of MNC and MWC ($\sim 0.16\text{ }\mu\text{m}$), NC ($\sim 0.18\text{ }\mu\text{m}$), and WC ($\sim 0.47\text{ }\mu\text{m}$). This arrangement is similar to that of LNF-64 perovskite. Thus, it is confirmed that the particle size of lanthanum nickel oxides depend on the amount of fuel chemicals in the combustion method.

4.2.3 Chemical compatibility with 8-YSZ electrolyte

4.2.3.1 The mixtures of L_2NF-91 powders with 8-YSZ

The chemical compatibility of both stoichiometric and non-stoichiometric L_2NF-91 perovskites was investigated in its mixture with 8-YSZ of 50/50 wt % at room temperature to 1200 °C. The new phase(s) formed by the undesired chemical reaction was followed by XRD and characterized using the JCDPS database.

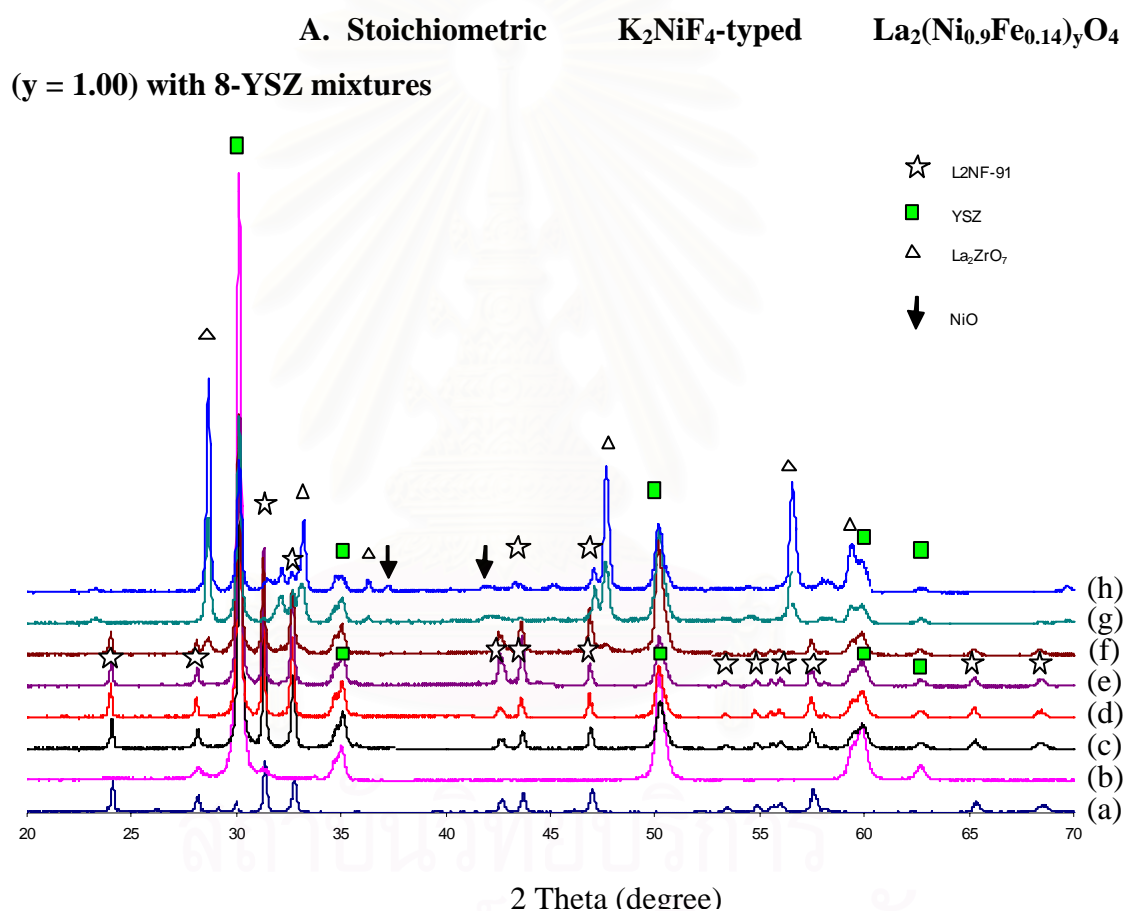


Figure 4.31 XRD patterns of (a) L_2NF-91 ($y = 1.00$), (b) 8-YSZ, and the powder mixtures between L_2NF-91 ($y = 1.00$) and 8-YSZ: (c) the mixtures at room temperature, (d) after calcination at 800°C for 5h, (e) after calcination at 900°C for 5h, (f) after calcination at 1000 °C for 5h, (g) after calcination at 1100 °C for 5h, and (h) after calcination 1200 °C for 5h.

Table 4.17 The presence of undesired phase(s) in the powder mixtures between $\text{La}_2\text{NF-91}$ ($y = 1.00$) and 8-YSZ after calcination at various temperatures for 5h

The calcination temperature (°C)	Synthesis methods	
	WC	MWC
RT	none	none
800	none	none
900	none	none
1000	trace amount $\text{La}_2\text{Zr}_2\text{O}_7$	trace amount $\text{La}_2\text{Zr}_2\text{O}_7$
1100	$\text{La}_2\text{Zr}_2\text{O}_7$ and NiO	$\text{La}_2\text{Zr}_2\text{O}_7$ and NiO
1200	$\text{La}_2\text{Zr}_2\text{O}_7$ and NiO	$\text{La}_2\text{Zr}_2\text{O}_7$ and NiO

$\text{La}_2(\text{Ni}_{0.9}\text{Fe}_{0.1})_y\text{O}_4$ ($y = 1.00$) is designated in this section as $\text{La}_2\text{NF-91}$ ($y = 1.00$). The XRD results show in Figure 4.31, and Table 4.17 summarizes the undesired species found at different calcination temperatures. The patterns at the calcination temperatures of 800-900°C contain the peaks of $\text{La}_2\text{NF-91}$ ($y = 1.00$) and 8-YSZ only, indicating the good chemical compatibility from room temperature up to 900°C. Besides the original components, the new phases of $\text{La}_2\text{Zr}_2\text{O}_7$ (JCDPS: 17-0450) started to form at 1000°C. At 1100 and 1200°C, the $\text{La}_2\text{Zr}_2\text{O}_7$ and NiO (JCPDS: 47-1049) phases were clearly observed and the original components disappeared.

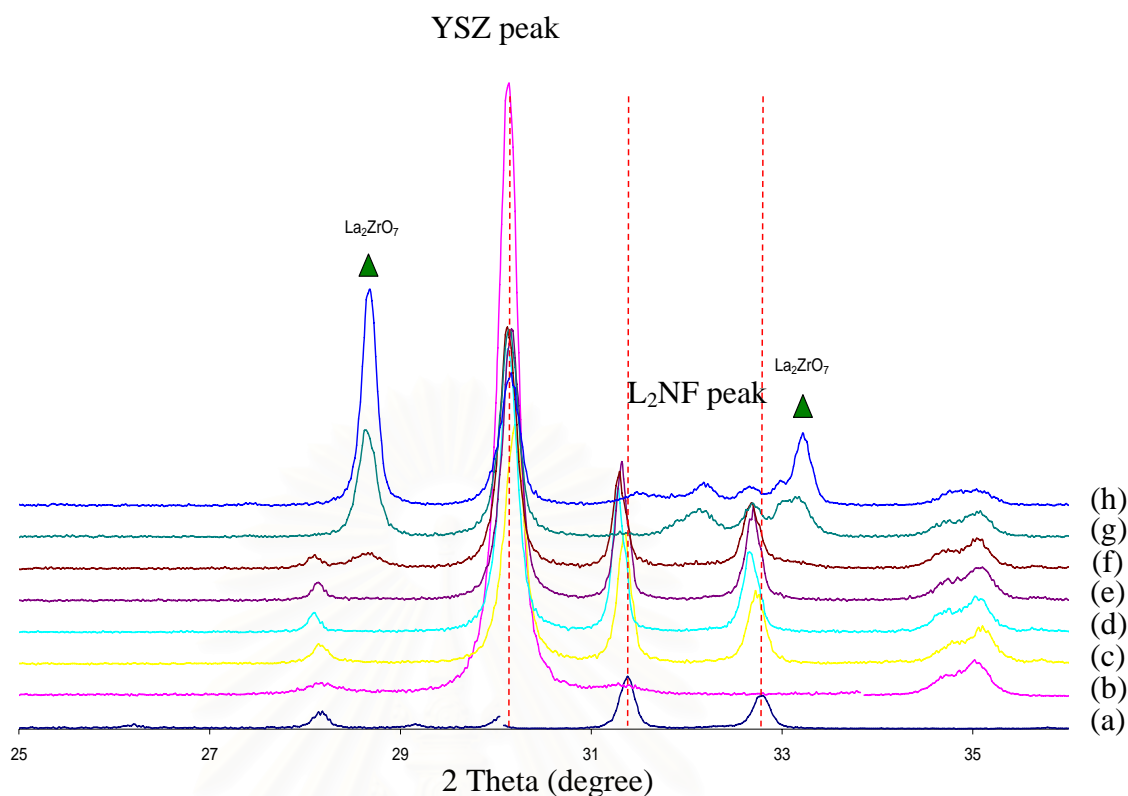


Figure 4.32 XRD patterns between a 2θ range of $25\text{-}36^\circ$ of (a) L₂NF-91 ($y = 1.00$), (b) 8-YSZ, and the powder mixtures between L₂NF-91 ($y = 1.00$) and 8-YSZ: (c) the mixtures before calcination, (d) after calcination at 800°C for 5h, (e) after calcination at 900°C for 5h, (f) after calcination at 1000°C for 5h, (g) after calcination at 1100°C for 5h, and (h) after calcination 1200°C for 5h.

In Figure 4.32, the portion of XRD with a 2θ range of $25\text{-}36^\circ$ was blown up. The shift of the L₂NF peaks to the lower diffraction angle indicates the volume expansion of K₂NiF₄ phase, caused by the dissolution of larger Zr cations into the K₂NiF₄-typed structure [48, 50]. Even though the new phases were not found at lower temperature by XRD, the small amount of Zr may exist in the LNF structure as the impurity atom.

B. Non- stoichiometric K_2NiF_4 -typed $La_2(Ni_{0.9}Fe_{0.14})_yO_4$

($y = 0.95$) with 8-YSZ mixtures

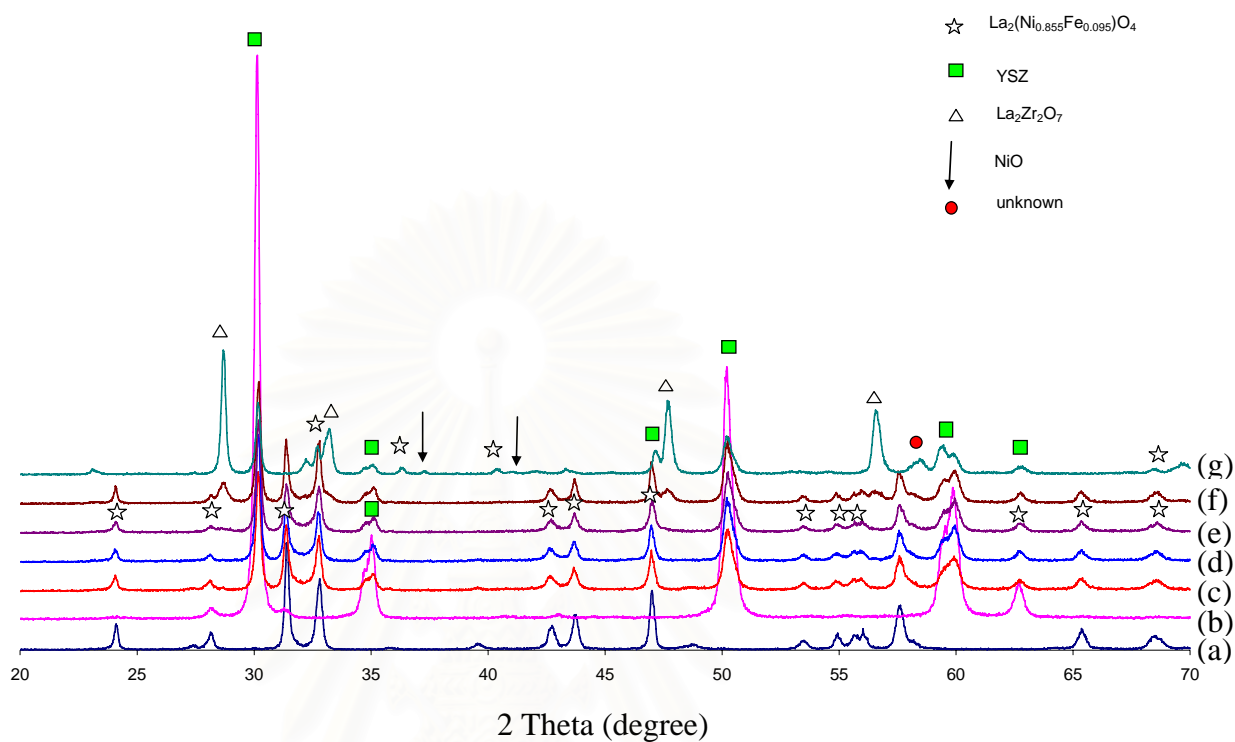


Figure 4.33 XRD patterns of (a) L_2NF-91 ($y = 0.95$), (b) 8-YSZ, and the powder mixtures between L_2NF-91 ($y = 0.95$) and 8-YSZ: (c) the mixtures at room temperature, (d) after calcinations at 800 °C for 5h, (e) after calcinations at 900 °C for 5h, (f) after calcinations at 1000 °C for 5h, and (g) after calcinations at 1100 °C for 5h.

สถาบันวิทยบริการ
จุฬาลงกรณ์มหาวิทยาลัย

Table 4.18 The presence of undesired phase(s) in the powder mixtures between K_2NiF_4 -typed structure L_2NF-91 ($y = 0.95$) and 8-YSZ after calcinations at various temperatures for 5h

The calcinations temperature ($^{\circ}C$)	Synthesis methods	
	MWC	MNC
RT	none	none
800	none	none
900	trace amount $La_2Zr_2O_7$	trace amount $La_2Zr_2O_7$
1000	$La_2Zr_2O_7$ and NiO	$La_2Zr_2O_7$ and NiO
1100	$La_2Zr_2O_7$ and NiO	$La_2Zr_2O_7$ and NiO

$La_2(Ni_{0.9}Fe_{0.1})_yO_4$ ($y = 0.95$) is designated in this section as L_2NF-91 ($y = 0.95$). The XRD results show in Figure 4.33, and Table 4.18 summarizes the undesired specie found at different calcination temperatures. The patterns at the calcination temperatures of $800^{\circ}C$ contains the peaks of L_2NF-91 ($y = 0.95$) and 8-YSZ only, indicating the good chemical compatibility from room temperature to $800^{\circ}C$ only. Besides the original components, the new phases of $La_2Zr_2O_7$ (JCDPS: 17-0450) and NiO (JCPDS: 47-1049) started to form at $900^{\circ}C$. At $1000-1100^{\circ}C$, the $La_2Zr_2O_7$ and NiO phases were clearly observed and the original components disappeared. Moreover, at $1100^{\circ}C$, the found unknown phase with a 2θ range of 58° was detected.

สถาบันวิทยบริการ
จุฬาลงกรณ์มหาวิทยาลัย

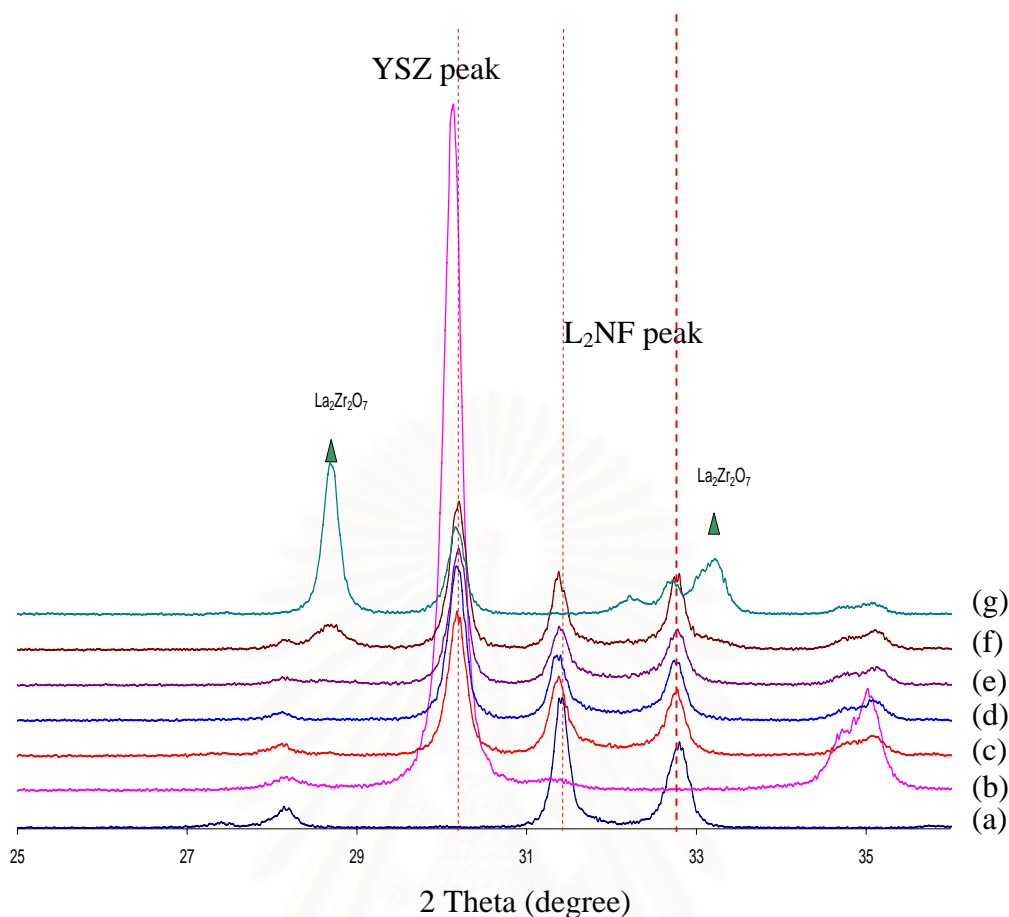


Figure 4.34 XRD patterns between a 2θ range of $25\text{--}36^\circ$ of (a) L_2NF-91 ($y = 0.95$), (b) 8-YSZ, and the powder mixtures between L_2NF-91 ($y = 0.95$) and 8-YSZ: (c) the mixtures at room temperature, (d) after calcination at 800°C for 5h, (e) calcination at 900°C for 5h, (f) calcination at 1000°C for 5h, and (g) calcination at 1100°C for 5h.

The portion of XRD with a 2θ range of $25\text{--}36^\circ$ was blown up in Figure 4.34. The shift of the L_2NF peaks to the lower diffraction angle indicates the volume expansion of K_2NiF_4 phase, caused by the dissolution of larger Zr cations into the K_2NiF_4 -typed structure [48, 50]. Even though the new phases were not found at lower temperature by XRD, the small amount of Zr may exist in the K_2NiF_4 -typed structure as the impurity atom.

C. Non-stoichiometric K_2NiF_4 -typed $La_2(Ni_{0.9}Fe_{0.14})_yO_4$
($y = 1.05$) with -YSZ mixtures

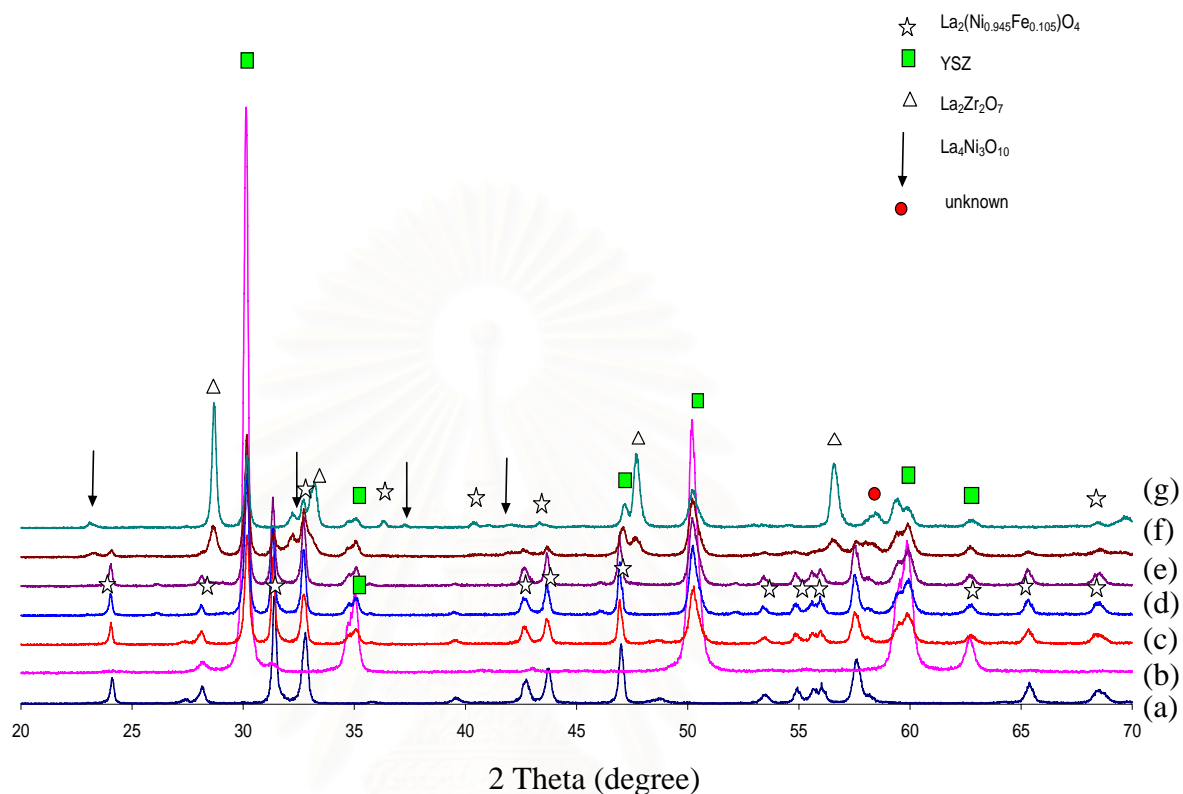


Figure 4.35 XRD patterns of (a) L_2NF-91 ($y = 1.05$), (b) 8-YSZ, and the powder mixtures between L_2NF-91 ($y = 1.05$) and 8-YSZ: (c) the mixtures at the room temperature, (d) after calcination at 800°C for 5h, (e) after calcination at 900°C for 5h, (f) after calcination at 1000 °C for 5h and (g) after calcination at 1100 °C for 5h.

Table 4.19 The presence of undesired phase(s) in the powder mixtures between L₂NF-91 (y = 1.05) and 8-YSZ after calcination at various temperatures for 5h

The calcination temperature (°C)	Synthesis methods	
	MWC	MNC
RT	none	none
800	none	none
900	trace amount La ₂ Zr ₂ O ₇ none	trace amount La ₂ Zr ₂ O ₇
1000	La ₂ Zr ₂ O ₇ and La ₄ Ni ₃ O ₁₀	La ₂ Zr ₂ O ₇ and La ₄ Ni ₃ O ₁₀
1100	La ₂ Zr ₂ O ₇ and La ₄ Ni ₃ O ₁₀	La ₂ Zr ₂ O ₇ and La ₄ Ni ₃ O ₁₀

La₂(Ni_{0.9}Fe_{0.1})_yO₄ (y = 1.05) is designated in this section as LNF-64 (y = 1.05). The XRD results show in Figure 4.35 and Table 4.19 summarizes the undesired specie found at different calcination temperatures. The patterns at the calcination temperatures of 800 °C contains the peaks of L₂NF-91 (y = 1.05) and 8-YSZ only, indicating the good chemical compatibility from room temperature to 800°C only. Besides the original components, the new phases of La₂Zr₂O₇ (JCDPS: 17-0450) and La₄Ni₃O₁₀ (JCDPS: 83-1164) started to form at 900°C. At 1000-1100°C, the La₂Zr₂O₇ and La₄Ni₃O₁₀ phases were clearly observed and the original components disappeared. Moreover, the XRD peak of unidentified phase was found at 58°.

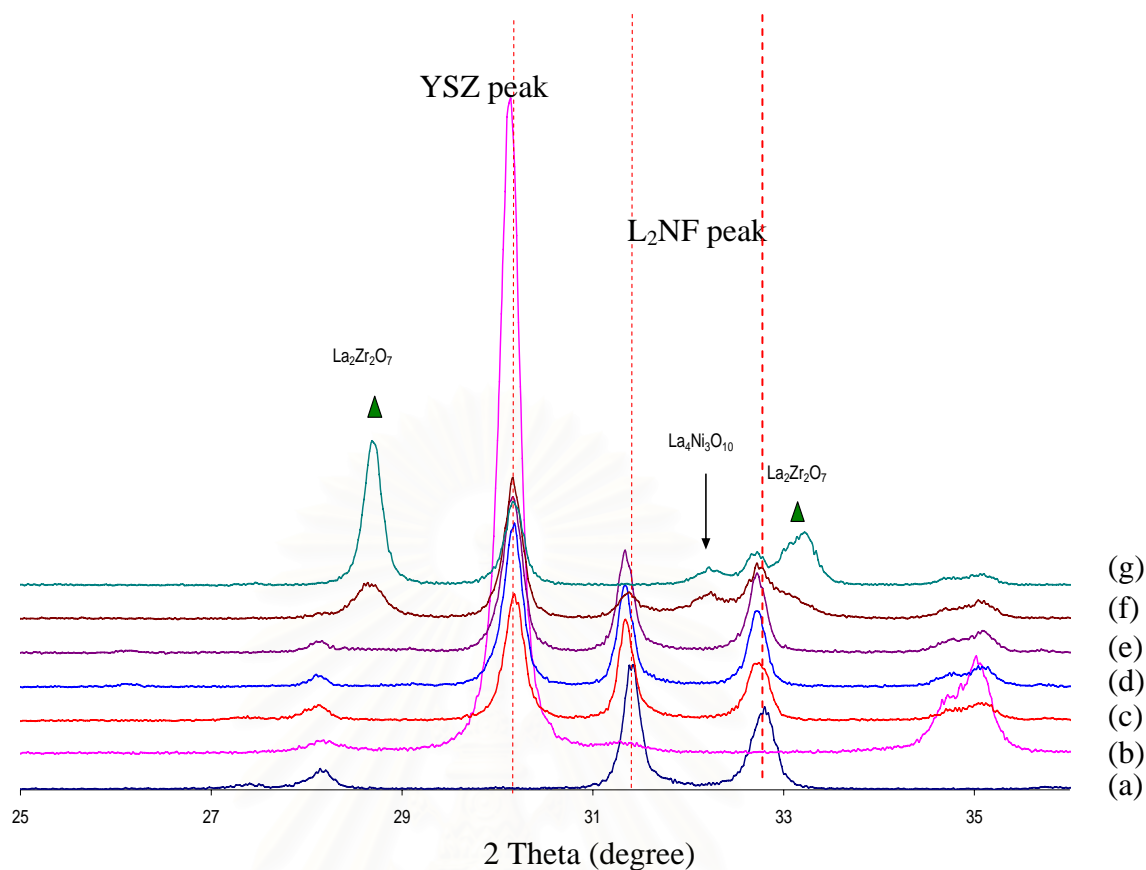
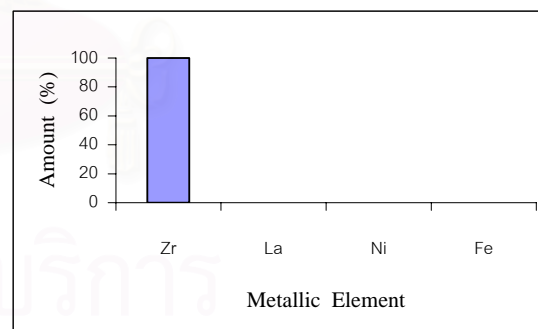
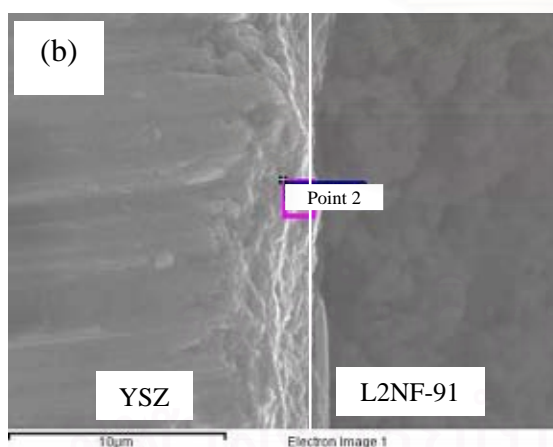
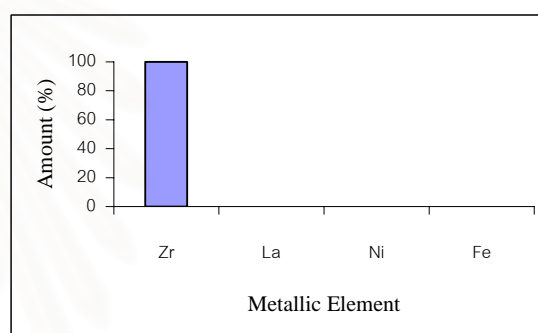
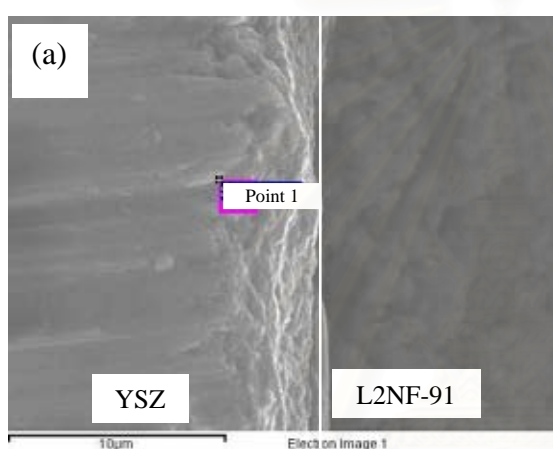


Figure 4.36 XRD patterns between a 2θ range of $25\text{-}36^\circ$ of (a) L₂NF-91 ($y = 1.05$), (b) 8-YSZ, and the powder mixtures between L₂NF-91 ($y = 1.05$) and 8-YSZ: (c) the mixtures at room temperature, (d) after calcination at 800°C for 5h, (e) after calcination at 900°C for 5h, (f) after calcination at 1000°C for 5h, and (g) after calcination at 1100°C for 5h.

The portion of XRD with a 2θ range of $25\text{-}36^\circ$ was blown up in Figure 4.36. The shift of the L₂NF peaks to the lower diffraction angle indicates the volume expansion of K₂NiF₄ phase, caused by the dissolution of larger Zr cations into the K₂NiF₄-typed structure [48, 50]. Even though the new phases were not found at lower temperature by XRD, the small amount of Zr may exist in the K₂NiF₄-typed structure as the impurity atom.

4.2.3.2 The membrane of L₂NF-91 powder with 8-YSZ

To simulate the SOFC configuration, the chemical compatibility was studied at the surface between L₂NF-91 and 8-YSZ. The L₂NF-91 prepared by MNC route was chosen in this study since it has a smallest particle size. The screen-printing technique of L₂NF-91 on 8-YSZ electrolyte pellet. From section 4.1.3.1 A, it was found that the L₂NF-91 can withstand the reaction with 8-YSZ up to 900 °C; therefore, in this section the study was focused on the temperature at 900 °C to observe any change corresponding to the XRD results by studying of cross-sectioned L₂NF-91 and 8-YSZ by SEM Maps (mode-ID-point technique).



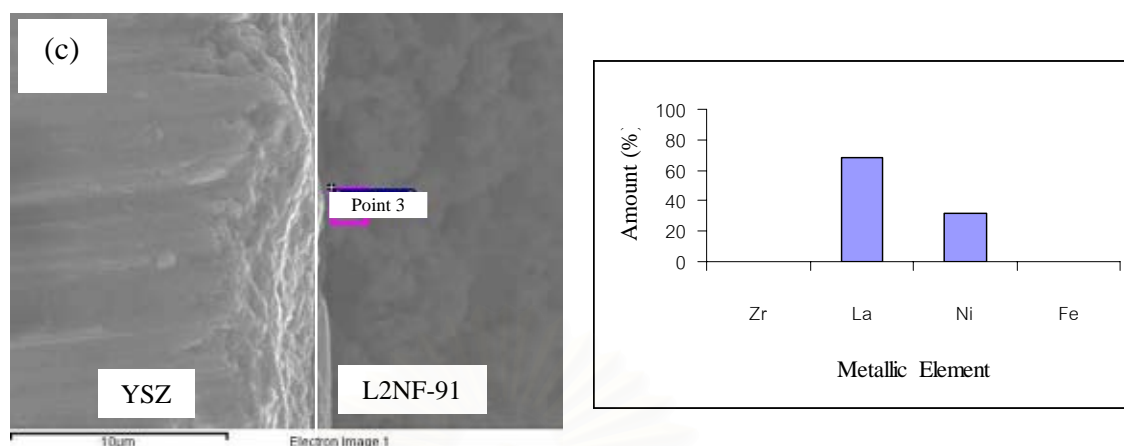


Figure 4.37 SEM-Maps (mode-ID-point technique) of the cross-sectioned L₂NF-91 (MNC method)/8-YSZ pellet after calcination at 900°C for 5 h, detected at (a) point 1, (b) point 2, and (c) point 3.

Table 4.20 The weight percentage of metallic elements of the cross-sectioned L₂NF-91 (MNC method)/8-YSZ pellet after calcination at 900°C for 5 h, summarized by SEM-Maps (ID-point technique)

Metallic Element	Amount (wt %)		
	point 1	point 2	point 3
Zr	100	100	0
La	0	0	68.50
Ni	0	0	31.50
Fe	0	0	0

From Figure 4.37 and table 4.20, there is only Zr as the metallic element at point 1 and 2, both located within the side of 8-YSZ pellet. At point 3, only La, Ni, and Fe were found. This result confirms XRD results in section 4.2.3.1 A that the reaction between L₂NF-91 and 8-YSZ does not occur at 900°C. In order words, the prepared L₂NF-91 was found to have a good chemical compatibility with YSZ at 900°C.

4.2.4 Physical compatibility of L₂NF-91 structure with 8-YSZ electrolyte

The physical compatibility between L₂NF-91 and 8-YSZ was investigated in term of the thermal expansion coefficient (TEC). The closed TEC values of both materials are the requirement in use as the components for SOFC.

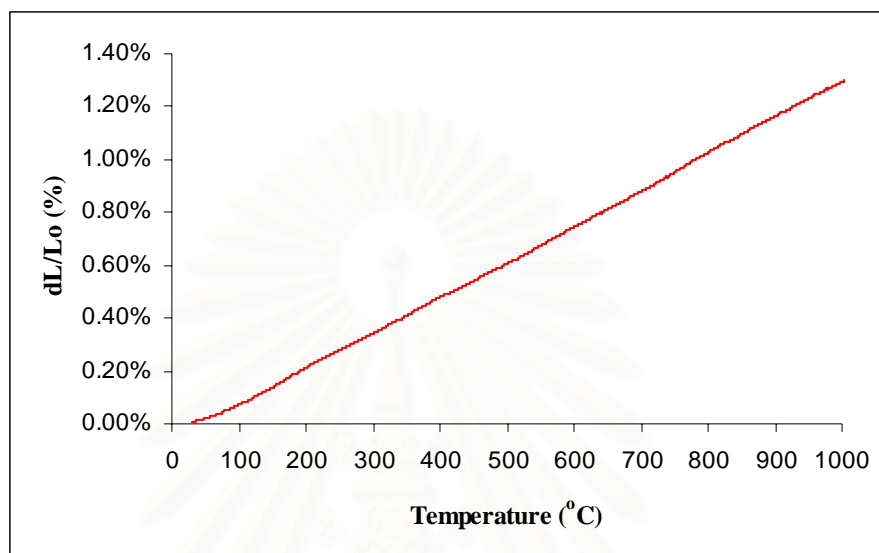


Figure 4.38 Thermal expansion behavior of L₂NF-91 prepared by MNC method.

Figure 4.38 shows the thermal expansion behavior of L₂NF-91, its slope indicates TEC of materials at each temperature. The straight line was obtained for L₂NF-91, indicating the constant TEC values of $12.7 \times 10^{-6} \text{ K}^{-1}$ from room temperature up to 1000 °C.

Table 4.21 The thermal expansion coefficients of L₂NF-91 samples and 8-YSZ at 800 °C

Materials	Synthesis method (s)	TEC ($\times 10^{-6} \text{ K}^{-1}$)
La ₂ Ni _{0.9} Fe _{0.1} O ₄ [in this thesis]	MNC	12.7
^a La ₂ Ni _{0.9} Fe _{0.1} O ₄	Solid state reaction	12.8
^a La ₂ Ni _{0.98} Fe _{0.02} O ₄	Solid state reaction	13.2
^b 8-YSZ	Solid state reaction	10.5

^aBasu et al. [18], ^bSingnal et al. [4]

As shown in Table 4.21, the thermal expansion coefficient of L₂NF-91 is $12.7 \times 10^{-6} \text{ K}^{-1}$, which is the same range with that of 8-YSZ. It could be concluded here that L₂NF-91 has the good physical compatibility with 8-YSZ.

CHAPTER V

CONCLUSION AND SUGGESTION

5.1 Conclusion

A. Perovskite structure

The single phased $\text{LaNi}_{1-x}\text{Fe}_x\text{O}_3$ ($x = 0.0-1.0$) perovskites were synthesized successfully by both WC and MWC methods at 700-900 °C for 5h.

- As x is 0.0-0.5, the crystal structure is cubic at 700°C and becomes rhombohedral at 900 °C. The structures are similar to those of LaNiO_3 .
- As x is 0.6-1.0, the crystal structure is orthorhombic. The structure is similar to that of LaFeO_3 .

The lattice constants and the volume per formula unit in the series generally increase as the Fe content (x of the $\text{LaNi}_{1-x}\text{Fe}_x\text{O}_3$) increases.

LNF-37 ($x = 0.7$) represents LNF perovskites with orthorhombic phase and LNF-64 ($x = 0.4$) represents LNF perovskites with the cubic/rhombohedral phases. The rhombohedral phase can withstand the high temperature up to 1200 °C, whereas the orthorhombic phase decomposes to La_2NiO_4 and La_2O_3 at 1200 °C. In conclusion, the presence of Fe increases the stability of the perovskite structure.

The effect of different combustion methods, WC, MWC, NC and MNC, was investigated using LNF-64 as a representative. All synthesis methods give the products with the same structure of a rhombohedral phase, but with the difference in sizes. The sizes of LNF-64 perovskite arranged from the smallest to the largest are ~0.17 μm by MNC method, ~0.26 μm by MWC method, ~0.35 μm by NC method and ~0.45 μm by WC method.

B. K_2NiF_4 -typed structure

The single phase of K_2NiF_4 -typed $\text{La}_2\text{Ni}_{1-x}\text{Fe}_x\text{O}_4$ (L_2NF) was synthesized successfully only with the composition of $x = 0.0-0.1$ using both WC and MWC methods at 900 °C for 5h. The crystal structure is tetragonal, similar to that of

La_2NiO_4 . With the replace of Fe ions in La_2NiO_4 , the volume per formula unit and the lattice constants increase, similar to what observed in perovskite structures.

The four combustion methods give the products of $\text{La}_2\text{Ni}_{0.9}\text{Fe}_{0.1}\text{O}_4$ with the tetragonal structure, similar to the structure of La_2NiO_4 . The sizes arranged from the smallest to the largest are $\sim 0.16 \mu\text{m}$ by MNC and MWC methods, $\sim 0.18 \mu\text{m}$ by NC method and $\sim 0.47 \mu\text{m}$ by WC method.

C. Chemical compatibility of both structures with 8-YSZ

The chemical compatibility of $\text{La}(\text{Ni}_{0.6}\text{Fe}_{0.4})_y\text{O}_3$ and $\text{La}_2(\text{Ni}_{0.9}\text{Fe}_{0.1})_y\text{O}_4/8\text{-YSZ}$ ($y = 1.00, 0.95, 1.05$) with 8-YSZ, were investigated by XRD at the temperature of 800 to 1200 °C.

- The stoichiometric formula ($y = 1.00$) has the good compatibility with 8-YSZ from room temperature up to 900 °C. The undesired phases of $\text{La}_2\text{Zr}_2\text{O}_7$ and NiO were found at higher temperature.

- The non-stoichiometric formula ($y = 0.95, 1.05$) has the good compatibility with 8-YSZ from room temperature up to 800 °C. The undesired phases of $\text{La}_2\text{Zr}_2\text{O}_7$ and NiO were found at higher temperature.

Although the impurity phase was not found until higher temperature, the dissolution of the small amount of Zr cations into both structures was observed since room temperature.

Investigating by SEM-EDX, the dissolution of metallic elements at the interface of the perovskite or K_2NiF_4 -typed and the 8-YSZ membrane was detected only at the temperature higher than 900 °C.

D. Physical compatibility between both structures with 8-YSZ

The thermal expansion coefficients of LNF-64 and $\text{L}_2\text{NF-91}$ are $13.2 \times 10^{-6} \text{ K}^{-1}$ and $12.7 \times 10^{-6} \text{ K}^{-1}$, respectively. Therefore, these compounds, as candidates of a cathode material, are physically compatible with 8-YSZ electrolyte.

5.2 Suggestion

1. During the fabrication of LNF and L_2NF cathodes on the 8-YSZ electrolyte for SOFC, the high temperature above 900 °C should be avoided because of the undesired chemical reaction occurs.

2. In order to regard the LNF and L_2NF series as the candidates of a cathode material for SOFC, the electronic conductivities must be measured. Fe can increase the thermal stability, but it can decrease the electronic conductivity also. Hence, the optimization of Fe contents on cathode materials based on both the good thermal stability and the high electrical conductivity must be investigated.

3. To study the efficiency of using the LNF and L_2NF series as the cathode in SOFC, the impedance of materials must be investigated using an AC-Impedance spectroscopy.



REFERENCES

- [1] Garrison, E. Solid Oxide Fuel Cells (online). Available from:
<http://www.iit.edu/~smart/garrear/fuelcells.htm>
- [2] Solid oxide fuel cell (online). Available from:
www.mne.eng.psu.ac.th/fuelcell/Sofc2.jpg
- [3] Flat plate solid oxide fuel cells (online). Available from:
http://www.doitpoms.ac.uk/tlplib/fuel-cells/figures/flat_plate_sofc_sml.
- [4] Singnal, S.C, Kendall, K. High temperature solid oxide fuel cells: fundamentals, design and applications (2004): p.1-143.
- [5] Chiba, R.; Yoshimura, F.; Sakurai, Y. An investigation of $\text{LaNi}_{1-x}\text{Fe}_x\text{O}_3$ as a cathode material for solid oxide fuel cells. *Solid State Ionics* 124 (1999): 281-288.
- [6] Zhu, G.; Fang, X.; Xia, C.; Liu, X. Preparation and electrical properties of $\text{La}_{0.4}\text{Sr}_{0.6}\text{Ni}_{0.2}\text{Fe}_{0.8}\text{O}_3$ using a glycine nitrate process. *Ceramics International* 131 (2005): 115–119.
- [7] Hrovat, M.; Katsarakis, N.; Reichmann, K.; Bemik, S.; Kuscer, D.; Hole, J. Characterisation of $\text{LaNi}_{1-x}\text{Co}_x\text{O}_3$ as a possible SOFC cathode material. *Solid State Ionics* 83 (1996): 99-105.
- [8] Mori, M.; Abe, T.; Yamamoto, O.; Takeda, Y.; Kawahara, T. Cubic-stabilized zirconia and alumina compositions as electrolytes in planar type solid oxide fuel cells. *Solid State Ionics* 74 (1994):157-164.
- [9] Suzuki, T.; Awano, M.; Jasinski, P.; Petrovsky, V.; Anderson, H.U. Composite (La,Sr) MnO_3 -YSZ cathode for SOFC, *Solid State Ionics* 177 (2006): 2071–2074.
- [10] Kharton, V.V.; Viskup, A.P.; Kovalevsky, A.V.; Naumovich, E.N.; Marques, F.M.B. Ionic transport in oxygen-hyperstoichiometric phases with K_2NiF_4 -type structure. *Solid State Ionics* 143 (2001): 337–353.
- [11] Munnings, C.N.; Skinner, S.J.; Amow, G.; Whifield, P.S.; Davidson, I.J. Structure, stability and electrical properties of the $\text{La}_{(2-x)}\text{Sr}_x\text{MnO}_{4\pm\delta}$ solid solution series. *Solid State Ionics* 177 (2006): 1849-1853.
- [12] Bevilacqua, M.; Montini, T.; Tavagnacco, C.; Vicario, G.; Fornasiero, P.; Graziani, M. Influence of synthesis route on morphology and electrical properties of $\text{LaNi}_{0.6}\text{Fe}_{0.4}\text{O}_3$. *Solid State Ionics* 177 (2006): 2957-2965.

- [13] Sahu, A.K.; Ghosh, A.; Suri, A.K.; Sengupta, P.; Bhanumurthy, K. Studies on chemical compatibility of lanthanum strontium manganite with yttria-stabilized zirconia. *Materials Letters* 58 (2004): 332–3336.
- [14] Falcon, H.; Goeta, A.E.; Punte, G.; Carbonio, R.E. Crystal structure refinement and Stability of $\text{LaFe}_x\text{Ni}_{1-x}\text{O}_3$ solid solutions. *Journal of solid state chemistry* 133 (1997): 379-385.
- [15] Provendier, H.; Petit, C.; Estournes, C.; Libs, S.; Kiennemann, A. *Applied Catalysis A : General* 180 (1999): 163-173.
- [16] Bontempi, E.; Garzella, C.; Valetti, S.; Depero, L.E. Structural study of $\text{LaNi}_x\text{Fe}_{1-x}\text{O}_3$ prepared from precursor salts. *Journal of the European Ceramic Society* 23 (2003): 2135-2142.
- [17] Chiba, R.; Yoshimura, F.; Sakurai, Y.; Tabata, Y.; Arakawa, M. A study of cathode materials for intermediate temperature SOFCs prepared by the sol-gel method. *Solid State Ionics* 175 (2004): 23–27.
- [18] Basu, R.N.; Tietz, F.; Wessel, E.; Buchkremer, H.P.; Stover, D. Microstructure and electrical conductivity of $\text{LaNi}_{0.6}\text{Fe}_{0.4}\text{O}_3$ prepared by combustion synthesis routes. *Materials Research Bulletin* 391(2004): 335–1345.
- [19] Zhen, Y.D.; Tok, A.I.Y.; Jiang, S.P.; Boey, F.Y.C. $\text{La}(\text{Ni},\text{Fe})\text{O}_3$ as a cathode material with high tolerance to chromium poisoning for solid oxide fuel cells. *Journal of Power Sources* 170 (2007): 61–66.
- [20] Proskurnina, N.V.; Voronin, V.I.; Cherepanov, V.A.; Kiselev, E.A. Phase equilibria and crystal structure of the solid solution $\text{LaFe}_{1-x}\text{Ni}_x\text{O}_3$. *Solid State Chemistry* 35 (2007): 233-239.
- [21] Knudsen, J.; Friehling, P.B.; Bonanos, N. Effect of A-site stoichiometry on phase stability and electrical conductivity of the perovskite $\text{La}_s(\text{Ni}_{0.59}\text{Fe}_{0.41}\text{O}_{3-\delta})$ and its compatibility with $(\text{La}_{0.85}\text{Sr}_{0.15})_{0.91}\text{MnO}_{3-\delta}$ and $\text{Zr}_{0.85}\text{Y}_{0.15}\text{O}_{2.925}$. *Solid State Ionics* 176 (2005): 1563–1569.
- [22] Kharton, V.V.; Viskup, A.P.; Naumovich, E.N.; Tikhonovich, V.N. Oxygen permeability of $\text{LaFe}_{1-x}\text{Ni}_x\text{O}_{3-\delta}$ solid solutions. *Materials Research Bulletin* 134 (1999):1311-1317.
- [23] Komatsu, T.; Chiba, R.; Arai, H.; Sato, K. Chemical compatibility and electrochemical property of intermediate-temperature SOFC cathodes under Cr poisoning condition. *Journal of Power Sources* 176 (2008): 132-137.

- [24] Fontaine, M.L.; Robert, C.L.; Barnab, A.; Ansart, F.; Tailhades, P. Synthesis of $\text{La}_{2-x}\text{NiO}_{4+\delta}$ oxides by polymeric route: non-stoichiometry control. *Ceramics International* 130 (2004): 2087–2098.
- [25] Fujihara, S.; Nakata, T.; Kozuka, H.; Yoko, T. The Effects of Substitution of Alkaline Earths or Y for La on Structure and Electrical Properties of LaSrFeO_4 . *Journal of solid state chemistry* 155 (1995): 456-463.
- [26] Daroukh, M.A.; Vashook, V.V.; Ullmann, H.; Tietz, F.; Raj, I.A. Oxides of the AMO_3 and A_2MO_4 -type: structural stability, electrical conductivity and thermal expansion. *Solid State Ionics* 158 (2003): 141-150.
- [27] Wang, Y.; Nie, H.; Wang, S.; Wen, T.L.; Guth, U.; Valshook, V. $\text{A}_{2-a}\text{A}_a\text{BO}_4$ type oxides as cathode materials for IT-SOFCs ($\text{A} = \text{Pr}, \text{Sm}$; $\text{A} = \text{Sr}$; $\text{B} = \text{Fe}; \text{Co}$). *Materials Letters* 60 (2006): 1174-1178.
- [28] Kharton, V.V.; Yaremchenko, A.A.; Shaula, A.L.; Patrakeev, M.V.; Naumovich, E.N.; Logvinovich, D.I.; Frade, J.R.; Marques, F.M.B. Transport properties and stability of Ni-containing mixed conductors with perovskite- and K_2NiF_4 -type structure. *Journal of Solid State Chemistry* 177 (2004): 26-37.
- [29] Jennings, A.J.; Shaw, C.K.M.; Skinner, S.J. Electrical conductivity of $\text{La}_x\text{Sr}_{2-x}\text{Fe}_{1-y}\text{Ru}_y\text{O}_{4\pm\delta}$. *Materials Chemistry and Physics* 89 (2005): 354-358.
- [30] Fontaine, M.L.; Robert, C.L.; Ansart, P.; Tailhades, P. Composition and porosity graded $\text{La}_{2-x}\text{NiO}_{4+\alpha}$ ($x \geq 0$) interlayers for SOFC: Control of the microstructure via a sol–gel process. *Journal of Power Sources* 156 (2006): 33–38.
- [31] Li, C.; Hu, T.; Zhang, H.; Chen, Y.; Jin, J.; Yang, N. Preparation and characterization of supported dense oxygen permeating membrane of mixed conductor $\text{La}_2\text{NiO}_{4\pm\delta}$. *Journal of Membrane Science* 22 (2003): 1–7.
- [32] Escudero, M.J.; Aguadero, A.; Alonso, J.A.; Daza, L. A kinetic study of oxygen reduction reaction on La_2NiO_4 cathodes by means of impedance spectroscopy. *Journal of Electroanalytical Chemistry* 611 (2007): 107-116.

- [33] Kharton, V.V., Tsipis, E.V.; Yaremchenko, A.A.; Frade, J.R. Surface-limited oxygen transport and electrode properties of $\text{La}_2\text{Ni}_{0.8}\text{Cu}_{0.2}\text{O}_{4+\delta}$. *Solid State Ionics* 166 (2004): 327–337.
- [34] Naumovich, E.N.; Patrakeevev, M.V.; Kharton, V.V.; Yaremchenko, A.A.; Logvinovich, D.I.L.; Marques, F.M.B. Oxygen nonstoichiometry in $\text{La}_2\text{Ni}(\text{M})\text{O}_{4+\delta}$ (M = Cu,Co) under oxidizing conditions. *Solid State Sciences* 7 (2005): 1353–1362.
- [35] Kilner, J.A.; Shaw, C.K.M. Mass transport in $\text{La}_2\text{Ni}_{1-x}\text{Co}_x\text{O}_{4+\delta}$ oxides with the K_2NiF_4 structure. *Solid State Ionics* 154 (2002): 523–527.
- [36] Amow, G.; Whitfield, P.S.; Davidson, I.; Hammond, R.; Munnings, C.; Skinner, S. Structural and sintering characteristics of the $\text{La}_2\text{Ni}_{1-x}\text{Co}_x\text{O}_{4+\delta}$ series. *Ceramics International* 130 (2004): 1635–1639.
- [37] Munnings, C.N.; Skinner, S.J.; Amow, G.; Whitfield, P.S.; Davidson, I.J. Oxygen transport in the $\text{La}_2\text{Ni}_{1-x}\text{Co}_x\text{O}_{4+\delta}$ system. *Solid State Ionics* 176 (2005): 1895–1901.
- [38] Patrakeevev, M.V.; Naumovich, E.N.; Kharton, V.V.; Yaremchenko, A.A.; Tsipis, E.V.; Nunez, P.; Frade, J.R. Oxygen nonstoichiometry and electron-hole transport in $\text{La}_2\text{Ni}_{0.9}\text{Co}_{0.1}\text{O}_{4+\delta}$. *Solid State Ionics* 176 (2005): 179–188.
- [39] Skinner, S.J.; Kilner, J.A. Oxygen diffusion and surface exchange in $\text{La}_{2-x}\text{Sr}_x\text{NiO}_{4+\delta}$. *Solid State Ionics* 135 (2000): 709–712.
- [40] Zhao, F.; Wang, X.; Wang, Z.; Peng, R.; Xia, C. K_2NiF_4 type $\text{La}_2\text{Sr}_x\text{Co}_{0.8}\text{Ni}_{0.2}\text{O}_{4+\delta}$ as the cathodes for solid oxide fuel cells. *Solid State Ionic* (2007):1-4.
- [41] Li, C.; Yu, G.; Yang, N. Supported dense oxygen permeating membrane of mixed conductor $\text{La}_2\text{Ni}_{0.8}\text{Fe}_{0.2}\text{O}_{4+\delta}$ Prepared by sol/gel method, *Separation and Purification Technology* 32 (2003): 335-339.
- [42] Tsipis, E.V.; Naumovich, E.N.; Patrakeevev, M.V.; Waerenborgh, J.C.; Pivak, Y.V.; Gaczynski, P.; Kharton, V.V. Oxygen nonstoichiometry and defect thermodynamics in $\text{La}_2\text{Ni}_{0.9}\text{Fe}_{0.1}\text{O}_{4+\delta}$. *Journal of Physics and Chemistry of Solids* 68 (2007): 1443-1455.

- [43] Tsipis, E.V.; Naumovich, E.N.; Shaula, A.L.; Patrakeev, M.V.; Waerenborgh, J.C.; Kharton, V.V. Oxygen nonstoichiometry and ionic transport in $\text{La}_2\text{Ni}(\text{Fe})\text{O}_{4+\delta}$. *Solid State Ionics* 179 (2008): 57-60.
- [44] Amow, G.; Davidson, I.J., Skinner, S.J. A comparative study of the Ruddlesden-Poppers series, $\text{La}_{n+1}\text{Ni}_n\text{O}_{3n+1}$ ($n=1, 2$ and 3), for Solid Oxide Fuel cell cathode applications *Solid State Ionics* 177 (2006): 1205-1210.
- [45] Lee, H.Y.; Oh, S.M. Origin of cathodic degradation and new phase formation at the $\text{La}_{0.9}\text{Sr}_{0.1}\text{MnO}_3/\text{YSZ}$ interface. *Solid State Ionics* 90 (1996): 133-140.
- [46] Kindermann, L.; Das, D.; Nickel, H.; Hilpert, K. Chemical compatibility of the LaFeO_3 base perovskites $(\text{La}_{0.6}\text{Sr}_{0.4})_Z\text{Fe}_{0.8}\text{M}_{0.2}\text{O}_3$ ($Z=1, 0.9$; $M = \text{Cr, Mn, Co, Ni}$) with yttria stabilized zirconia. *Solid State Ionics* 89 (1996): 215-220.
- [47] Matsuzaki, Y.; Yasuda, I. Relationship between the steady-state polarization of the SOFC air electrode, $\text{La}_{0.6}\text{Sr}_{0.4}\text{MnO}_{3+\delta}/\text{YSZ}$, and its complex impedance measured at the equilibrium potential. *Solid State Ionics* 126 (1999): 307-313.
- [48] Kostogloudis, G.C.; Tsiniarakis, G.; Ftikos, C. Chemical reactivity of perovskite oxide SOFC cathodes and yttria stabilized zirconia. *Solid State Ionics* 135 (2000): 529-535.
- [49] Simner, S.P.; Shelton, J.P.; Anderson, M.D.; Stevenson, J.W. Interaction between $\text{La}(\text{Sr})\text{FeO}_3$ SOFC cathode and YSZ electrolyte. *Solid State Ionics* 161 (2003): 11-18.
- [50] Orui, H.; Watanabe, K.; Arakawa, M. Application of $\text{LaNi}(\text{Fe})\text{O}_3$ as air electrode of solid oxide fuel cell. *Electrochemistry Society* 151 (2004): A1412-A1417.
- [51] Anderson, M.D.; Stevenson, J.W.; Simner, S.P. Reactivity of lanthanide ferrite SOFC cathodes with YSZ electrolyte. *Journal of Power Sources* 129 (2004): 188-192.
- [52] Arakawa, M.; Chiba, R.; Kato, N.; Sakurai, Y.; Hirai, T.; Yamada, I.; New anode and cathode materials for highly efficient SOFCs. MRS Spring Meeting Abstracts, San Francisco, California, April 5-9, *The Electrochemical Society* (1999): p.447.

- [53] Basu, R.N.; Tietz, F.; Wessel, E.; Stover, D. Interface reactions during co-firing of solid oxide fuel cell components. *Journal of Materials Processing Technology* 147 (2004): 85–89.
- [54] Ji, Y.; Kilner, J.A.; Carolan, M.F. Electrical properties and oxygen diffusion in yttria-stabilised zirconia (YSZ)- $\text{La}_{0.8}\text{Sr}_{0.2}\text{MnO}_3$ (LSM) composites. *Solid State Ionics* 176 (2005): 937–943.
- [55] Smith, J.R.; Wachsman, E.D.; Effect of harsh anneals on the LSM/YSZ interfacial impedance profile. *Electrochemical Acta* 51 (2006): 1585–1591.
- [56] Li, C.; Soh, K.C.K.; Wu, P. Formability of ABO_3 perovskites. *Journal of Alloys and Compounds* 372 (2004): 40–48.
- [57] Feng, F.M.; Jiang, L.Q.; Zhu, M.; Liu, H.B.; Zhou, X.; Li, C.H. Formability of ABO_3 cubic perovskites. *Journal of Physics and Chemistry of Solids* (2007).
- [58] Song, H.S.; Kim, W.H.; Hyun, S.H.; Moon, J.; Kim J.; Lee, H.W. Effect of Starting particulate materials on microstructure and cathodic performance of nanoporous LSM–YSZ composite cathodes. *Journal of Power Sources* 167 (2007): 258–264.
- [59] Brant, M.C.; Matencio, T.; Dessemond, L.; Domingues, R.Z. Electrical degradation of porous and dense LSM/YSZ interface. *Solid State Ionics* 177 (2006): 915–921.
- [60] Kim, W.H.; Song, H.S.; Moon, J.; Lee, H.W. Intermediate temperature solid oxide fuel cell using $(\text{La}, \text{Sr})(\text{Co}, \text{Fe})\text{O}_{3-\delta}$ -based cathodes. *Solid State Ionics* 177 (2006): 3211–3216.
- [61] The structure of crystalline solids (online). Available from: www.eng.pyo.nu.ac.th/adcharawadeek/En.Materials/Lesson%201-4/The%20Structure%20of%20Crystalline%20Solids.pdf
- [62] Zahid, M.; Raj, I.A.; Tietz, F. Stover, D. Chemical and physical properties of complex perovskites in the $\text{La}_{0.8}\text{Sr}_{0.2}\text{MnO}_{3-\delta}$ – $\text{La}_{0.8}\text{Sr}_{0.2}\text{CuO}_{2.4+\delta}$ – $\text{La}_{0.8}\text{Sr}_{0.2}\text{FeO}_{3+\delta}$. *Solid State Sciences* 9 (2007): 706–712.
- [63] Zhao, F.; Peng, R.; Xia, C. $\text{La}_{0.6}\text{Sr}_{0.4}\text{MnO}_{3-\delta}$ -based electrode with high durability for intermediate temperature solid oxide fuel cells. *Materials Research Bulletin* 43 (2008): 370–376.

- [64] Piao, J.; Sun, K.; Zhang, N.; Xu, S. A study of process parameters of LSM and LSM–YSZ composite cathode films prepared by screen-printing. *Journal of Power Sources* 175 (2008): 288–295.
- [65] Wincewicz, K.C.; Cooper, J.S. Taxonomies of SOFC material and manufacturing alternatives. *Journal of Power Sources* 140 (2005): 280–296.
- [66] Kharton, V.V.; Yaremchenko, A.A.; Kovalevsky, A.V.; Viskup, A.P.; Naumovich, E.N.; Kerko P.F. Perovskite-type oxides for high-temperature oxygen separation membranes. *Journal of Membrane Science* 163 (1999): 307–317.
- [67] Kawada, T.; Sakai, N.; Yokokawa, H.; Dokiya, M. Reaction between solid oxide fuel cell. *Solid State Ionics* 50 (1992): 189-196.
- [68] Tsai, T.; Barnett S.A. Effect of LSM-YSZ cathode on thin-electrolyte solid oxide fuel cell performance. *Solid State Ionics* 93 (1997): 207-217.
- [69] Thermal expansion (online). Available from:
<http://hyperphysics.phy-astr.gsu.edu/Hbase/thermo/thexp.html>
- [70] Kim, J.D.; Kim, G.D.; Moon, J.W.; Park, Y.; Lee, W.H.; Kobayashi, K.; Nagai, M.; Kim, C.E. Characterization of LSM–YSZ composite electrode by AC impedance spectroscopy. *Solid State Ionics* 143 (2001): 379–389.
- [71] Tai, L.W.; Nasrallah, M.M.; Anderson, H.U.; Sparlin D.M.; Sehlin, S.R. Structure and electrical properties of $\text{La}_{1-x}\text{Sr}_x\text{Co}_{1-y}\text{Fe}_y\text{O}_3$ Part 2. The system $\text{La}_{1-x}\text{Sr}_x\text{Co}_{0.2}\text{Fe}_{0.8}\text{O}_3$. *Solid State Ionics* 76 (1995): 273-283.
- [72] Yang, K.; Shen, J.H.; Yang, H.Y.; Hung, I.M.; Fungb, H.Z.; Wang, H.C. Characterization of the yttria-stabilized zirconia thin film electrophoretic deposited on $\text{La}_{0.8}\text{Sr}_{0.2}\text{MnO}_3$ substrate. *Journal of Alloys and Compounds* 436 (2007): 351–357.
- [73] Orui, H.; Chiba Reiichi, Arakawa, M. Electrochemical performance and microstructure of the LNF-SDC composite cathode for SOFC (2006).
- [74] Xin, X.; Lu, Z.; Huang, X.; Sha, X.; Zhang, Y.; Chen, K.; Ai, N.; Zhu, R.; Su, W. *Journal of Power Sources* 160 (2006): 1221–1224.
- [75] Patel, R.; Simon, C.; Weller, M.T. LnSrScO_4 (Ln = La, Ce, Pr, Nd and Sm) systems and structure correlations for A_2BO_4 (K_2NiF_4) structure types. *Journal of Solid State Chemistry* 180 (2007): 349–359.

- [76] Park, H.J.; Choi, G.M. Oxygen permeation characteristics of zirconia with surface modification. *Solid State Ionics* 177 (2006): 2261–2267.
- [77] Sintering of a powder compact (online). Available from:
<http://www.teachnet.ie/dkeenahan/page21.html>
- [78] Srdic, V.V.; Omorjan, R.P.; Seydel, J. Electrochemical performances of (La,Sr)CoO₃ cathode for zirconia-based solid oxide fuel cells. *Journal Materials Science and Engineering B*116 (2005): 119–124.
- [79] Nie, H.W.; Wen, T.L.; Wang, S.R.; Wang, Y.S.; Guth, U.; Vashook, V. Preparation, thermal expansion, chemical compatibility, electrical conductivity and polarization of A_{2-α}A'_αMO₄ (A = Pr, Sm; A' = Sr; M = Mn, Ni; α = 0.3, 0.6) as a new cathode for SOFC. *Solid State Ionics* 177 (2006): 1929–1932.
- [80] Kharton, V.V.; Kovalevsky, A.V.; Avdeev, M.; Tsipis, E.V.; Patrakeevev, M.V.; Yaremchenko, A.A.; Naumovich, E.N.; Frade, J.R. Chemically induced expansion of La₂NiO_{4+δ}-based materials. *Chemistry of materials* 19 (2007): 2027-2033.
- [81] Xiong, Z.X.; Ji, G.L.; Fang, X. Simulation of grain growth for ABO₃ type ceramics. *Materials Science and Engineering B*99 (2003): 541-548.
- [82] Perovskite structure (online). Available from:
<http://super.gsnu.ac.kr/lecture/inorganic/perovskite.html>



APPENDICES

สถาบันวิทยบริการ
จุฬาลงกรณ์มหาวิทยาลัย

APPENDIX A

The calculations for synthesis by the combustion method

The molecular weights of starting materials

Chemicals	Molecular weight
$\text{La}(\text{NO}_3)_2 \cdot 6\text{H}_2\text{O}$	433.02
$\text{Ni}(\text{NO}_3)_2 \cdot 6\text{H}_2\text{O}$	290.81
$\text{Fe}(\text{NO}_3)_3 \cdot 6\text{H}_2\text{O}$	404.00
Citric acid	192.43

1. Perovskite structure

Example Preparation of 0.0025 mole $\text{LaNi}_{0.6}\text{Fe}_{0.4}\text{O}_{3-\delta}$ (LNF-64)

$\text{La}(\text{NO}_3)_2 \cdot 6\text{H}_2\text{O}$

$$\begin{aligned}
 \text{LNF-64 with 1 mole, La} &= 1 \text{ mole} \\
 \text{LNF-64 0.025 mole, La} &= \frac{0.0025 \text{ mole} \times 1 \text{ mole}}{1 \text{ mole}} \\
 &= 0.0025 \text{ mole} \\
 \text{g} &= n \times \text{MW} \\
 &= 0.0025 \times 433.02 \\
 &= 1.0826 \text{ g}
 \end{aligned}$$

$\text{Ni}(\text{NO}_3)_2 \cdot 6\text{H}_2\text{O}$

$$\begin{aligned}
 \text{LNF-64 with 1 mole, La} &= 0.6 \text{ mole} \\
 \text{LNF-64 0.025 mole, La} &= \frac{0.0025 \text{ mole} \times 0.6 \text{ mole}}{1 \text{ mole}} \\
 &= 0.00150 \text{ mole} \\
 \text{g} &= n \times \text{MW} \\
 &= 0.00150 \times 290.81 \\
 &= 0.43621 \text{ g}
 \end{aligned}$$

$\text{Fe}(\text{NO}_3)_3 \cdot 6\text{H}_2\text{O}$

$$\begin{aligned}
 \text{LNF-64 with 1 mole, La} &= 0.4 \text{ mole} \\
 \text{LNF-64 0.025 mole, La} &= \frac{0.0025 \text{ mole} \times 0.4 \text{ mole}}{1 \text{ mole}} \\
 &= 0.0010 \text{ mole}
 \end{aligned}$$

$$\begin{aligned}
 \text{g} &= n \times \text{MW} \\
 &= 0.0010 \times 404 \\
 &= 0.404 \text{ g}
 \end{aligned}$$

Citric acid

General formula of perovskite is ABO_3 , LNF-64 based on 0.0025 mole

To form the complex, moles of metal : moles of citric acid = 1:2

$$\begin{aligned}
 \text{Moles of (A+B)} &= (0.00025+0.0025) \text{ moles} \\
 \text{Moles of citric acid} &= 2 \times \text{moles of (A+B)} \\
 &= 2 \times 0.005 \\
 \text{Weight of citric acid} &= n \times \text{MW} \\
 &= 0.01 \text{ mole} \times 192.43 \text{ g/mole} \\
 &= 1.9243 \text{ g}
 \end{aligned}$$

2. K_2NiF_4 -typed structure

Example Preparation of 0.0025 mole $\text{La}_2\text{Ni}_{0.6}\text{Fe}_{0.4}\text{O}_{3-\delta}$ (LNF-64)

$\text{La}(\text{NO}_3)_2 \cdot 6\text{H}_2\text{O}$

$\text{La}_2\text{Ni}_{0.6}\text{Fe}_{0.4}\text{O}_{3-\delta}$ ($\text{L}_2\text{NF-64}$) based on 0.0025 mole

$\text{La}(\text{NO}_3)_2 \cdot 6\text{H}_2\text{O}$

$$\begin{aligned}
 \text{L}_2\text{NF-64 with 1 mole, La} &= 2 \text{ mole} \\
 \text{L}_2\text{NF-64 0.025 mole, La} &= \frac{0.0025 \text{ mole} \times 2 \text{ mole}}{1 \text{ mole}} \\
 &= 5 \times 10^{-3} \text{ mole} \\
 \text{g} &= n \times \text{MW} \\
 &= 5 \times 10^{-3} \times 433.02 \\
 &= 2.1651 \text{ g}
 \end{aligned}$$

$\text{Ni}(\text{NO}_3)_2 \cdot 6\text{H}_2\text{O}$

$$\begin{aligned}
 \text{L}_2\text{NF-64 with 1 mole, La} &= 0.6 \text{ mole} \\
 \text{L}_2\text{NF-64 0.025 mole, La} &= \frac{0.0025 \text{ mole} \times 0.6 \text{ mole}}{1 \text{ mole}} \\
 &= 1.5 \times 10^{-3} \text{ mole} \\
 \text{g} &= n \times \text{MW} \\
 &= 0.00150 \times 290.81 \\
 &= 0.43621 \text{ g}
 \end{aligned}$$

Fe(NO₃)₃·6H₂O

$$\begin{aligned}
 \text{L}_2\text{NF-64 with 1 mole, La} &= 0.4 \text{ mole} \\
 \text{L}_2\text{NF-64 0.025 mole, La} &= \frac{0.0025 \text{ mole} \times 0.4 \text{ mole}}{1 \text{ mole}} \\
 &= 0.0010 \text{ mole} \\
 \text{g} &= n \times \text{MW} \\
 &= 0.0010 \times 404 \\
 &= 0.404 \text{ g}
 \end{aligned}$$

Citric acid

General formula of K₂NiF₄-typed structure is A₂BO₄, L₂NF-64 based on 0.0025 mole

To form the complex, moles of metal : moles of citric acid = 1:1

$$\begin{aligned}
 \text{La, 1 mole, amount metal [NO}_3\text{] of} &= 2 \text{ mole} \\
 &= \frac{2 \text{ mole} \times 0.0050 \text{ mole}}{1 \text{ mole}} \\
 &= 0.01 \text{ mole}
 \end{aligned}$$

$$\begin{aligned}
 \text{Ni, 1 mole, amount metal [NO}_3\text{] of} &= 2 \text{ mole} \\
 &= \frac{2 \text{ mole} \times 0.0010 \text{ mole}}{1 \text{ mole}} \\
 &= 2.0 \times 10^{-3} \text{ mole}
 \end{aligned}$$

$$\begin{aligned}
 \text{Fe, 1 mole, amount metal [NO}_3\text{] of} &= 3 \text{ mole} \\
 &= \frac{3 \text{ mole} \times 0.00150 \text{ mole}}{1 \text{ mole}} \\
 &= 4.5 \times 10^{-3} \text{ mole}
 \end{aligned}$$

$$\begin{aligned}
 \text{Total of amount [NO}_3\text{]} &= 0.01 + 2.0 \times 10^{-3} + 4.5 \times 10^{-3} \text{ mole} \\
 &= 0.00165 \text{ mole}
 \end{aligned}$$

$$\begin{aligned}
 \text{Weight of citric acid} &= n \times \text{MW} \\
 &= 0.00165 \times 192.43 \\
 &= 3.1750 \text{ g}
 \end{aligned}$$

3. The calculate lattice parameters**Orthorhombic system**

$$1/d^2 = (h^2/a^2) + (k^2/b^2) + (l^2/c^2)$$

Rhombohedral system

$$1/d^2 = \frac{[(h^2+k^2+l^2) \sin 2\alpha + 2(hl+kl+hl)2 \cos^2 \alpha - \cos \alpha]}{a^2(1-3 \cos^2 \alpha + 2 \cos^2 \alpha)}$$

Tetragonal system

$$1/d^2 = (h^2 + k^2)/a^2 + l^2/c^2$$

Example The calculation of the 101 plane of an orthorhombic cell with $a = 5.5669$ nm, $b = 7.8547$ nm and $c = 5.553$ nm, as shown Figure A-1

$$\begin{aligned}
 \text{From } 1/d^2 &= (h^2/a^2) + (k^2/b^2) + (l^2/c^2) \\
 1/d^2 &= 1/(0.55669^2) + 0 + 1/(0.5553^2) \\
 &= 1/0.3099 + 0 + 1/0.3083 \\
 &= 3.2268 + 0 + 3.2435 \\
 &= 6.4703 \text{ (nm)}^{-2} \\
 &= \sqrt{1/6.4703} \\
 d &= 0.3930 \text{ nm or } 3.930 \text{ \AA} \text{ (show No.3)}
 \end{aligned}$$

PDF#37-1493: QM=Star(S); d=Diffraction; l=Diffraction													PDF Card		
Iron Lanthanum Oxide															
Fe La O3															
Radiation=CuKa1				Lambda=1.5405981				Filter=Graph							
Calibration=Internal(W)				2T=22.605-112.539				I/c(RIR)=							
Ref: McMurdie, H., Morris, M., Evans, E., Paretzkin, B., Wood, E.A., and G. B. Barab, C. Powder Diffraction, v1 p269 (1986)															
Orthorhombic - Powder Diffraction, Pn*a (62) No.2															
CELL: 5.5669 x 7.8547 x 5.553 <90.0 x 90.0 x 90.0> Z=4 mp=															
Density(c)=6.640				Density(m)=6.25A				Mwt=242.75				Vol=242.81			
Ref: 1. Geller, S., Wood, E.A. Acta Crystallogr., v9 p563 (1956)															
NOTE: A stoichiometric mixture of La (OH)3 and Fe2O3 was heated overnight to 1000\$DE, then 1 day each at 1200\$DE and 1350\$DE. The structure was qualitatively determined by Geller and Wood (1). A rhombohedral phase was found above 980\$DE (Dalziel, 2). The mean temperature of data collection was 25.4\$DE. To replace 15-148, Geller and Wood (1).															
Color: Dark brown															
Strong Lines: 2.78/X 1.60/4 1.97/3 2.27/2 3.93/2 1.39/2 1.05/1 1.24/1 0.93/1 1.76/1															
54 Lines, Wavelength to Compute Theta = 1.54056A(Cu), I%-Type = Peak Height															
#	d(A)	I(f)	(h k l)	2-Theta	Theta	1/(2d)	#	d(A)	I(f)	(h k l)	2-Theta	Theta	1/(2d)		
1	3.9302	17.0	(1 0 1)	22.605	11.303	0.1272	28	1.2288	2.0	(4 1 2)	77.636	38.818	0.4069		
2	3.5169	4.0	(1 1 1)	25.303	12.652	0.1422	29	1.2276	2.0	(2 5 2)	77.729	38.865	0.4073		
3	2.778	0.0	(1 2 1)	32.000	16.000	0.1799	30	1.1976	0.0	(0 5 3)	80.063	40.031	0.4175		
4	2.62	0.0	(2 1 0)	34.375	17.072	0.1906	31	1.1847	3.0	(2 6 0)	81.113	40.557	0.4221		

Figure A-1 An example of PDF-file from 37-1493 database.

4. The calculation of the volume per formula unit of LNF (perovskite structure) and L₂NF (K₂NiF₄-typed structure)

$$\text{The volume per formula unit} = \frac{V (\text{\AA}^3)}{Z}$$

V = volume of unit cell

Z = number of formula per unit cell

(show figure A-1 No.4)

$$\begin{aligned} \text{From Orthorhombic} &= a \times b \times c \\ \text{LNF-37} &= 5.5219 \times 7.8102 \times 5.5216 \\ &= 238.13 \text{ \AA}^3/4 \\ &= 59.53 \text{ \AA}^3 \end{aligned}$$

$$\begin{aligned} \text{From Rhombohedral} &= a^2 \times c \sin (60^\circ) \\ \text{LNF-64} &= 5.4921 \times 5.4921 \times 6.6413 \\ &= 173.48 \text{ \AA}^3/3 \\ &= 57.82 \text{ \AA}^3 \end{aligned}$$

$$\begin{aligned} \text{From Tetragonal} &= a^2 \times c \\ \text{L}_2\text{NF-91} &= 3.8944 \times 3.8944 \times 12.5711 \\ &= 190.65 \text{ \AA}^3 / 2 \\ &= 95.325 \text{ \AA}^3 \end{aligned}$$

APPENDIX B

The Morphology of samples were recorded using SEM

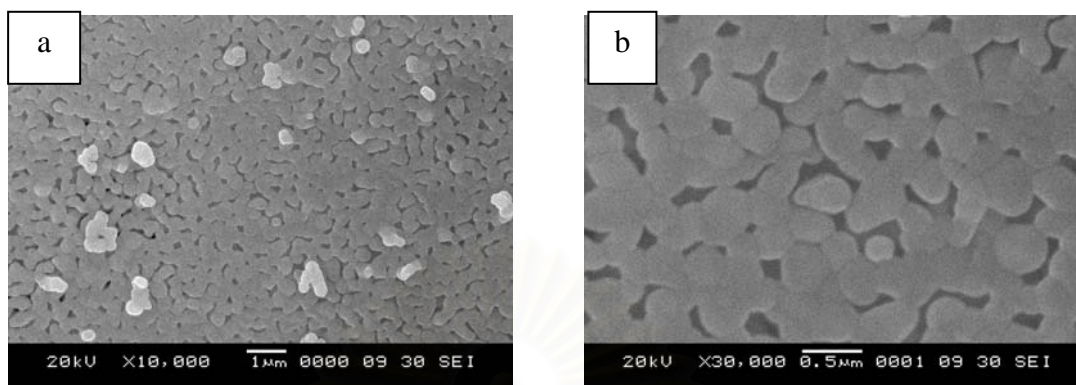


Figure B-1 SEM pictures of LNF-64, synthesized by MWC method at the calcinations temperature of 1000°C for 5h with the magnification of (a) x 10,000 , and (b) x 30,000

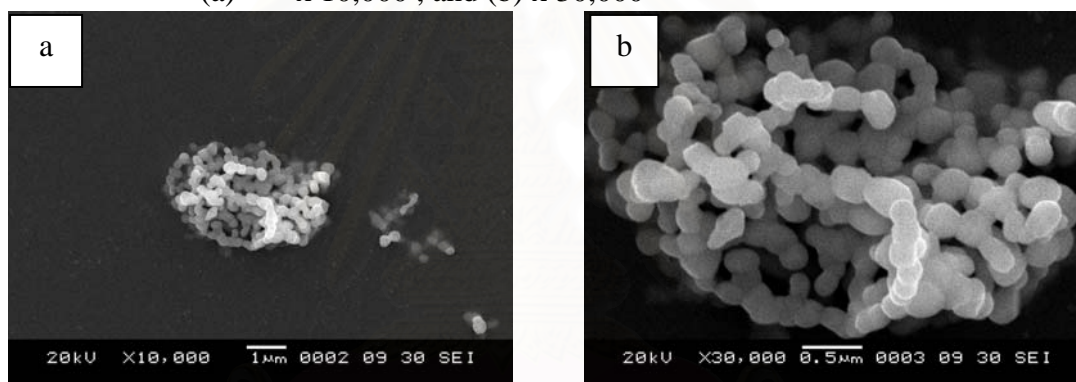


Figure B-2 SEM pictures of LNF-64 (zoom 1 point), synthesized by MWC method at the calcinations temperature of 1000°C for 5h with the magnification of (a) x 10,000 , and (b) x 30,000

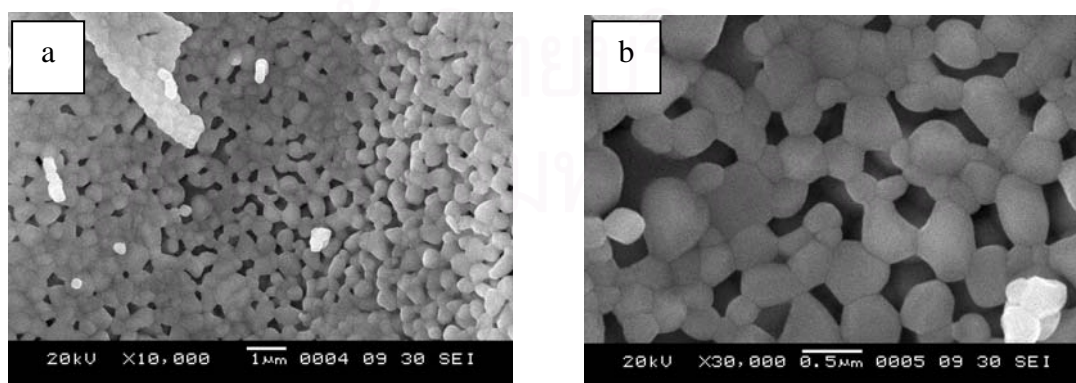


Figure B-3 SEM pictures of LNF-64, synthesized by WC method at the calcinations temperature of 1000°C for 5h with the magnification of (a) x 10,000 , and (b) x 30,000

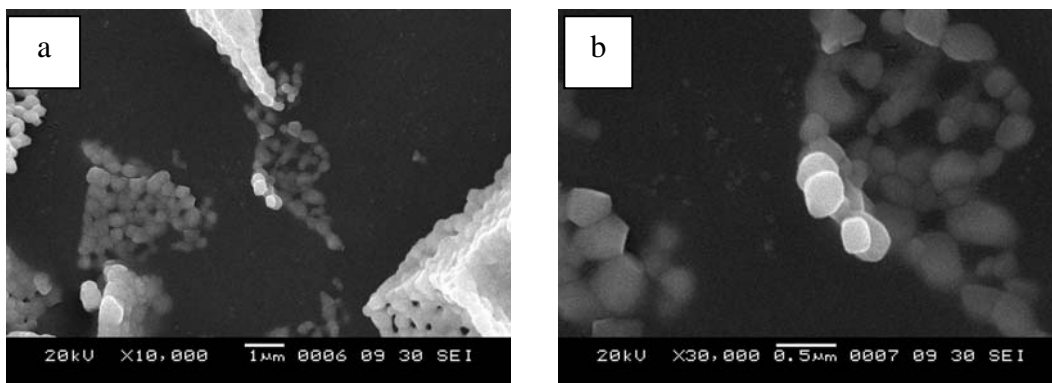


Figure B-4 SEM pictures of LNF-64 (zoom 1 point), synthesized by WC method at the calcinations temperature of 1000°C for 5h with the magnification of (a) x 10,000 , and (b) x 30,000

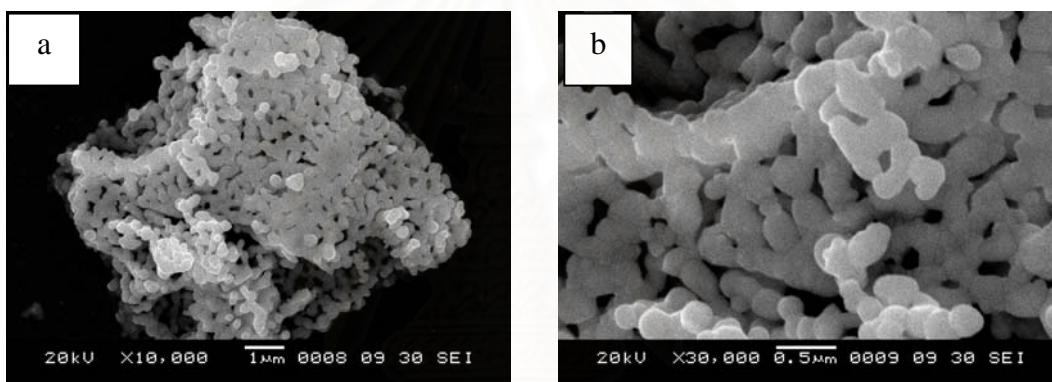


Figure B-5 SEM pictures of LNF-37, synthesized by MWC method at the calcinations temperature of 1000°C for 5h with the magnification of (a) x 10,000 , and (b) x 30,000

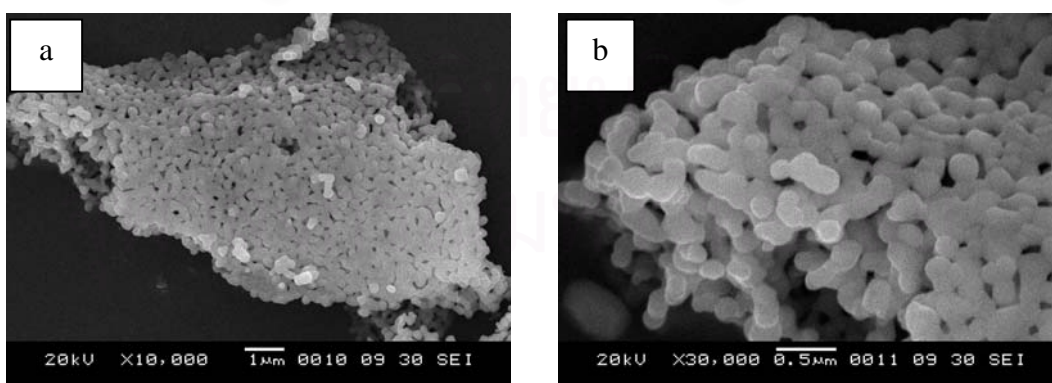


Figure B-6 SEM pictures of LNF-37, synthesized by WC method at the calcinations temperature of 1000°C for 5h with the magnification of (a) x 10,000 , and (b) x 30,000

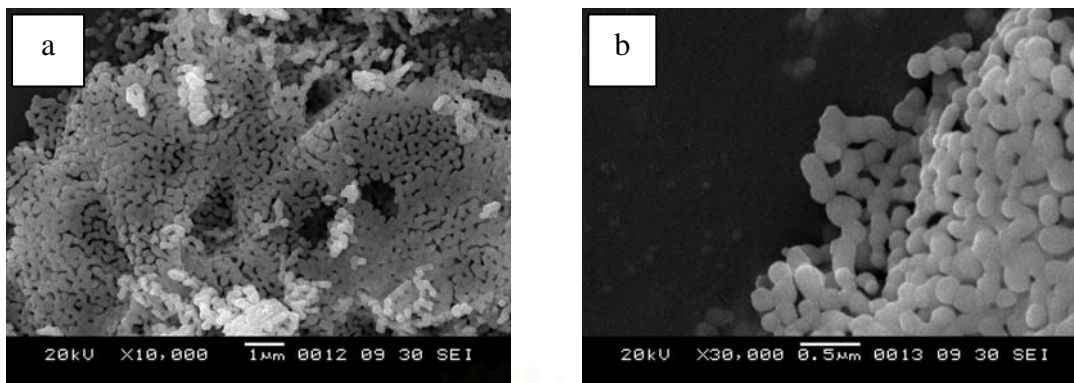


Figure B-7 SEM pictures of LNF-37, synthesized by MWC method at the calcinations temperature of 900°C for 5h with the magnification of (a) x 10,000 , and (b) x 30,000

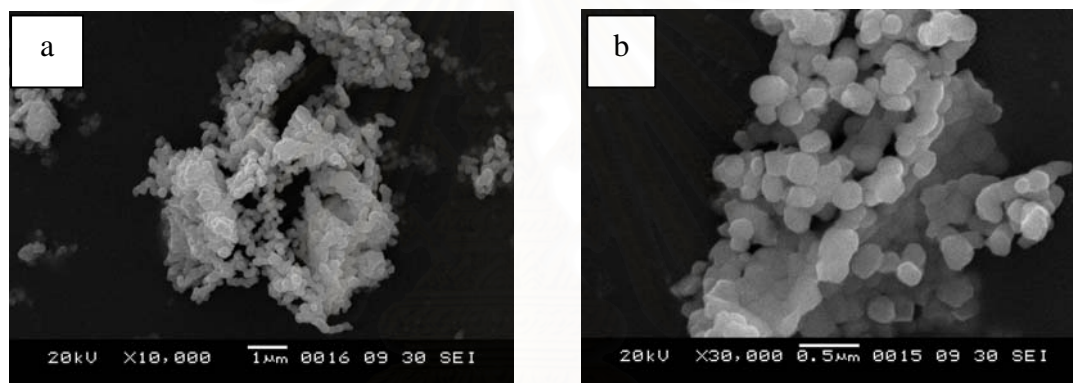


Figure B-8 SEM pictures of LNF-64, synthesized by MWC method at the calcinations temperature of 900°C for 5h with the magnification of (a) x 10,000 , and (b) x 30,000

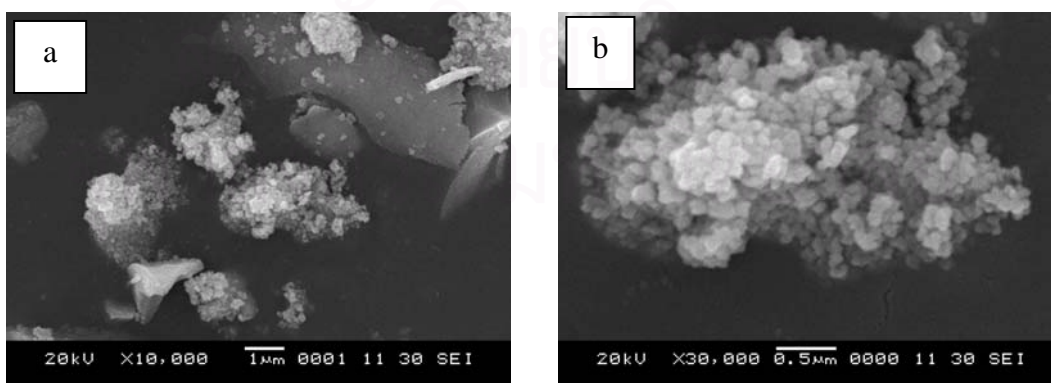


Figure B-9 SEM pictures of LNF-91, synthesized by WC method at the calcinations temperature of 700°C for 5h with the magnification of (a) x 10,000 , and (b) x 30,000

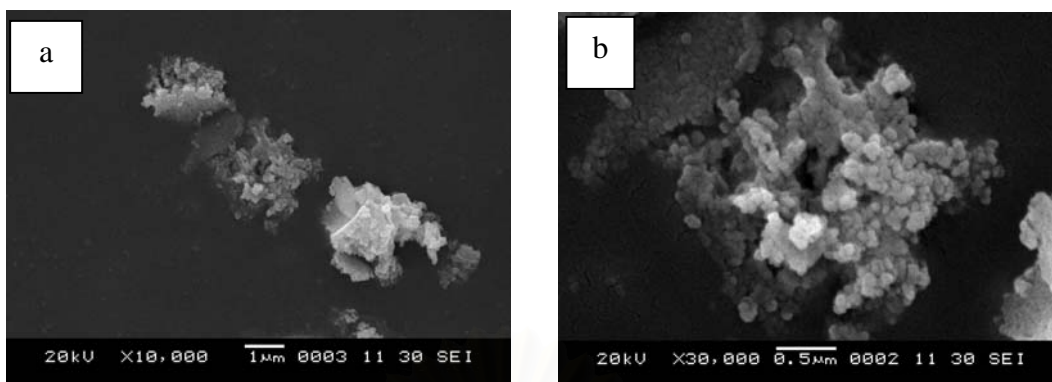


Figure B-10 SEM pictures of LNF-91, synthesized by MWC method at the calcinations temperature of 700°C for 5h with the magnification of (a) x 10,000 , and (b) x 30,000

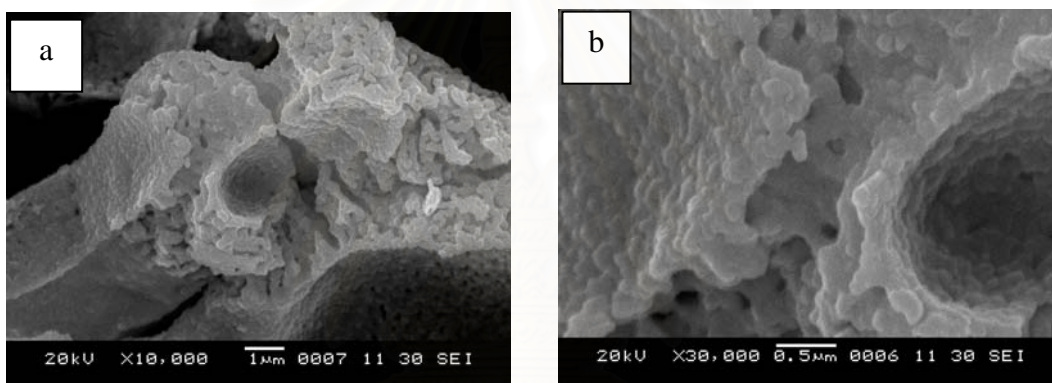


Figure B-11 SEM pictures of LNF-91, synthesized by WC method at the calcinations temperature of 900°C for 5h with the magnification of (a) x 10,000 , and (b) x 30,000

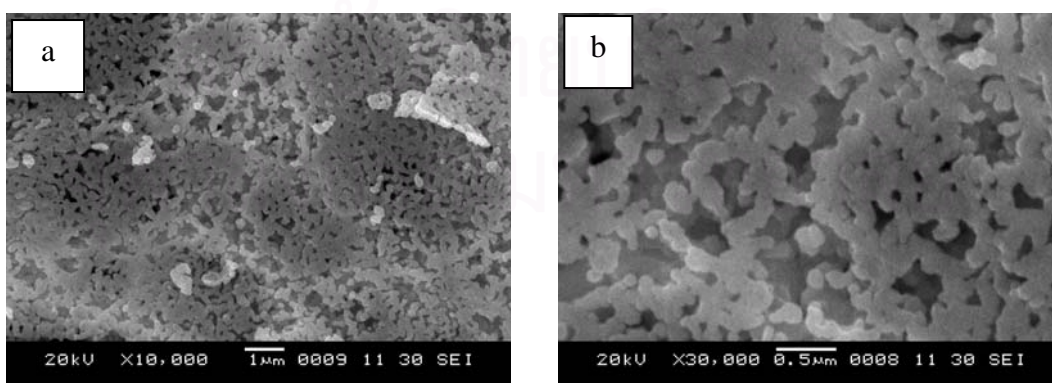


Figure B-12 SEM pictures of LNF-91, synthesized by MWC method at the calcinations temperature of 900°C for 5h with the magnification of (a) x 10,000 , and (b) x 30,000

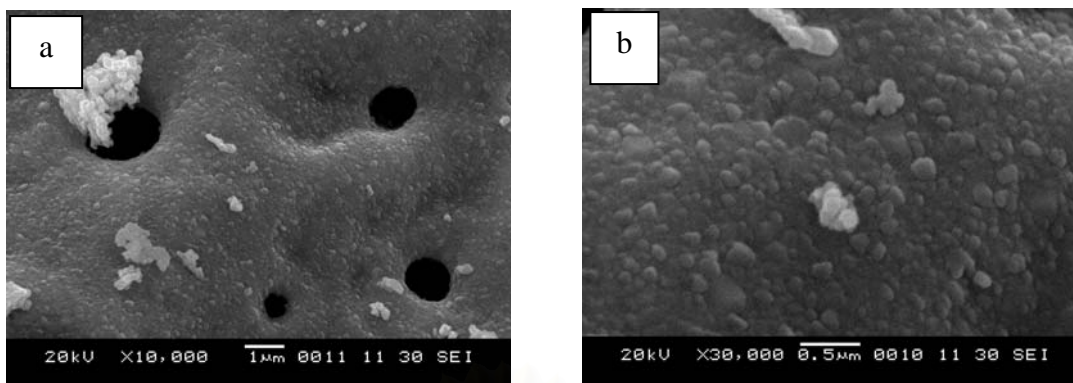


Figure B-13 SEM pictures of LNF-91, synthesized by NC method at the calcinations temperature of 900°C for 5h with the magnification of (a) x 10,000 , and (b) x 30,000

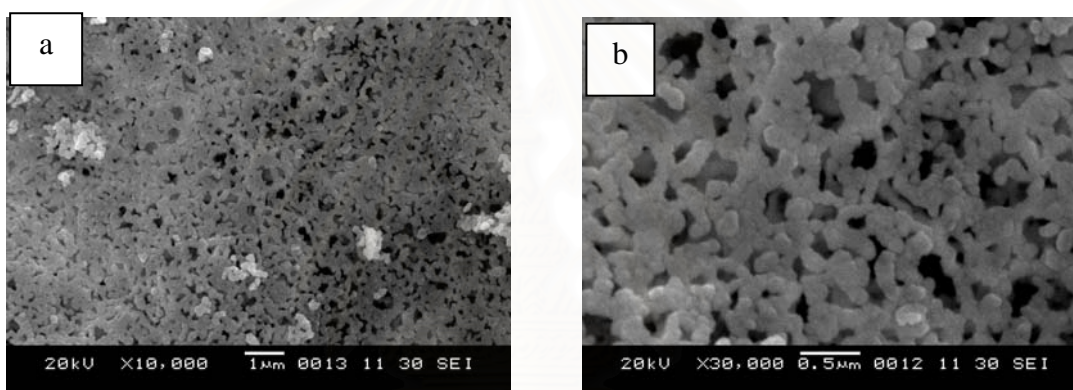


Figure B-14 SEM pictures of LNF-91, synthesized by MNC method at the calcinations temperature of 900°C for 5h with the magnification of (a) x 10,000 , and (b) x 30,000

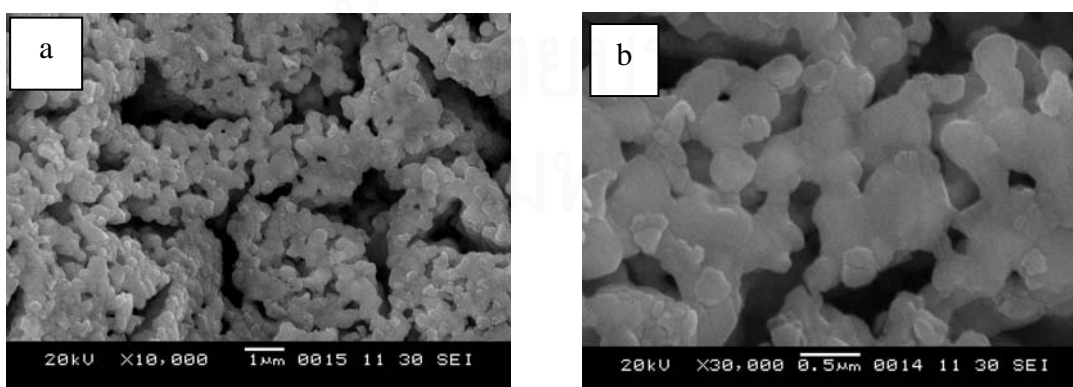


Figure B-15 SEM pictures of LNF-91, synthesized by WC method at the calcinations temperature of 1000°C for 5h with the magnification of (a) x 10,000 , and (b) x 30,000

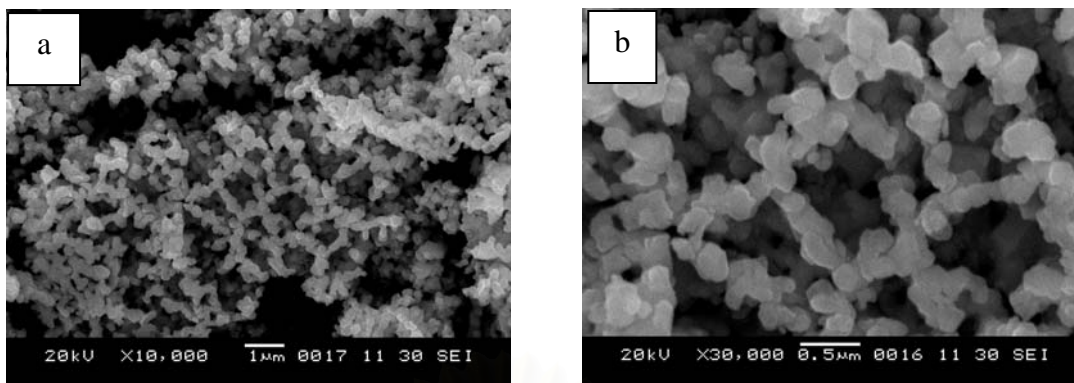


Figure B-16 SEM pictures of LNF-91, synthesized by MWC method at the calcinations temperature of 1000°C for 5h with the magnification of (a) x 10,000 , and (b) x 30,000

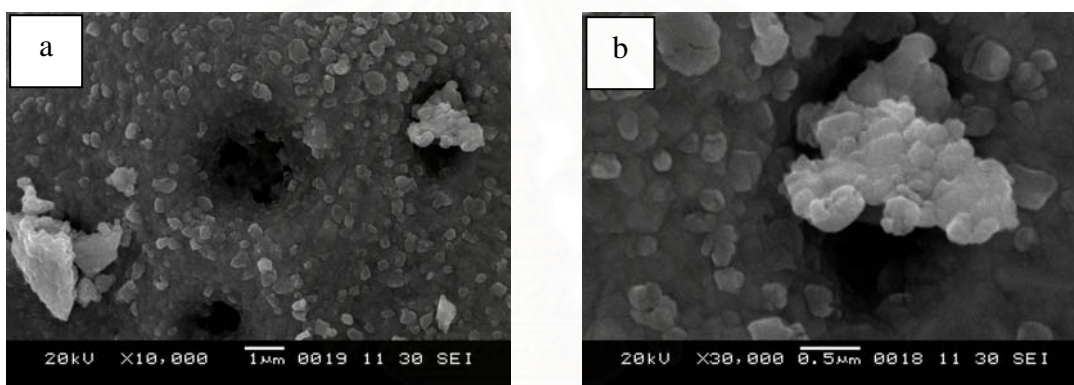


Figure B-17 SEM pictures of LNF-91, synthesized by WC method at the calcinations temperature of 1000°C for 5h with the magnification of (a) x 10,000 , and (b) x 30,000

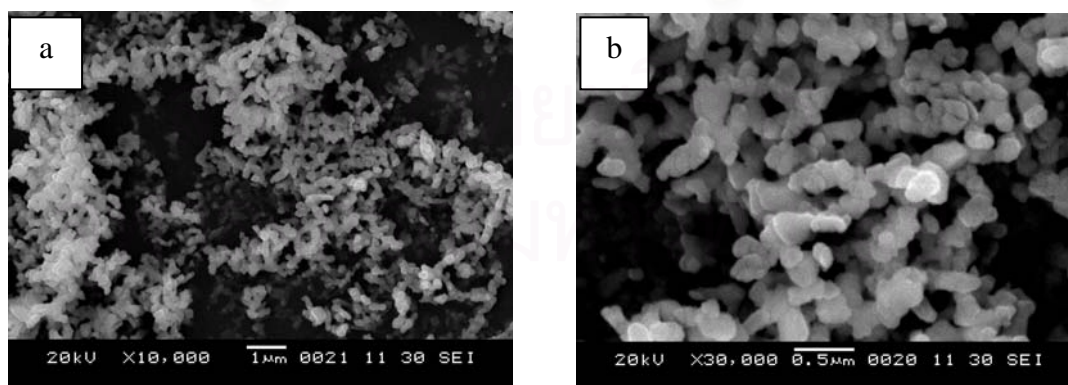


Figure B-17 SEM pictures of LNF-91, synthesized by MNC method at the calcinations temperature of 1000°C for 5h with the magnification of (a) x 10,000 , and (b) x 30,000

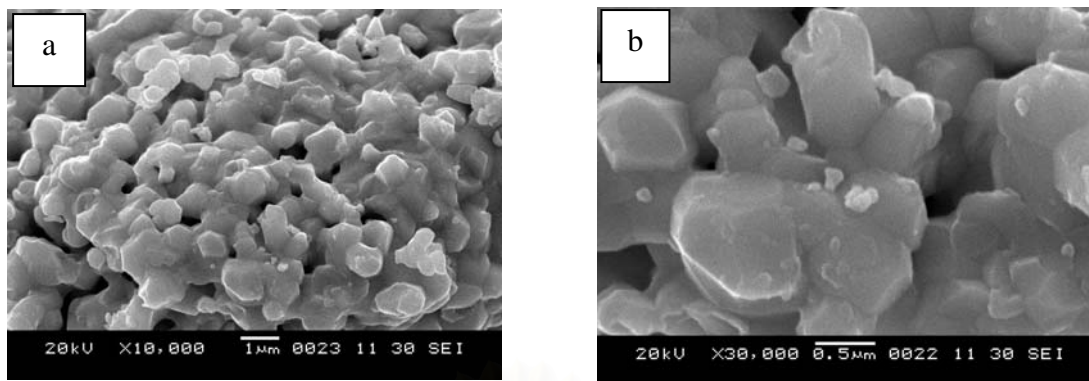


Figure B-18 SEM pictures of LNF-91, synthesized by WC method at the calcinations temperature of 1200°C for 5h with the magnification of (a) x 10,000 , and (b) x 30,000

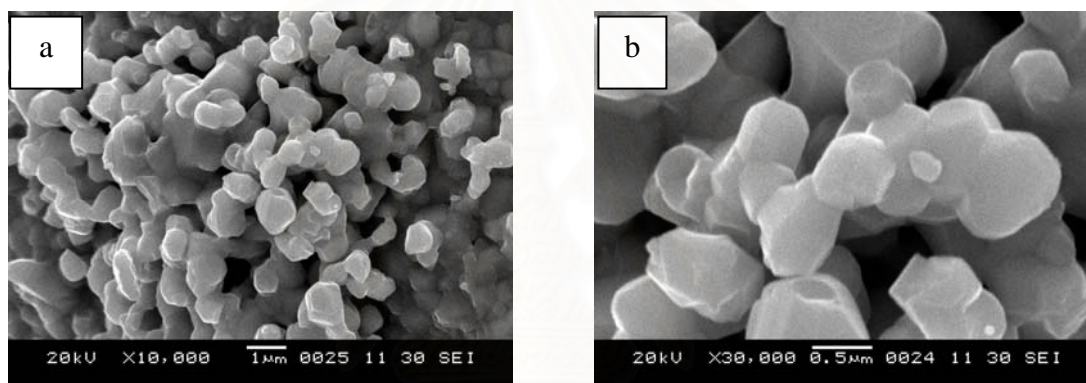


Figure B-18 SEM pictures of LNF-91, synthesized by MWC method at the calcinations temperature of 1200°C for 5h with the magnification of (a) x 10,000 , and (b) x 30,000

สถาบันวิทยบริการ
จุฬาลงกรณ์มหาวิทยาลัย

APPENDIX C

The Particle size-distribution of LNF-64 synthesized by four methods WC, MWC, NC, and (d) MNC with the calcination temperature of 1000 °C for 5 h. Each method run 3 time.



สถาบันวิทยบริการ
จุฬาลงกรณ์มหาวิทยาลัย

Result: Analysis Report

Sample Details

Sample ID: Sample 2
 Sample File: IH002_51
 Sample Path: D:\DATASIZE\IN-HOUSE\IH_51\

Run Number: 2
 Record Number: 250

Measured: Tue Mar 11 2008 3:13PM
 Analysed: Tue Mar 11 2008 3:13PM
 Result Source: Analysed

Sample Notes: Medium : DI water

Dispersant : Sodium pyrophosphate
 Treatment : Ultrasonic 5 minutes & Stir medium
 Note : LNF-64-WL-1000 C, 30 minutes, 30/01/51

System Details

Range Lens: 300RF mm
 Presentation: 3_BRTI
 Analysis Model: Polydisperse
 Modifications: None

Beam Length: 2.40 mm
 [Particle R.I. = (2.4000, 0.1000); Dispersant R.I. = 1.3300]

Sampler: MS1

Obscuration: 20.0 %

Residual: 1.086 %

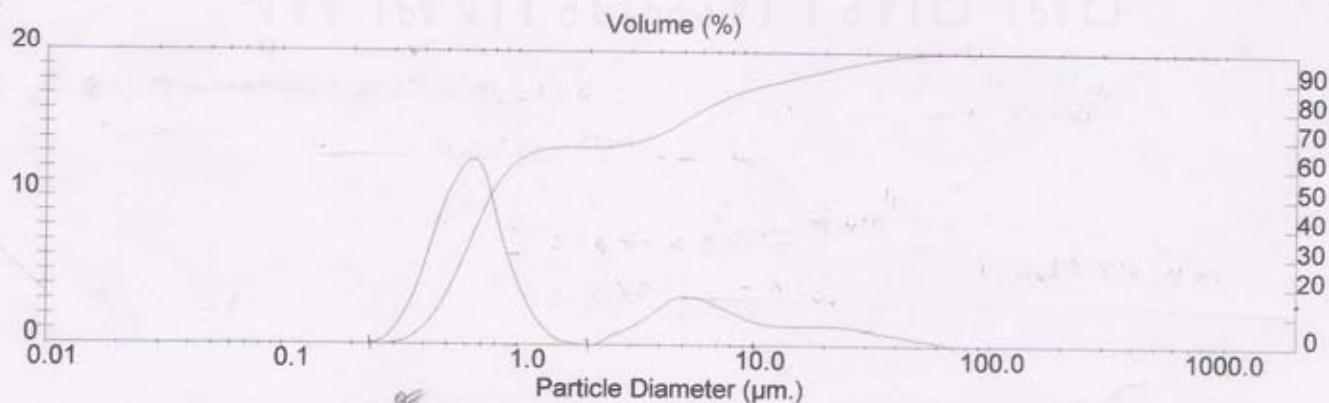
Result Statistics

Distribution Type: Volume
 Mean Diameters:
 D [4, 3] = 4.46 um

Concentration = 0.0017 %Vol
 D (v, 0.1) = 0.44 um
 D [3, 2] = 0.84 um
 Density = 1.000 g / cub. cm
 D (v, 0.5) = 0.76 um
 Span = 1.609E+01

Specific S.A. = 7.1287 sq. m / g
 D (v, 0.9) = 12.73 um
 Uniformity = 5.121E+00

Size Low (um)	In %	Size High (um)	Under%	Size Low (um)	In %	Size High (um)	Under%
0.05	0.00	0.06	0.00	6.63	2.60	7.72	84.48
0.06	0.00	0.07	0.00	7.72	2.09	9.00	86.57
0.07	0.00	0.08	0.00	9.00	1.67	10.48	88.24
0.08	0.00	0.09	0.00	10.48	1.40	12.21	89.64
0.09	0.00	0.11	0.00	12.21	1.29	14.22	90.94
0.11	0.00	0.13	0.00	14.22	1.28	16.57	92.22
0.13	0.00	0.15	0.00	16.57	1.30	19.31	93.53
0.15	0.00	0.17	0.00	19.31	1.30	22.49	94.82
0.17	0.00	0.20	0.00	22.49	1.23	26.20	96.05
0.20	0.00	0.23	0.00	26.20	1.10	30.53	97.15
0.23	0.12	0.27	0.12	30.53	0.92	35.56	98.08
0.27	0.79	0.31	0.91	35.56	0.75	41.43	98.82
0.31	2.35	0.36	3.26	41.43	0.57	48.27	99.39
0.36	4.98	0.42	8.24	48.27	0.39	56.23	99.78
0.42	8.32	0.49	16.56	56.23	0.22	65.51	100.00
0.49	10.93	0.58	27.49	65.51	0.00	76.32	100.00
0.58	12.45	0.67	39.93	76.32	0.00	88.91	100.00
0.67	11.59	0.78	51.53	88.91	0.00	103.58	100.00
0.78	7.61	0.91	59.14	103.58	0.00	120.67	100.00
0.91	4.51	1.06	63.65	120.67	0.00	140.58	100.00
1.06	2.24	1.24	65.89	140.58	0.00	163.77	100.00
1.24	0.87	1.44	66.76	163.77	0.00	190.80	100.00
1.44	0.26	1.68	67.02	190.80	0.00	222.28	100.00
1.68	0.06	1.95	67.08	222.28	0.00	258.95	100.00
1.95	0.02	2.28	67.09	258.95	0.00	301.68	100.00
2.28	0.61	2.65	67.70	301.68	0.00	351.46	100.00
2.65	0.96	3.09	68.66	351.46	0.00	409.45	100.00
3.09	1.55	3.60	70.21	409.45	0.00	477.01	100.00
3.60	2.27	4.19	72.48	477.01	0.00	555.71	100.00
4.19	3.07	4.88	75.54	555.71	0.00	647.41	100.00
4.88	3.27	5.69	78.81	647.41	0.00	754.23	100.00
5.69	3.06	6.63	81.87	754.23	0.00	878.67	100.00



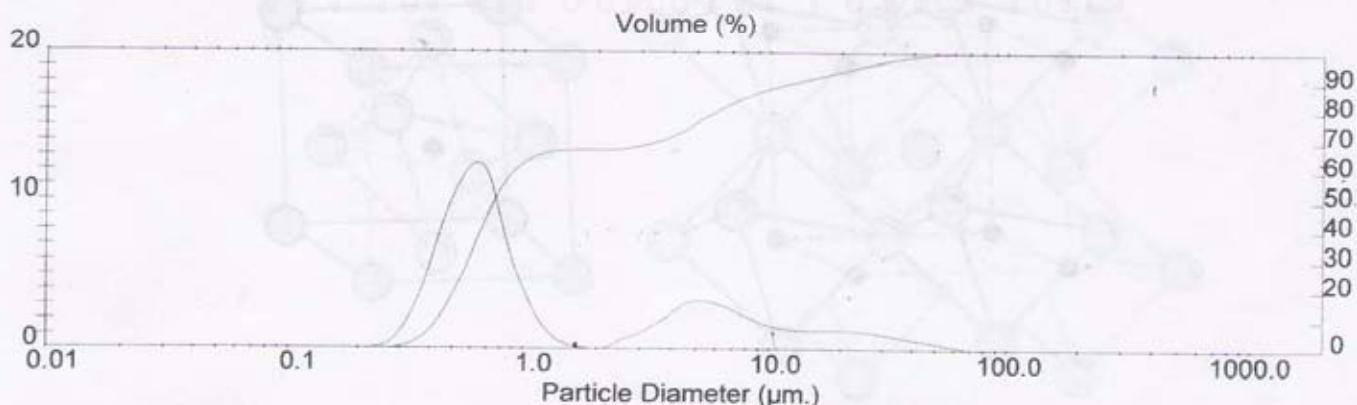
Result: Analysis Report

Sample Details
 Sample ID: Sample 2 Run Number: 11 Measured: Tue Mar 11 2008 3:14PM
 Sample File: IH002_51 Record Number: 259 Analysed: Tue Mar 11 2008 3:14PM
 Sample Path: D:\DATASIZE\IN-HOUSE\IH_51\ Result Source: Analysed
 Sample Notes: Medium : DI water
 Dispersant : Sodium pyrophosphate
 Treatment : Ultrasonic 5 minutes & Stir medium
 Note : LNF-64-WL-1000 C, 30 minutes, 30/01/51

System Details
 Range Lens: 300RF mm Beam Length: 2.40 mm Sampler: MS1 Obscuration: 20.1 %
 Presentation: 3_BRTI [Particle R.I. = (2.4000, 0.1000); Dispersant R.I. = 1.3300]
 Analysis Model: Polydisperse Residual: 1.080 %
 Modifications: None

Result Statistics
 Distribution Type: Volume Concentration = 0.0017 %Vol Density = 1.000 g / cub. cm Specific S.A. = 7.1827 sq. m / g
 Mean Diameters: D (v, 0.1) = 0.44 um D (v, 0.5) = 0.76 um D (v, 0.9) = 12.75 um
 D [4, 3] = 4.45 um D [3, 2] = 0.84 um Span = 1.623E+01 Uniformity = 5.143E+00

Size Low (um)	In %	Size High (um)	Under%	Size Low (um)	In %	Size High (um)	Under%
0.05	0.00	0.06	0.00	6.63	2.60	7.72	84.43
0.06	0.00	0.07	0.00	7.72	2.09	9.00	86.52
0.07	0.00	0.08	0.00	9.00	1.68	10.48	88.20
0.08	0.00	0.09	0.00	10.48	1.42	12.21	89.62
0.09	0.00	0.11	0.00	12.21	1.31	14.22	90.93
0.11	0.00	0.13	0.00	14.22	1.30	16.57	92.23
0.13	0.00	0.15	0.00	16.57	1.32	19.31	93.55
0.15	0.00	0.17	0.00	19.31	1.31	22.49	94.85
0.17	0.00	0.20	0.00	22.49	1.24	26.20	96.09
0.20	0.00	0.23	0.00	26.20	1.11	30.53	97.20
0.23	0.15	0.27	0.16	30.53	0.92	35.56	98.12
0.27	0.87	0.31	1.03	35.56	0.74	41.43	98.86
0.31	2.48	0.36	3.51	41.43	0.56	48.27	99.42
0.36	5.14	0.42	8.65	48.27	0.38	56.23	99.80
0.42	8.46	0.49	17.11	56.23	0.20	65.51	100.00
0.49	11.00	0.58	28.11	65.51	0.00	76.32	100.00
0.58	12.39	0.67	40.50	76.32	0.00	88.91	100.00
0.67	11.43	0.78	51.94	88.91	0.00	103.58	100.00
0.78	7.45	0.91	59.39	103.58	0.00	120.67	100.00
0.91	4.37	1.06	63.76	120.67	0.00	140.58	100.00
1.06	2.14	1.24	65.90	140.58	0.00	163.77	100.00
1.24	0.83	1.44	66.73	163.77	0.00	190.80	100.00
1.44	0.24	1.68	66.97	190.80	0.00	222.28	100.00
1.68	0.05	1.95	67.03	222.28	0.00	258.95	100.00
1.95	0.02	2.28	67.04	258.95	0.00	301.68	100.00
2.28	0.60	2.65	67.64	301.68	0.00	351.46	100.00
2.65	0.96	3.09	68.61	351.46	0.00	409.45	100.00
3.09	1.56	3.60	70.17	409.45	0.00	477.01	100.00
3.60	2.27	4.19	72.44	477.01	0.00	555.71	100.00
4.19	3.07	4.88	75.51	555.71	0.00	647.41	100.00
4.88	3.27	5.69	78.78	647.41	0.00	754.23	100.00
5.69	3.05	6.63	81.83	754.23	0.00	878.67	100.00



Result: Analysis Report

Sample ID: Sample 2	Run Number: 15	Measured: Tue Mar 11 2008 3:15PM
Sample File: IH002_51	Record Number: 263	Analysed: Tue Mar 11 2008 3:15PM
Sample Path: D:\DATASIZE\IN-HOUSE\IH_51\		Result Source: Analysed
Sample Notes: Medium : DI water		
Dispersant : Sodium pyrophosphate		
Treatment : Ultrasonic 5 minutes & Stir medium		
Note : LNF-64-WL-1000 C, 30 minutes, 30/01/51		

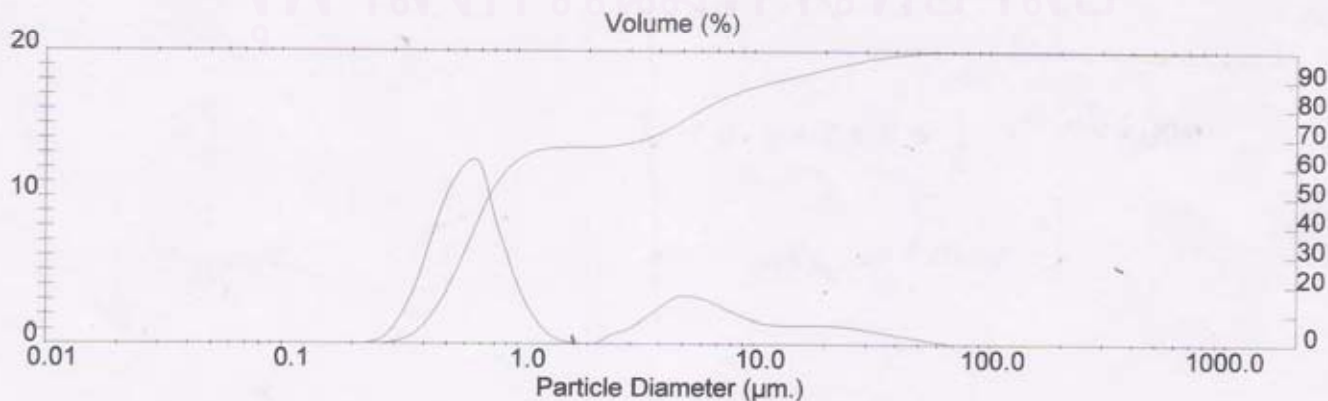
System Details

Range Lens: 300RF mm	Beam Length: 2.40 mm	Sampler: MS1	Obscuration: 20.1 %
Presentation: 3_BRTI	[Particle R.I. = (2.4000, 0.1000);	Dispersant R.I. = 1.3300]	
Analysis Model: Polydisperse			Residual: 1.070 %
Modifications: None			

Result Statistics

Distribution Type: Volume	Concentration = 0.0017 %Vol	Density = 1.000 g / cub. cm	Specific S.A. = 7.2003 sq. m / g
Mean Diameters:	D (v, 0.1) = 0.44 um	D (v, 0.5) = 0.76 um	D (v, 0.9) = 12.77 um
D [4, 3] = 4.44 um	D [3, 2] = 0.83 um	Span = 1.632E+01	Uniformity = 5.150E+00

Size Low (um)	In %	Size High (um)	Under%	Size Low (um)	In %	Size High (um)	Under%
0.05	0.00	0.06	0.00	6.63	2.59	7.72	84.41
0.06	0.00	0.07	0.00	7.72	2.09	9.00	86.50
0.07	0.00	0.08	0.00	9.00	1.68	10.48	88.17
0.08	0.00	0.09	0.00	10.48	1.43	12.21	89.60
0.09	0.00	0.11	0.00	12.21	1.33	14.22	90.93
0.11	0.00	0.13	0.00	14.22	1.32	16.57	92.25
0.13	0.00	0.15	0.00	16.57	1.33	19.31	93.59
0.15	0.00	0.17	0.00	19.31	1.32	22.49	94.90
0.17	0.00	0.20	0.00	22.49	1.24	26.20	96.14
0.20	0.00	0.23	0.00	26.20	1.10	30.53	97.24
0.23	0.16	0.27	0.17	30.53	0.91	35.56	98.15
0.27	0.89	0.31	1.06	35.56	0.73	41.43	98.88
0.31	2.52	0.36	3.58	41.43	0.55	48.27	99.44
0.36	5.19	0.42	8.77	48.27	0.37	56.23	99.80
0.42	8.51	0.49	17.28	56.23	0.19	65.51	99.99
0.49	11.02	0.58	28.30	65.51	0.01	76.32	100.00
0.58	12.39	0.67	40.69	76.32	0.00	88.91	100.00
0.67	11.39	0.78	52.08	88.91	0.00	103.58	100.00
0.78	7.40	0.91	59.48	103.58	0.00	120.67	100.00
0.91	4.33	1.06	63.81	120.67	0.00	140.58	100.00
1.06	2.11	1.24	65.92	140.58	0.00	163.77	100.00
1.24	0.81	1.44	66.73	163.77	0.00	190.80	100.00
1.44	0.23	1.68	66.97	190.80	0.00	222.28	100.00
1.68	0.05	1.95	67.02	222.28	0.00	258.95	100.00
1.95	0.02	2.28	67.04	258.95	0.00	301.68	100.00
2.28	0.60	2.65	67.64	301.68	0.00	351.46	100.00
2.65	0.96	3.09	68.60	351.46	0.00	409.45	100.00
3.09	1.56	3.60	70.16	409.45	0.00	477.01	100.00
3.60	2.29	4.19	72.45	477.01	0.00	555.71	100.00
4.19	3.07	4.88	75.52	555.71	0.00	647.41	100.00
4.88	3.26	5.69	78.78	647.41	0.00	754.23	100.00
5.69	3.04	6.63	81.82	754.23	0.00	878.67	100.00



Result: Analysis Report

Sample ID: Sample 4
 Sample File: IH002_51
 Sample Path: D:\DATASIZE\IN-HOUSE\IH_51\
 Sample Notes: Medium : DI water

Sample Details
 Run Number: 6
 Record Number: 284

Measured: Tue Mar 11 2008 3:33PM
 Analysed: Tue Mar 11 2008 3:33PM
 Result Source: Analysed

Dispersant : Sodium pyrophosphate
 Treatment : Ultrasonic 5 minutes & Stir medium
 Note : LNF-64-MWC-1000 C, 30 minutes, 30/01/51

System Details

Range Lens: 300RF mm
 Presentation: 3_BRTI
 Analysis Model: Polydisperse
 Modifications: None

Beam Length: 2.40 mm
 [Particle R.I. = (2.4000, 0.1000); Dispersant R.I. = 1.3300]

Sampler: MS1
 Obscuration: 19.8 %
 Residual: 1.346 %

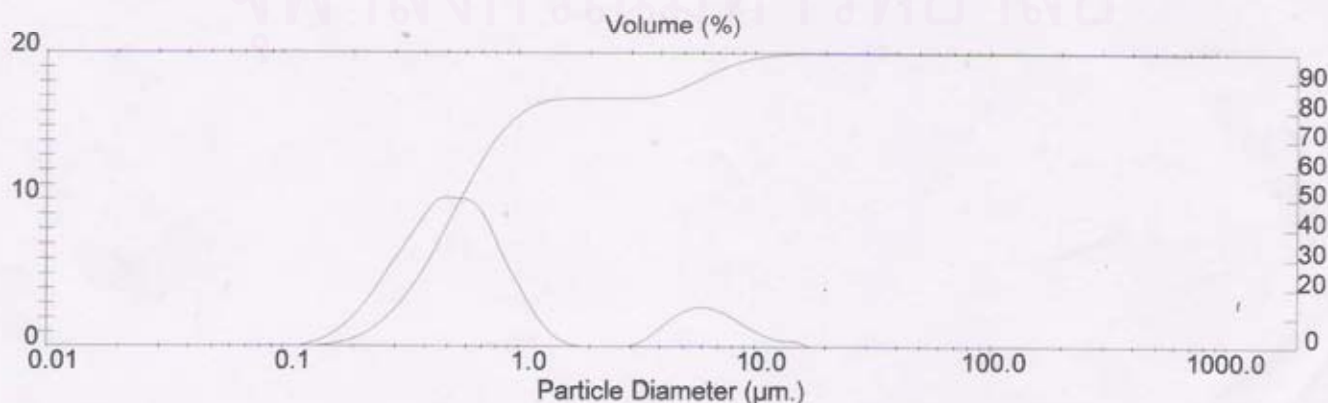
Result Statistics

Distribution Type: Volume
 Mean Diameters:
 D [4, 3] = 1.54 um

Concentration = 0.0010 %Vol
 D (v, 0.1) = 0.28 um
 D [3, 2] = 0.52 um
 Density = 1.000 g / cub. cm
 D (v, 0.5) = 0.57 um
 Span = 9.297E+00

Specific S.A. = 11.5883 sq. m / g
 D (v, 0.9) = 5.57 um
 Uniformity = 2.042E+00

Size Low (um)	In %	Size High (um)	Under%	Size Low (um)	In %	Size High (um)	Under%
0.05	0.00	0.06	0.00	6.63	2.41	7.72	95.50
0.06	0.00	0.07	0.00	7.72	1.84	9.00	97.34
0.07	0.00	0.08	0.00	9.00	1.21	10.48	98.55
0.08	0.00	0.09	0.00	10.48	0.71	12.21	99.25
0.09	0.00	0.11	0.00	12.21	0.42	14.22	99.67
0.11	0.03	0.13	0.03	14.22	0.33	16.57	100.00
0.13	0.27	0.15	0.30	16.57	0.00	19.31	100.00
0.15	0.74	0.17	1.04	19.31	0.00	22.49	100.00
0.17	1.49	0.20	2.53	22.49	0.00	26.20	100.00
0.20	2.59	0.23	5.12	26.20	0.00	30.53	100.00
0.23	4.04	0.27	9.15	30.53	0.00	35.56	100.00
0.27	5.67	0.31	14.82	35.56	0.00	41.43	100.00
0.31	7.18	0.36	22.00	41.43	0.00	48.27	100.00
0.36	8.71	0.42	30.71	48.27	0.00	56.23	100.00
0.42	9.96	0.49	40.66	56.23	0.00	65.51	100.00
0.49	10.04	0.58	50.70	65.51	0.00	76.32	100.00
0.58	9.89	0.67	60.59	76.32	0.00	88.91	100.00
0.67	8.71	0.78	69.30	88.91	0.00	103.58	100.00
0.78	6.50	0.91	75.80	103.58	0.00	120.67	100.00
0.91	4.47	1.06	80.27	120.67	0.00	140.58	100.00
1.06	2.58	1.24	82.85	140.58	0.00	163.77	100.00
1.24	1.13	1.44	83.98	163.77	0.00	190.80	100.00
1.44	0.33	1.68	84.31	190.80	0.00	222.28	100.00
1.68	0.05	1.95	84.36	222.28	0.00	258.95	100.00
1.95	0.00	2.28	84.36	258.95	0.00	301.68	100.00
2.28	0.00	2.65	84.36	301.68	0.00	351.46	100.00
2.65	0.00	3.09	84.36	351.46	0.00	409.45	100.00
3.09	0.36	3.60	84.72	409.45	0.00	477.01	100.00
3.60	1.12	4.19	85.84	477.01	0.00	555.71	100.00
4.19	1.97	4.88	87.81	555.71	0.00	647.41	100.00
4.88	2.56	5.69	90.37	647.41	0.00	754.23	100.00
5.69	2.71	6.63	93.08	754.23	0.00	878.67	100.00



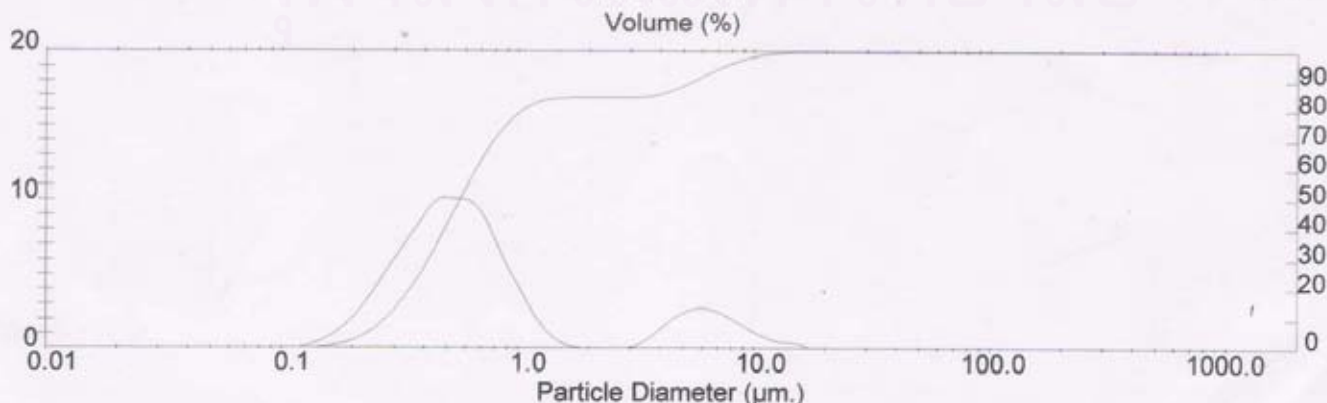
Result: Analysis Report

Sample ID: Sample 4	Run Number: 11	Measured: Tue Mar 11 2008 3:33PM
Sample File: IH002_51	Record Number: 289	Analysed: Tue Mar 11 2008 3:33PM
Sample Path: D:\DATASIZE\IN-HOUSE\IH_51\		Result Source: Analysed
Sample Notes: Medium : DI water		
Dispersant : Sodium pyrophosphate		
Treatment : Ultrasonic 5 minutes & Stir medium		
Note : LNF-64-MWC-1000 C, 30 minutes, 30/01/51		

System Details			
Range Lens: 300RF mm	Beam Length: 2.40 mm	Sampler: MS1	Obscuration: 19.8 %
Presentation: 3_BRTI	[Particle R.I. = (2.4000, 0.1000);	Dispersant R.I. = 1.3300]	
Analysis Model: Polydisperse			Residual: 1.349 %
Modifications: None			

Result Statistics			
Distribution Type: Volume	Concentration = 0.0010 %Vol	Density = 1.000 g / cub. cm	Specific S.A. = 11.5944 sq. m / g
Mean Diameters:	D (v, 0.1) = 0.28 um	D (v, 0.5) = 0.57 um	D (v, 0.9) = 5.57 um
D [4, 3] = 1.54 um	D [3, 2] = 0.52 um	Span = 9.305E+00	Uniformity = 2.042E+00

Size Low (um)	In %	Size High (um)	Under%	Size Low (um)	In %	Size High (um)	Under%
0.05	0.00	0.06	0.00	6.63	2.41	7.72	95.48
0.06	0.00	0.07	0.00	7.72	1.84	9.00	97.33
0.07	0.00	0.08	0.00	9.00	1.22	10.48	98.55
0.08	0.00	0.09	0.00	10.48	0.72	12.21	99.27
0.09	0.00	0.11	0.00	12.21	0.42	14.22	99.69
0.11	0.03	0.13	0.03	14.22	0.31	16.57	100.00
0.13	0.27	0.15	0.30	16.57	0.00	19.31	100.00
0.15	0.74	0.17	1.04	19.31	0.00	22.49	100.00
0.17	1.49	0.20	2.53	22.49	0.00	26.20	100.00
0.20	2.59	0.23	5.12	26.20	0.00	30.53	100.00
0.23	4.04	0.27	9.16	30.53	0.00	35.56	100.00
0.27	5.68	0.31	14.83	35.56	0.00	41.43	100.00
0.31	7.19	0.36	22.02	41.43	0.00	48.27	100.00
0.36	8.72	0.42	30.74	48.27	0.00	56.23	100.00
0.42	9.97	0.49	40.70	56.23	0.00	65.51	100.00
0.49	10.05	0.58	50.75	65.51	0.00	76.32	100.00
0.58	9.90	0.67	60.65	76.32	0.00	88.91	100.00
0.67	8.72	0.78	69.36	88.91	0.00	103.58	100.00
0.78	6.49	0.91	75.85	103.58	0.00	120.67	100.00
0.91	4.46	1.06	80.31	120.67	0.00	140.58	100.00
1.06	2.56	1.24	82.87	140.58	0.00	163.77	100.00
1.24	1.13	1.44	83.99	163.77	0.00	190.80	100.00
1.44	0.33	1.68	84.32	190.80	0.00	222.28	100.00
1.68	0.05	1.95	84.37	222.28	0.00	258.95	100.00
1.95	0.00	2.28	84.37	258.95	0.00	301.68	100.00
2.28	0.00	2.65	84.37	301.68	0.00	351.46	100.00
2.65	0.00	3.09	84.37	351.46	0.00	409.45	100.00
3.09	0.36	3.60	84.73	409.45	0.00	477.01	100.00
3.60	1.12	4.19	85.85	477.01	0.00	555.71	100.00
4.19	1.96	4.88	87.81	555.71	0.00	647.41	100.00
4.88	2.56	5.69	90.37	647.41	0.00	754.23	100.00
5.69	2.70	6.63	93.07	754.23	0.00	878.67	100.00



Result: Analysis Report

Sample ID: Sample 4
Sample File: IH002_51
Sample Path: D:\DATASIZE\IN-HOUSE\IH_51\
Sample Notes: Medium : DI water
 Dispersant : Sodium pyrophosphate
 Treatment : Ultrasonic 5 minutes & Stir medium
 Note : LNF-64-MWC-1000 C, 30 minutes, 30/01/51

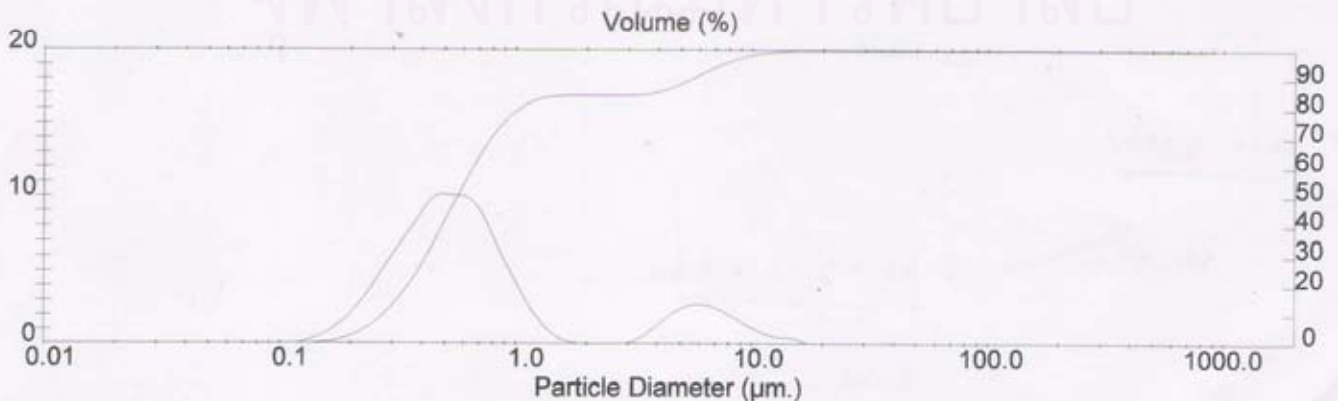
Sample Details
Run Number: 12
Record Number: 290

Measured: Tue Mar 11 2008 3:33PM
Analysed: Tue Mar 11 2008 3:33PM
Result Source: Analysed

System Details
Range Lens: 300RF mm **Beam Length:** 2.40 mm **Sampler:** MS1 **Obscuration:** 19.8 %
Presentation: 3_BRTI **[Particle R.I. = (2.4000, 0.1000); Dispersant R.I. = 1.3300]**
Analysis Model: Polydisperse **Residual:** 1.346 %
Modifications: None

Result Statistics
Distribution Type: Volume **Concentration =** 0.0010 %Vol **Density =** 1.000 g / cub. cm **Specific S.A. =** 11.5977 sq. m / g
Mean Diameters:
D [4, 3] = 1.54 um **D (v, 0.1) =** 0.28 um **D (v, 0.5) =** 0.57 um **D (v, 0.9) =** 5.56 um
 D [3, 2] = 0.52 um **Span =** 9.295E+00 **Uniformity =** 2.042E+00

Size Low (um)	In %	Size High (um)	Under%	Size Low (um)	In %	Size High (um)	Under%
0.05	0.00	0.06	0.00	6.63	2.40	7.72	95.48
0.06	0.00	0.07	0.00	7.72	1.83	9.00	97.31
0.07	0.00	0.08	0.00	9.00	1.21	10.48	98.52
0.08	0.00	0.09	0.00	10.48	0.72	12.21	99.24
0.09	0.00	0.11	0.00	12.21	0.43	14.22	99.67
0.11	0.02	0.13	0.02	14.22	0.33	16.57	100.00
0.13	0.27	0.15	0.30	16.57	0.00	19.31	100.00
0.15	0.74	0.17	1.04	19.31	0.00	22.49	100.00
0.17	1.49	0.20	2.52	22.49	0.00	26.20	100.00
0.20	2.59	0.23	5.11	26.20	0.00	30.53	100.00
0.23	4.04	0.27	9.15	30.53	0.00	35.56	100.00
0.27	5.68	0.31	14.83	35.56	0.00	41.43	100.00
0.31	7.19	0.36	22.02	41.43	0.00	48.27	100.00
0.36	8.72	0.42	30.74	48.27	0.00	56.23	100.00
0.42	9.97	0.49	40.71	56.23	0.00	65.51	100.00
0.49	10.05	0.58	50.77	65.51	0.00	76.32	100.00
0.58	9.91	0.67	60.67	76.32	0.00	88.91	100.00
0.67	8.73	0.78	69.40	88.91	0.00	103.58	100.00
0.78	6.50	0.91	75.90	103.58	0.00	120.67	100.00
0.91	4.45	1.06	80.35	120.67	0.00	140.58	100.00
1.06	2.55	1.24	82.91	140.58	0.00	163.77	100.00
1.24	1.13	1.44	84.04	163.77	0.00	190.80	100.00
1.44	0.33	1.68	84.37	190.80	0.00	222.28	100.00
1.68	0.05	1.95	84.42	222.28	0.00	258.95	100.00
1.95	0.00	2.28	84.42	258.95	0.00	301.68	100.00
2.28	0.00	2.65	84.42	301.68	0.00	351.46	100.00
2.65	0.00	3.09	84.42	351.46	0.00	409.45	100.00
3.09	0.36	3.60	84.78	409.45	0.00	477.01	100.00
3.60	1.11	4.19	85.89	477.01	0.00	555.71	100.00
4.19	1.95	4.88	87.84	555.71	0.00	647.41	100.00
4.88	2.55	5.69	90.39	647.41	0.00	754.23	100.00
5.69	2.69	6.63	93.08	754.23	0.00	878.67	100.00



Result: Analysis Report

Sample Details

Sample ID: Sample 8
 Sample File: IH002_51
 Sample Path: D:\DATASIZE\IN-HOUSE\IH_51\

Run Number: 1
 Record Number: 339

Measured: Tue Mar 11 2008 4:07PM
 Analysed: Tue Mar 11 2008 4:07PM
 Result Source: Analysed

Sample Notes: Medium : DI water
 Dispersant : Sodium pyrophosphate
 Treatment : Ultrasonic 5 minutes & Stir medium
 Note : LNF-64-MNC-1000 C, 30 minutes, 31/01/51

System Details

Range Lens: 300RF mm
 Presentation: 3_BRTI
 Analysis Model: Polydisperse
 Modifications: None

Beam Length: 2.40 mm
 [Particle R.I. = (2.4000, 0.1000); Dispersant R.I. = 1.3300]

Sampler: MS1

Obscuration: 22.5 %

Residual: 2.545 %

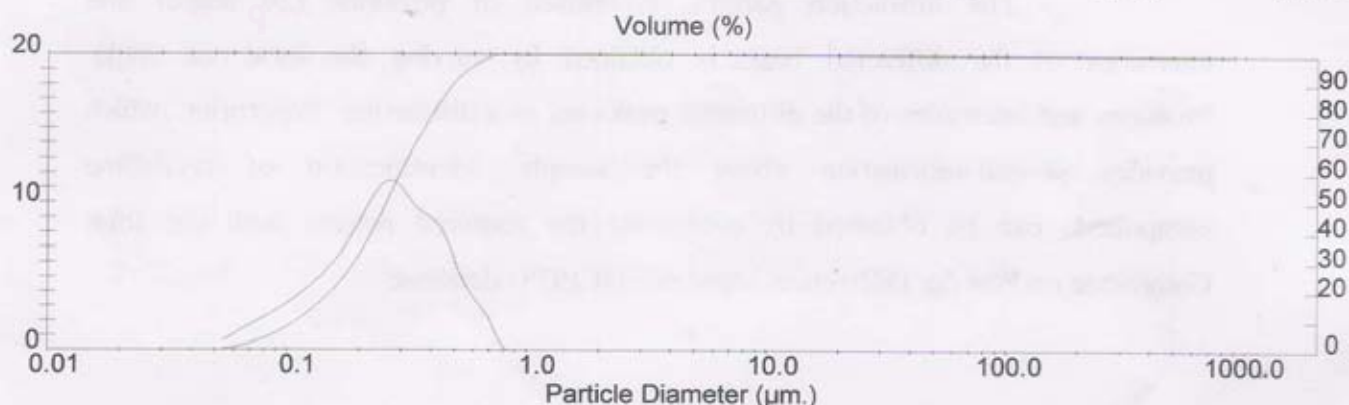
Result Statistics

Distribution Type: Volume
 Mean Diameters:
 D [4, 3] = 0.28 um

Concentration = 0.0009 %Vol
 D (v, 0.1) = 0.11 um
 D [3, 2] = 0.21 um
 Density = 1.000 g / cub. cm
 D (v, 0.5) = 0.26 um
 Span = 1.470E+00

Specific S.A. = 28.8927 sq. m / g
 D (v, 0.9) = 0.49 um
 Uniformity = 4.499E-01

Size Low (um)	In %	Size High (um)	Under%	Size Low (um)	In %	Size High (um)	Under%
0.05	0.68	0.06	0.68	6.63	0.00	7.72	100.00
0.06	1.27	0.07	1.95	7.72	0.00	9.00	100.00
0.07	1.85	0.08	3.80	9.00	0.00	10.48	100.00
0.08	2.46	0.09	6.26	10.48	0.00	12.21	100.00
0.09	3.13	0.11	9.39	12.21	0.00	14.22	100.00
0.11	3.91	0.13	13.30	14.22	0.00	16.57	100.00
0.13	4.84	0.15	18.14	16.57	0.00	19.31	100.00
0.15	6.02	0.17	24.15	19.31	0.00	22.49	100.00
0.17	7.57	0.20	31.73	22.49	0.00	26.20	100.00
0.20	9.51	0.23	41.24	26.20	0.00	30.53	100.00
0.23	11.15	0.27	52.39	30.53	0.00	35.56	100.00
0.27	11.23	0.31	63.61	35.56	0.00	41.43	100.00
0.31	9.86	0.36	73.48	41.43	0.00	48.27	100.00
0.36	9.02	0.42	82.50	48.27	0.00	56.23	100.00
0.42	7.67	0.49	90.17	56.23	0.00	65.51	100.00
0.49	4.99	0.58	95.16	65.51	0.00	76.32	100.00
0.58	3.28	0.67	98.44	76.32	0.00	88.91	100.00
0.67	1.56	0.78	100.00	88.91	0.00	103.58	100.00
0.78	0.00	0.91	100.00	103.58	0.00	120.67	100.00
0.91	0.00	1.06	100.00	120.67	0.00	140.58	100.00
1.06	0.00	1.24	100.00	140.58	0.00	163.77	100.00
1.24	0.00	1.44	100.00	163.77	0.00	190.80	100.00
1.44	0.00	1.68	100.00	190.80	0.00	222.28	100.00
1.68	0.00	1.95	100.00	222.28	0.00	258.95	100.00
1.95	0.00	2.28	100.00	258.95	0.00	301.68	100.00
2.28	0.00	2.65	100.00	301.68	0.00	351.46	100.00
2.65	0.00	3.09	100.00	351.46	0.00	409.45	100.00
3.09	0.00	3.60	100.00	409.45	0.00	477.01	100.00
3.60	0.00	4.19	100.00	477.01	0.00	555.71	100.00
4.19	0.00	4.88	100.00	555.71	0.00	647.41	100.00
4.88	0.00	5.69	100.00	647.41	0.00	754.23	100.00
5.69	0.00	6.63	100.00	754.23	0.00	878.67	100.00



Result: Analysis Report

Sample ID: Sample 8
 Sample File: IH002_51
 Sample Path: D:\DATASIZE\IN-HOUSE\IH_51\
 Sample Notes: Medium : DI water
 Dispersant : Sodium pyrophosphate
 Treatment : Ultrasonic 5 minutes & Stir medium
 Note : LNF-64-MNC-1000 C, 30 minutes, 31/01/51

Sample Details
 Run Number: 2
 Record Number: 340

Measured: Tue Mar 11 2008 4:07PM
 Analysed: Tue Mar 11 2008 4:07PM
 Result Source: Analysed

System Details

Range Lens: 300RF mm
 Presentation: 3_BRTI
 Analysis Model: Polydisperse
 Modifications: None

Beam Length: 2.40 mm
 [Particle R.I. = (2.4000, 0.1000); Dispersant R.I. = 1.3300]

Sampler: MS1

Obscuration: 22.5 %

Residual: 2.545 %

Result Statistics

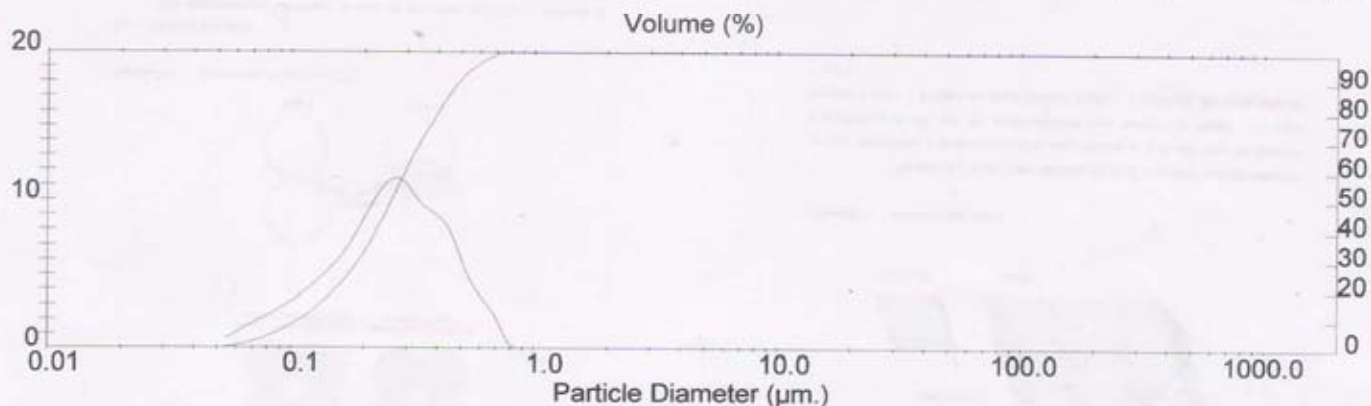
Distribution Type: Volume
 Mean Diameters:
 D [4, 3] = 0.28 um

Concentration = 0.0009 %Vol
 D (v, 0.1) = 0.11 um
 D [3, 2] = 0.21 um

Density = 1.000 g / cub. cm
 D (v, 0.5) = 0.26 um
 Span = 1.470E+00

Specific S.A. = 28.9120 sq. m / g
 D (v, 0.9) = 0.49 um
 Uniformity = 4.499E-01

Size Low (um)	In %	Size High (um)	Under%	Size Low (um)	In %	Size High (um)	Under%
0.05	0.68	0.06	0.68	6.63	0.00	7.72	100.00
0.06	1.28	0.07	1.96	7.72	0.00	9.00	100.00
0.07	1.85	0.08	3.81	9.00	0.00	10.48	100.00
0.08	2.46	0.09	6.27	10.48	0.00	12.21	100.00
0.09	3.13	0.11	9.41	12.21	0.00	14.22	100.00
0.11	3.91	0.13	13.32	14.22	0.00	16.57	100.00
0.13	4.85	0.15	18.17	16.57	0.00	19.31	100.00
0.15	6.02	0.17	24.19	19.31	0.00	22.49	100.00
0.17	7.58	0.20	31.77	22.49	0.00	26.20	100.00
0.20	9.52	0.23	41.29	26.20	0.00	30.53	100.00
0.23	11.15	0.27	52.44	30.53	0.00	35.56	100.00
0.27	11.22	0.31	63.66	35.56	0.00	41.43	100.00
0.31	9.86	0.36	73.52	41.43	0.00	48.27	100.00
0.36	9.01	0.42	82.53	48.27	0.00	56.23	100.00
0.42	7.66	0.49	90.19	56.23	0.00	65.51	100.00
0.49	4.98	0.58	95.18	65.51	0.00	76.32	100.00
0.58	3.27	0.67	98.45	76.32	0.00	88.91	100.00
0.67	1.55	0.78	100.00	88.91	0.00	103.58	100.00
0.78	0.00	0.91	100.00	103.58	0.00	120.67	100.00
0.91	0.00	1.06	100.00	120.67	0.00	140.58	100.00
1.06	0.00	1.24	100.00	140.58	0.00	163.77	100.00
1.24	0.00	1.44	100.00	163.77	0.00	190.80	100.00
1.44	0.00	1.68	100.00	190.80	0.00	222.28	100.00
1.68	0.00	1.95	100.00	222.28	0.00	258.95	100.00
1.95	0.00	2.28	100.00	258.95	0.00	301.68	100.00
2.28	0.00	2.65	100.00	301.68	0.00	351.46	100.00
2.65	0.00	3.09	100.00	351.46	0.00	409.45	100.00
3.09	0.00	3.60	100.00	409.45	0.00	477.01	100.00
3.60	0.00	4.19	100.00	477.01	0.00	555.71	100.00
4.19	0.00	4.88	100.00	555.71	0.00	647.41	100.00
4.88	0.00	5.69	100.00	647.41	0.00	754.23	100.00
5.69	0.00	6.63	100.00	754.23	0.00	878.67	100.00



VITAE

Miss Sirinoot Iamsaard was born on November 14, 1981 in Bangkok, Thailand. She received Bachelor's Degree of Education in Chemistry from Bansomdejchaopraya Rajabhat University in 2003. Since then, she attended the Master's Degree Program of petrochemistry and Poltmer Scince at Facuty of scince , Chulalongkorn University and finished she study in 2007.

Her present address in 69/6 Thoet Thai 59 Road, Pasicharem, Bangkok, 10160, Thailand. Tel 085-9414441, 02-8687645.



สถาบันวิทยบริการ
จุฬาลงกรณ์มหาวิทยาลัย